INVESTIGATION OF COMPLEX MAGNETIC PHENOMENA IN SPINEL $FeMn_2O_4$, $MnFe_2O_4$, AND $NiFe_2O_4$

A Dissertation

Submitted to the Graduate Faculty of the
Louisiana State University and
Agricultural and Mechanical College
in partial fulfillment of the
requirements for the degree of
Doctor of Philosophy

in

The Department of Physics and Astronomy

by
Roshan Kumar Nepal
B.S., Southeastern Louisiana University, 2013
M.S., Louisiana State University, 2019
May 2020

Dedicated to My Parents

Acknowledgments

As a PhD student at the Louisiana State University, I had the opportunity to work amongst some of the most supportive, loving, and caring individuals. I cannot imagine arriving at this point without their moral support.

First and foremost, I want to express my most sincere gratitude to my advisor, Professor Rongying Jin. Her mentorship, encouragement, and patience were invaluable throughout my PhD years. Her positivity, like turning lemons into lemonade, helped me overcome hurdles and learn valuable lessons from my failures. Her immense scientific curiosity helped me grow as a researcher. I could not have asked for a better advisor for my dissertation research.

I would also like to thank my committee members Professor Ward Plummer and Professor Juana Moreno. Their positive words and constructive criticisms helped me improve my work and finalize this dissertation. I also want to thank Professor Jerome Hoffman for serving as the Dean's representative in my dissertation committee. I also want to acknowledge Professor Jiandi Zhang for several thought-provoking scientific discussions.

I want to acknowledge Dr. Zhen Wang at Brookhaven National Laboratory (BNL) for her valuable help with transmission electron microscopy measurements. I also want to thank her for being a great host to me during my visit to BNL. I want to thank Dr. Qiang Zhang at Oak Ridge National Laboratory for performing neutron scattering experiments. I also want to thank Dr. Dongmei Cao for her assistance on scanning electron microscopy and energy dispersive spectroscopy. I want to thank Dr. Mohammad Saghayezhian for x-ray photoelectron spectroscopy measurements. Dr. Saghayezhian also deserves much appreciation for being a positive role model with his can-do attitude and for his encouragement.

I express my sincere gratitude to the senior members of our lab who helped me learn the lab skills needed for this work. Dr. Zhenyu Diao, Dr. Jiayun Pan, and Dr. Guixin Cao, who have since moved on from our lab, were instrumental when I was first learning how

to become an experimental condensed matter physicist. I must thank Frank Womack for his help diagnosing and fixing problems in the lab. His expertise and willingness to teach me were immensely valuable. I also want to acknowledge the entire Department of Physics and Astronomy community for creating a welcoming and supportive learning environment.

This work would have been impossible without a long list of friends and lab mates who provided support and advice during the times of needs: Ramakanta Chapai, Prahald Siwakoti, Ahmad Us Salaheen, Sumit Libi, Mohammad Saghayezhian, David Howe, Dongliang Gong, Silu Huang, Smita Speer, Joanna (Asia) Blawat, Zeeshan Ali, Tej Poudel Chhetri, Narayan Bhusal, Sushovit Adhikari, Lingyi Xing, Joel Taylor, Chetan Dhital, Hangwen Guo, Gaomin Wang, and many more. The bonds that we have made during the last several years will be forever cherished by me.

Finally, I would like to express my sincere gratitude to my family for providing their continuous love and support. My father Nanda Prasad Nepal, my mother Shanta Ghimire Nepal, and my brother Ravi Nepal have always believed in me, even when I doubted myself. Despite being far away from them for most of the time during this work, I could always reach out to them when I needed them. My partner, Brooke Elizabeth Trabona, deserves much gratitude. Her love, support, and encouragement have always helped me to be a better version of myself, and without her, this work would not have been possible.

Table of Contents

List of Figures

Abstract

Frustrated magnetic systems, where all spin interactions cannot be simultaneously satisfied, have continued to attract interest due to a plethora of novel magnetic states that emerge in them due to frustration and their potential technological applications. Spinel oxides (AB_2O_4, where A and B are metal ions) are an excellent testing ground for the exploration of frustrated magnetism. This dissertation presents the experimental investigation of complex magnetic phenomena in the spinel oxides $FeMn_2O_4$, $MnFe_2O_4$, and $NiFe_2O_4$.

$FeMn_2O_4$ and $MnFe_2O_4$ are members of the manganese ferrite family where both manganese and iron can possess mixed oxidation states, resulting in additional spin interactions that compete with the collinear ferrimagnetic order leading to complex magnetic ground states. From our measurements, we found that $FeMn_2O_4$ undergoes one structural and two magnetic transitions. The structural transition occurs at $T_s \sim 595$ K from a high temperature cubic to a low temperature tetragonal phase. Below $T_{FI\text{-}1} \sim 373$ K, it becomes collinear ferrimagnetic, and below $T_{FI\text{-}2} \sim 50$ K, its O-site spins form a spin ice-like "two-in-two-out" order. Similarly, in $MnFe_2O_4$, we identified three magnetic transitions: paramagnetic to collinear ferrimagnetic transition at $T_{FI\text{-}1} \sim 575$ K, followed by spin rearrangements at $T_{FI\text{-}2} \sim 50$ K and $T_x \sim 15$ K. Furthermore, in both systems, we found that the different magnetic orders have significant effects on other physical properties.

Frustration and complex magnetism can also be induced at the interfaces due to the competing magnetic orders. We extend our study into frustrated magnetism by exploring the interface-induced behavior in $NiFe_2O_4$ matrix containing self-assembled NiO columns that are magnetically distinct. The bulk magnetic measurements revealed a spin glass state below $T_{SG} \sim 28$ K. By combining the macroscopic measurements with the microscopic analysis, like transmission electron microscopy and magnetic force microscopy, we establish that the spin glass state occurs at the interface due to the competing magnetic orders that frustrate the interfacial spins. We demonstrate the viability of self-assembly of microstructures within a matrix as an effective way to enable emergent phenomena.

Chapter 1
Introduction

Magnetic phenomena have been fascinating mankind since our first encounter with loadstone or magnetite Fe_3O_4 and have been a crucial part of human advancement. From the earliest use of a magnetic compass as a navigational tool to the more recent application of electromagnets in radio and television, the usefulness of magnetism has helped propel human civilization at a fast pace. In the last century alone, we saw several consequential advancements in technology, such as magnetic memory device, magnetic cassette, video tapes, magnetic nuclear imaging, and so on. All these applications were direct results of the expansion of the knowledge of magnetism in materials. In recent years, the demand for magnetic materials with novel properties has risen dramatically to meet today's new technological challenges, such as high-density magnetic memory storage devices and materials with potential applications in spintronics and quantum computing. Thus, the attraction towards the study of magnetism and related phenomena is not only driven by our desire to understand the fundamental physics behind it, but also to find materials with new properties and ways to control them.

In the search for novel magnetic properties, frustrated magnets, where the ground state is highly degenerate [1], have emerged as one of the key players. The highly degenerate ground state in the frustrated magnets makes them an excellent testbed to discover new magnetic states and exotic properties of matter. In these materials, the long-range magnetic order, such as ferromagnetism and antiferromagnetism, is prevented by the competing magnetic interactions. Instead, they display a wide array of novel ground states. For example, in quantum spin liquids, the frustrated interactions collapse into a highly entangled fluctuating liquid-like ground state [2] that could be utilized in quantum computing. Spin ice is another type of frustrated magnet, where the competing interactions result in degenerate spin orders and are known to exhibit characteristics of magnetic monopoles [3]. Magnetic skyrmions, tiny whirlpools of spins touted to be useful as high density memory

devices that are usually found in special chiral magnets, can also be realized in some frustrated systems, where the interactions favoring parallel magnetic moments compete with those favoring antiparallel magnetic moments and force the magnetic moments to coil into magnetic spirals [4]. Additionally, these exotic states in frustrated magnets can be manipulated by application of external stimuli, such as magnetic field, further cementing their potential place in the next generation devices.

Spinel oxides (AB_2O_4, where A and B are metal ions) hold a special place among frustrated magnets. Named after the eponym mineral $MgAl_2O_4$, known as Spinel, this class of compounds consists of more than two hundred members and is one of the most extensive series of compounds, owing to their chemical versatility [5]. For instance, in the mineral Spinel ($Mg^{2+}Al_2^{3+}O_4$), a wide range of divalent and trivalent cations can be substituted for Mg^{2+} and Al^{3+} cations, respectively. Their versatility coupled with their unique crystal structure, which is described in Section 1.4, provide possibilities for a wide range of physical properties that have been tuned for many practical applications [5] and have established them as a fertile ground to explore the physics of frustration. The goal of this dissertation is to experimentally investigate the complex magnetic landscape resulting from frustration in three iron-based spinel oxides: $FeMn_2O_4$, $MnFe_2O_4$, and $NiFe_2O_4$.

The work presented in this dissertation is organized in the following way. In the subsequent sections of this chapter, an overview of the basic principles of magnetism including geometric frustration and spinel structure is provided. The experimental techniques from the synthesis of materials to their characterization is presented in Chapter 2. Chapters 3 and 4 provide the results from the experimental studies of the physical properties of single crystals of $FeMn_2O_4$ and $MnFe_2O_4$, respectively, with an emphasis on their complex magnetic orders and their effects on other physical properties. Chapter 5 presents the interfacial spin glass state emerging in the single crystal $NiFe_2O_4$ with self-assembled NiO columns. Lastly, Chapter 6 summarizes the key results from this work.

1.1 Review of magnetism

This section outlines the theoretical concepts about magnetism that are required to explain the experimental results from this work. First, a brief introduction to magnetism is presented, with reference to the textbooks by Stephen Blundell [6] and Allan H. Morrish [7]. Then, the concept of geometric frustration is discussed. In the latter part of this chapter, an introduction to the spinel oxides and their complex magnetic phase diagrams is presented.

1.1.1 Magnetic moments

Magnetic moment, which is the fundamental object in magnetism, is responsible for the origin of the magnetic behavior in a material [6]. In classical electromagnetism, a magnetic moment arises from a current loop created by the motion of electrons. For an electron (charge $-e$, mass m_e) orbiting around the nucleus of a hydrogen atom in a circular orbit, the magnetic moment is given by $\mu = \pi r^2 I$, where I is the loop current due to the electron's motion and r is the radius of its orbit. In the ground state, the angular momentum of the electron is $m_e v r = \hbar$, so the magnetic moment of the electron is given by

$$\mu = \pi r^2 I = -\frac{e\hbar}{2m_e} \equiv -\mu_B, \tag{1.1}$$

where μ_B is the Bohr magneton[1]. Since it arises from the orbital motion of an electron, this angular momentum is known as the orbital angular momentum.

In quantum mechanics, this orbital angular momentum is characterized by the orbital quantum number l, whose value ranges from $0, 1, ..., (n-1)$, where n is the energy level occupied by the electron. In addition to l, an electron also possesses an intrinsic angular momentum known as spin, which is characterized by the spin quantum number $s = \frac{1}{2}$. For each l and s, there is a magnetic quantum number, m_l and m_s, respectively, which represents its value along a fixed axis, usually taken as the z axis. The quantum numbers $m_{l,s}$ can have one of $2(l,s)+1$ values from $\{-l, -l+1, ..., l-1, l\}$ and $\{-s, -s+1, ..., s\}$,

[1] $\mu_B = 9.274 \times 10^{-24} Am^2$

respectively. This means, for an electron, $m_s = \pm\frac{1}{2}$. These two values are referred to as "spin up" and "spin down" for positive and negative values of m_s, respectively.

1.1.2 Moments in a magnetic field

Let us consider an atom with Z electrons. The total Hamiltonian $\hat{\mathcal{H}}_0$ of the electrons has the usual form

$$\hat{\mathcal{H}}_0 = \sum_{i=1}^{Z}[\frac{\mathbf{p}_i^2}{2m_e} + V_i], \tag{1.2}$$

where $\mathbf{p}_i$ is the linear momentum of of the i^{th} electron and V_i is the electrostatic potential experienced by the it. Let us now add an external magnetic field $\mathbf{H}$ which perturbs the system. The new, perturbed Hamiltonian can be written as

$$\hat{\mathcal{H}} = \sum_{i=1}^{Z}\Big[\frac{[\mathbf{p}_i + e\mathbf{A}(\mathbf{r}_i)]^2}{2m_e} + V_i\Big] + g\mu_B\mu_0\mathbf{H}\cdot\mathbf{S}, \tag{1.3}$$

where $\mathbf{A}$ is the vector potential, $\mathbf{S}$ is the total spin of the electrons, and g is a constant called g-factor. The term $g\mu_B\mu_0\mathbf{H}\cdot\mathbf{S}$ is called the Zeeman term, which accounts for the interaction between the magnetic field and the spins of the electrons. For a uniform magnetic field, we can choose the vector potential to satisfy the gauge $\mathbf{A}(r) = \frac{1}{2}(\mu_0\mathbf{H}\times\mathbf{r})$, such that $\mu_0\mathbf{H} = \nabla\times\mathbf{A}$. Then, Eq. (1.3) can be rearranged as

$$\hat{\mathcal{H}} = \hat{\mathcal{H}}_0 + \mu_B(\mathbf{L} + g\mathbf{S})\cdot\mu_0\mathbf{H} + \frac{e^2}{8m_e}\sum_i(\mu_0\mathbf{H}\times\mathbf{r}_i)^2, \tag{1.4}$$

where $\mathbf{L} = 1/\hbar\sum i\mathbf{r}_i\times\mathbf{p}_i$ is the total angular momentum. The second term in the above equation is the dominant perturbation to the original Hamiltonian $\hat{\mathcal{H}}_0$. This term, known as the paramagnetic term, is a consequence of the atom's total magnetic moment. Therefore, if the total magnetic moment is equal to zero, then there is no contribution from this term. The third term in Eq. (1.4) is usually much smaller than the paramagnetic term and is only relevant if the paramagnetic term is negligible. This term is known as the diamagnetic term.

1.1.3 Hund's rules

In an ion containing many electrons occupying several shells, the total orbital angular momentum **L** and the total spin angular momentum **S** are a combination of the spin and orbital momenta of all of the electrons. Hence, the total magnetic momentum of an ion depends on how the electrons fill the available energy levels. The electrons populate the available energy levels such that the total energy is minimized by following the Hund's rules that are listed below.

1. Arrange the electrons such that the total spin **S** is maximized. This configuration minimizes the Coulomb energy. This is analogous to the Pauli's exclusion principle.

2. With the total spin **S** maximized, maximize the total orbital momentum **L**. This also reduces the Coulomb repulsion between the electrons.

3. Minimize the spin-orbit energy. The total angular momentum **J** is given by $|L - S|$ if the shell is less than half full and by $|L + S|$ if the shell is more than half full.

Equipped with the three Hund's rules, we can predict the sequence by which the electrons occupy the energy levels in an ion, and thus allowing us to estimate the total magnetic moment of an ion.

1.1.4 Magnetic ions in crystals

In the previous sections, we treated the magnetic ions as completely free entities without any interactions with their surroundings. However, in a crystal, the magnetic ions interact with their local surroundings as well as their neighbors. An ion in a crystal experiences a crystal field (CF), which is an electric field derived from its neighboring atoms. The size and nature of the CF depends on the local symmetry around the ion, i.e. its local environment.

Let us consider a common case of a transition metal[2] ion sitting at the center of an octahedral environment formed by oxygen anions located along the x, y, and z axes, as

[2]An element whose atom has a partially filled d sub-shell, eg. Cr, Mn, Fe, etc. (IUPAC)

shown in Figure 1.1(a). Here, the CF arises from the electrostatic interaction between the 3d orbitals of the metal ion and the 2p orbitals of the corner oxygen atoms. As shown in Figure 1.1(b and c), among the five degenerate 3d orbitals, e_g orbitals (d_{z^2} and $d_{x^2-y^2}$) lie along the coordinate axes, whereas the t_{2g} orbitals (d_{xy}, d_{xz}, and d_{yz}) lie between the axes. Therefore, the e_g orbitals have a larger overlap with the 2p orbitals of the corner oxygen ions, leading to a larger electrostatic energy compared to the t_{2g} orbitals. This makes the t_{2g} orbitals more energetically favorable. This can be seen clearly in the planar view of the xy plane shown in Figure 1.1(d and e). As a result, the CF splits the five-fold degenerate 3d orbitals as shown in Figure 1.2(b), with the three-fold t_{2g} levels having lower energy than the two-fold e_g levels.

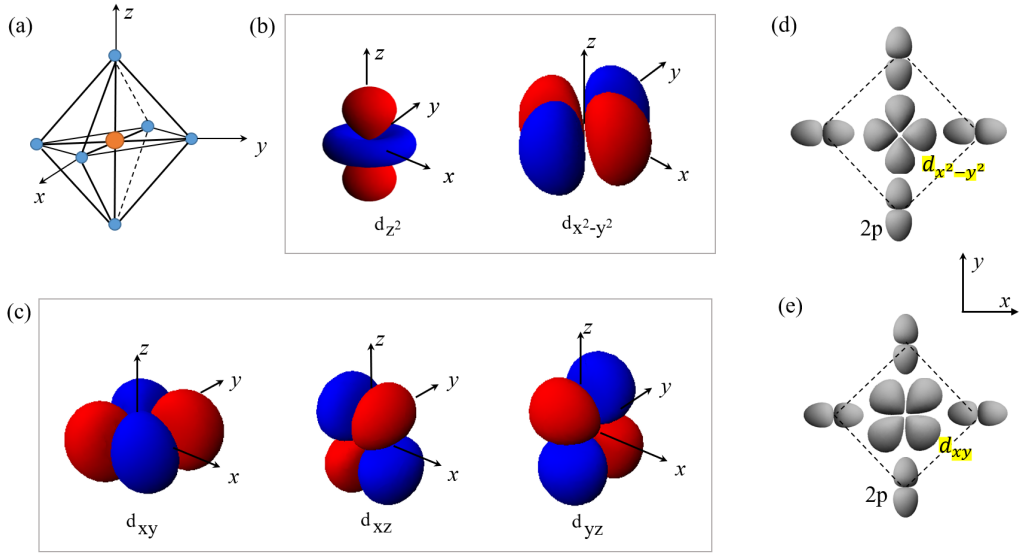

Figure 1.1. (a) A 3d metal ion (orange dot) at the center of an octohedron formed by oxygen ions (blue dots). (b and c) Probability distributions of e_g orbitals and t_{2g} orbitals, respectively. (d and e) Orbital overlaps between the oxygen 2p orbitals and $d_{x^2-y^2}$ and d_{xy} orbitals, respectively.

The situation is reversed in a tetrahedral environment, where the oxygen ions are located between the axes resulting in a larger overlap between their 2p orbitals and the t_{2g} orbitals of the metal ion. So, in a tetrahedral environment, the two-fold e_g levels have lower energy than the three-fold t_{2g} levels.

Although the electrons occupy the low energy orbitals first before filling up the higher energy orbitals by obeying the Hund's rules, the CF effect can influence this order. If the CF energy is smaller than the pairing energy, i.e. the energy cost of putting two electrons in the same orbital, then the electrons will occupy all five orbitals singly before doubly occupying them. This scenario is called the weak-field case and it leads to a high spin (HS) state. In the reverse scenario where the pairing energy is lower than the CF energy, the electrons will doubly occupy the lower energy orbitals before they fill the higher energy orbitals. This leads to a low spin (LS) state and is called a strong-field case. A schematic of a singly occupied HS state for a $3d^4$ ion is displayed in Figure 1.2(b).

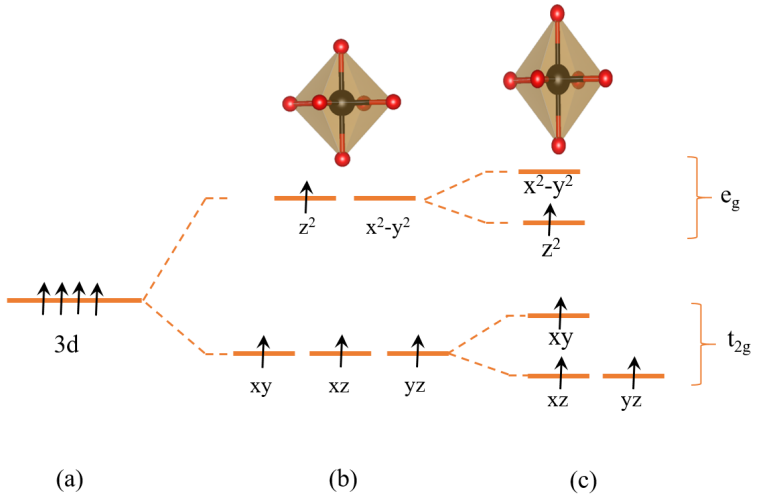

Figure 1.2. (a) Five-fold degenerate 3d orbitals in a free ion. (b) Splitting of e_g and t_{2g} orbitals due to the crystal field. (c) Further splitting of orbitals due to the Jahn-Teller effect.

Despite the CF effect, the degeneracy in the t_{2g} and e_g orbitals are still present. This is where the Jahn-Teller theorem comes into play, which states that "the nonlinear complexes or ions which have a degenerate ground state will spontaneously distort and the degeneracy will be removed" [8]. The distortion, known as the Jahn-Teller (J-T) effect, occurs because a small displacement of the ions will reduce the energy. In a $3d^4$ ion in an octahedral environment, the splitting of the two e_g orbitals lowers the net energy of the system; therefore, the octahedron will spontaneously elongate, as shown in Figure 1.2(c). However,

in a $3d^3$ ion, the splitting of the two empty e_g will not lower the net energy of the system; therefore, it will not undergo a distortion.

This effect is profound in crystals with a significant amount of "Jahn-Teller active" ions. Below a certain critical temperature, these ions can collectively undergo a J-T distortion throughout the crystal, leading to a change in the overall crystallographic symmetry. This is known as a cooperative J-T transition.

1.1.5 Magnetic interactions

To understand the various types of magnetic states, let us first discuss the different types of magnetic interactions that allow the magnetic moments in a crystal to communicate with each other, potentially allowing them to produce long range orders.

One of the basic interactions between two magnetic moments is the *magnetic dipolar interaction*. Two magnetic moments μ_1 and μ_2 separated by a distance $\mathbf{r}$ have an interaction energy given by

$$E = \frac{\mu_0}{4\pi r^3}\Big[\mu_1 \cdot \mu_2 - \frac{3}{r^2}(\mu_1 \cdot \mathbf{r})(\mu_2 \cdot \mathbf{r})\Big]. \tag{1.5}$$

This energy depends on the mutual alignment between the two moments and their separation. For two magnetic moments $\mu \sim \mu_B$ separated by a typical interatomic distance in solids $\sim$1 Å, the dipolar energy $E \sim 10^{-23}$J $\sim 10^{-4}$eV, which is equivalent to about 1 Kelvin, much smaller than the ordering temperature of many magnetic materials such as iron ($T_C \sim 1000$ K). Therefore, dipolar interactions alone could not explain the long range order in most magnetic materials but can be significant in materials that order at milliKelvin temperatures.

Exchange interactions lie at the heart of the phenomenon of long range magnetic order in solids [6]. The exchange interactions are simply the electrostatic interaction, i.e. charges of the same sign cost energy when they are close together and save energy when they are far apart. To understand the origin of the exchange interaction, let us consider two electrons with spatial coordinates $\mathbf{r}_1$ and $\mathbf{r}_2$, respectively. If these two electrons are in states $\psi_a(\mathbf{r}_1)$ and $\psi_b(\mathbf{r}_2)$, respectively, then the wave function for their joint state is given by their

product $\psi_a(\mathbf{r}_1)\psi_b(\mathbf{r}_2)$. Since electrons are fermions, the overall wavefunction, including the spin part, must be antisymmetric. If the spatial state ψ is symmetric, then the spin part χ must be asymmetric state. In the asymmetric state, also known as the singlet state (χ_S), the two spins are antiparallel leading to an S = 0 state. Similarly, if the spatial state is asymmetric, then the spin part must be symmetric, also known as spin triplet state (χ_T) with S = 1. Therefore, the overall wave function Ψ can be written as

$$\Psi_S \propto \big[\psi_a(\mathbf{r}_1)\psi_b(\mathbf{r}_2) + \psi_a(\mathbf{r}_2)\psi_b(\mathbf{r}_1)\big]\chi_S \tag{1.6}$$

and

$$\Psi_T \propto \big[\psi_a(\mathbf{r}_1)\psi_b(\mathbf{r}_2) - \psi_a(\mathbf{r}_2)\psi_b(\mathbf{r}_1)\big]\chi_T \tag{1.7}$$

for the singlet and triplet configuration, respectively. If $\hat{\mathcal{H}}$ is the Hamiltonion of the system, then the difference in energies between the two states is given by

$$E_S - E_T \propto \int \psi_a^*(\mathbf{r}_1)\psi_b^*(\mathbf{r}_2)\hat{\mathcal{H}}\psi_a(\mathbf{r}_2)\psi_b(\mathbf{r}_1)d\mathbf{r}_1\mathbf{r}_2. \tag{1.8}$$

The exchange constant or the exchange integral, J is defined as

$$J = E_S - E_T = \int \psi_a^*(\mathbf{r}_1)\psi_b^*(\mathbf{r}_2)\hat{\mathcal{H}}\psi_a(\mathbf{r}_2)\psi_b(\mathbf{r}_1)d\mathbf{r}_1\mathbf{r}_2, \tag{1.9}$$

and the spin-dependent term in the effective Hamiltonion can be written as

$$\hat{\mathcal{H}}^{spin} = -J\mathbf{S}_1 \cdot \mathbf{S}_2, \tag{1.10}$$

where $\mathbf{S}_1 \cdot \mathbf{S}_2$ is the spin-spin interaction. If J > 0, then $E_S > E_T$, leading to the S = 1 state, i.e. the spins are aligned. If J < 0, then the S = 0 state is favorable, i.e. the spins are anti-aligned. If the two electrons are on the same atom, the excahnge integral is generally positive. This means they are aligned so that the spatial part of the wavefunction is anti-

symmetric. This keeps the two electrons apart and minimizes the electrostatic repulsion. On the other hand, if the two electrons are on neighboring atoms, J is likely to be negative as the electrons prefer to form bonds so that they can be less confined. So, here singlet state is favored.

The following are some of the various types of exchange interactions commonly found in magnetic solids.

Direct exchange is when the electrons in the neighboring magnetic ions interact directly via an exchange interaction. Quite often, there is insufficient overlap between the orbitals of neighboring magnetic atoms. So, direct exchange alone cannot justify all magnetic orders. For this we need to consider some indirect exchange interaction between the electrons, such as superexchange, double exchange, and RKKY interactions.

Superexchange is defined as an indirect interaction between non-neighboring magnetic ions that is mediated by a non-magnetic ion located in between them. This interaction usually results in an antiparallel spin alignment as it lowers the overall kinetic energy part in the Hamiltonian. Superexchange is responsible for antiferromagnetism in a number of ionic solids such as 3d metal oxides (MO) where the superexchange between the neighboring magnetic metal ions is mediated by an oxygen ion.

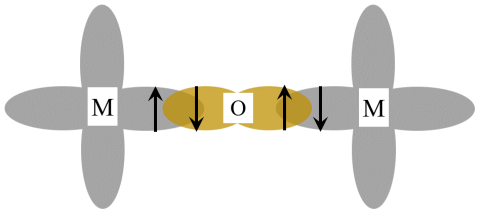

Figure 1.3. M-O-M bond in a magnetic metal oxide. The overlap between the 3d orbitals of the metal ion M and the 2p orbitals of oxygen represents the bonds. The arrows represent the spins of the four electrons involved in the bonding process. The lowest energy configuration of the spins is the antiferromagnetic alignment of the neighboring spins.

For simplicity, if we assume that the magnetic moment on the metal ion is due to a single unpaired electron and that the system is perfectly ionic, then the single unpaired electron in the 3d orbital of the metal ion and the two p electrons in the oxygen ions are

responsible for the M-O-M bonding, as shown in Figure 1.3. The four bonding electrons can be oriented in several different ways on the three ions, out of which the antiferromagnetically aligned configuration has the lowest energy. This configuration allows the bonding electrons to become delocalized over the whole M-O-M structure and thus lowers the total kinetic energy.

In compounds with magnetic ions that show mixed valence, an exchange interaction occurs between the ions with two oxidation states, which is called *double exchange*. Double exchange allows the neighboring ions to have a high spin configuration while allowing for electron hopping between the neighboring orbitals. This process is depicted in Figure 1.4. If a solid has Mn^{3+} and Mn^{4+} ions as nearest neighbors, then the lone e_g electron on a Mn^{3+} ion can hop to the neighboring Mn^{4+} as it has no electrons in its e_g orbital. However, because of Hund's first rule the e_g electron and the three t_{2g} electrons must be aligned. Thus, it is not energetically favorable for an e_g electron to hop to a neighboring ion in which the t_{2g} spins would be antiparallel to itself. Hence, the moments in the neighboring ions ought to be aligned ferromagnetically to maintain the high-spin arrangement on both ions. This ability to hop between neighboring ions lowers the kinetic energy as the electrons are once again more delocalized. This process also makes the solid conductive.

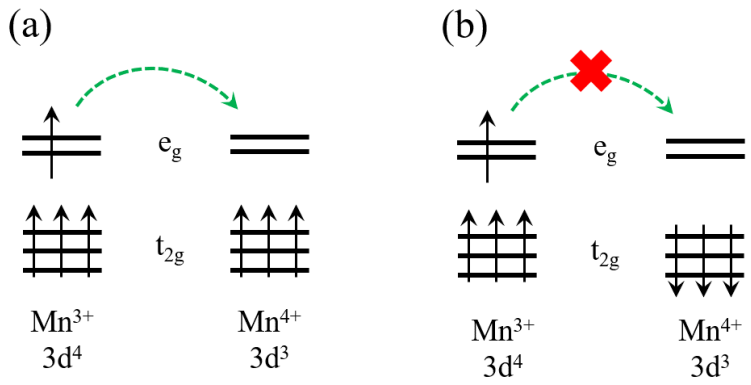

Figure 1.4. Double exchange mechanism in neighboring Mn^{3+} and Mn^{4+} ions. (a) The hopping of the e_g electron is allowed in ferromagnetically aligned neighbors. (b) In the neighboring ions that are antiferromagnetically aligned, the hopping of e_g electron is not allowed.

The *RKKY interaction* is an indirect exchange in metals that is mediated by the conduction electrons. A localized magnetic moment polarizes the conduction electrons. These polarized electrons can couple with the neighboring magnetic moments a distance r away. It is termed after Ruderman, Kittel, Kasuya, and Yosida, who discovered this effect. The strength of the RKKY interaction is given by $J_{RKKY} \propto \frac{cos(2k_F r)}{r^3}$, where k_F is the Fermi surface radius. Clearly, this interaction is oscillatory, and depending on the distance r, it can be antiferromagnetic or ferromagnetic.

Dzyaloshinsky-Moriya interaction, or the anisotropic exchange, is the exchange interaction between the ground state of one magnetic ion and the excited state of the another that is produced by the spin-orbit interaction. If such an interaction is present in a solid, the Hamiltonian has an extra term

$$\hat{\mathcal{H}}_{DM} = \mathbf{D} \cdot \mathbf{S}_1 \times \mathbf{S}_2. \tag{1.11}$$

The vector $\mathbf{D}$ depends on the crystal symmetry. If the crystal has an inversion symmetry with respect to the center between the two magnetic ions, then the vector $\mathbf{D} = 0$. If $\mathbf{D}$ is not equal to zero, it tries to align the neighboring spins at a right angle and therefore induces a twist in the neighboring moments directions.

The magnetic ground state of a solid depends on the various magnetic interactions discussed above as well as their strengths. Figure 1.5 shows the microscopic arrangement of magnetic moments in a crystal with various types of magnetic orders. In the following subsection, some of the most common types of magnetic states will be discussed.

1.1.6 Types of magnetism in matter

Since a crystal has a large number of magnetic moments, it is practical to define the magnetic moment per unit volume as the magnetization $\mathbf{M}$. In the presence of an external magnetic field $\mathbf{H}$, one can define the magnetic susceptibility χ as

$$\chi = \lim_{H \to 0} \frac{\partial M}{\partial H}. \tag{1.12}$$

For a constant field, $\chi = \frac{M}{H}$.

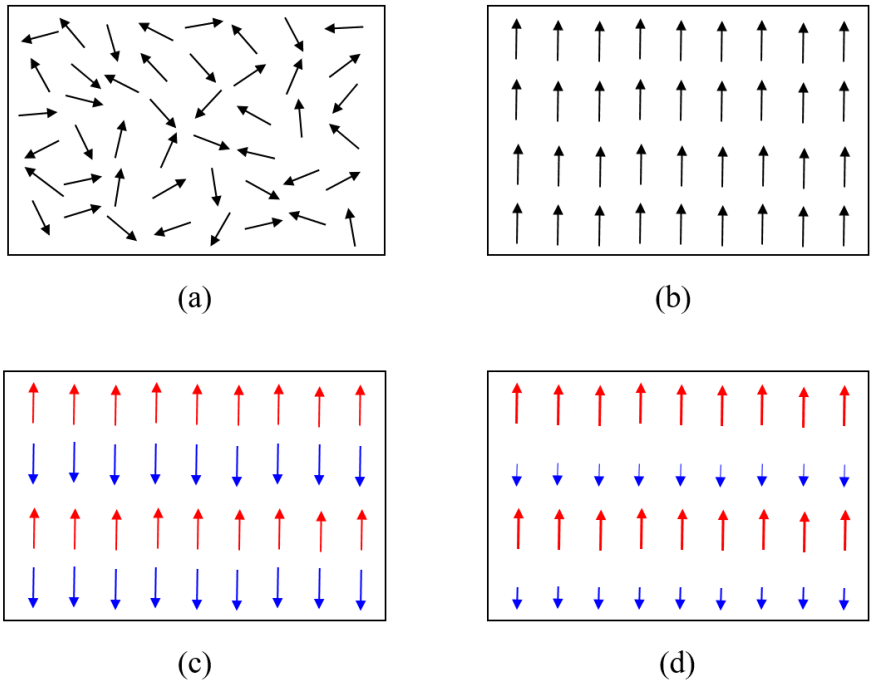

Figure 1.5. Arrangements of magnetic moments in (a) paramagnet, (b) ferromanget, (c) antiferromagnet, and (d) ferrimagnet.

As the prefix dia suggests, in a diamagnetic material, a magnetic field induces a net magnetization that is aligned against it. Therefore, diamagnets have $\chi < 0$. The third term in Eq. (1.4), which is the interaction of the magnetic field with the orbital motion of the electrons, is responsible for diamagnetism. Since the orbital motion of electrons do not depend on temperature, χ_{dia} in turn is temperature-independent. Strictly speaking, all materials possess diamagnetism, but this effect is very small and negligible in materials where there are other types of magnetic interactions. Therefore, diamagnetism is only observed in materials that have ions with completely filled orbitals, i.e. $\mathbf{J} = 0$.

Paramagnetism is when $\chi > 0$. In other words, paramagnets are materials where the magnetic moments align in the same direction as the applied field. Paramagnetism arises from the second term in Eq. (1.4), which is related to the effect of the magnetic field on the

orbital angular momentum and spin of the electrons. Therefore, paramagnetism occurs in those materials where the constituting ions possess non-zero total moments $\mathbf{J} \equiv \mathbf{L} + \mathbf{S}$. In the absence of an external magnetic field, these moments point in random directions and cancel each other, resulting in a zero total magnetization, as shown in Figure 1.5(a). When an external magnetic field is applied, the moments align themselves along the direction of the field since it lowers the total energy of the system. This results in a net magnetization M in the direction parallel to the applied field H, leading to a positive χ.

The susceptibility in paramagnets is temperature-dependent and follows the Curie's law

$$\chi = \frac{C}{T}, \tag{1.13}$$

where C is the Curie constant.

Ferromagnetism (FM) occurs when the exchange interaction $J > 0$. In a ferromagnet, there exist a characteristic temperature known as Curie temperature ($\mathrm{T_C}$) below which all magnetic moments are in parallel alignment. This gives rise to a spontaneous magnetization, even in the absence of an external magnetic field. Above $\mathrm{T_C}$, the magnetic susceptibility in a ferromagnet follows the Curie Weiss law

$$\chi = \frac{C}{T - \theta}, \tag{1.14}$$

where C is the Curie constant and θ is the Curie Weiss temperature.

If the exchange interaction $J < 0$, the neighboring spins want to point in opposite directions. This configuration is called antiferromagnetism (AFM). In an AFM system, below a characteristic temperature called the Néel temperature ($\mathrm{T_N}$), the anti-aligned neighboring spins cancel each other out and result in a zero net magnetization. Above $\mathrm{T_N}$, the magnetic susceptibility in AFM also follows Eq. (1.14), but with a negative θ.

An AFM lattice can be thought of as two interpenetrating sublattices, one where the spins point up and the other where the spins point down, as shown in Figure 1.5(c). If the spins in the two sublattices are equal in magnitude, then there is zero net magnetization. However, if the spins in the sublattices have unequal magnetic moments, like in Figure 1.5(d), then there still exists a net magnetic moment. Such a configuration is known as ferrimagnetism (FI). In the case of FI, the magnetic susceptibility follows the following relation at temperatures above the ordering temperature [9]

$$\frac{1}{\chi} = \frac{T - \theta_a}{C} - \frac{\xi}{T - \theta'}, \tag{1.15}$$

where θ_a is the asymptotic Curie temperature, C is the Curie constant, and ξ and θ' are constants derived from the molecular field theory, which will be described in detail in Section 1.2.

Spin glass (SG) is one of the magnetic systems in which the magnetic interactions are competing with each other which prevents the formation of the conventional long-range magnetic orders [10]. They are characterized by a random cooperative freezing of spins below a well-defined freezing temperature T_f. Due to the competing interactions that cannot be simultaneously satisfied, the ground state in a SG is composed of highly degenerate metastable states. Due to the metastability of the ground states, SG demonstrates several unique features, such as time-dependent magnetization relaxation and magnetic memory effect.

The competing interactions in a SG want to freeze the spins in random directions, whereas an applied magnetic field wants to align the spins parallel to it [10]. Therefore, there is a competition between the SG freezing and the Zeeman energy, and strong enough magnetic fields can completely destroy the SG state.

1.2 Two-sublattice model for ferrimagnetism

The two-sublattice model for ferrimagnetism is based on the molecular field theory developed first for antiferromagnetic systems by Louis Néel [11, 12], which he later extended for ferrimagnets [9, 13]. This section briefly summarizes this description of ferrimagnets. For more detail, we direct the reader to Ref. [7].

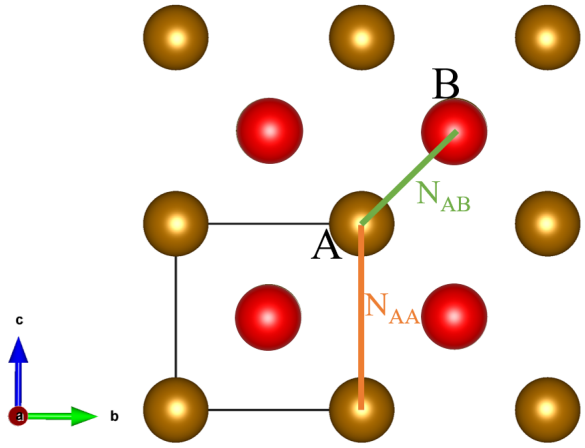

Figure 1.6. A body centered cubic structure decomposed into two sublattices. The corner atoms (brown balls) and the body atoms (red balls) compose the A and B sublattices, respectively.

Let us consider a simple example of a body-centered cubic crystal, with the A sublattice consisting of the corner positions and the B sublattice consisting of the body positions. In this arrangement, an atom at the A site has all of its nearest neighbors lie on B sites and all of its next nearest neighbors lie on A sites and vice versa. In the mean field theory, the molecular field acting on an atom at an A site can be written as

$$\mathbf{H}_{mA} = -N_{AA}\mathbf{M}_A - N_{AB}\mathbf{M}_B, \tag{1.16}$$

where $\mathbf{M}_A$ and $\mathbf{M}_B$ are the magnetizations of the A and B sublattices, respectively. The coefficients N_{AB} and N_{AA} are the molecular field constants for the nearest neighbor interaction and next nearest neighbor interactions, respectively. The molecular field acting on

an B site atom can be similarly written as

$$\mathbf{H}_{mB} = -N_{BA}\mathbf{M}_A - N_{BB}\mathbf{M}_B. \tag{1.17}$$

Here, N_{BA} and N_{BB} are the nearest neighbor and next nearest neighbor interaction constanst for the B site atom, respectively. At equilibrium, $N_{AB} = N_{BA}$. If an external field $\mathbf{H}$ is applied, then the fields $\mathbf{H}_A$ and $\mathbf{H}_B$ at an atom on the A and B sublattices are given by

$$\mathbf{H}_A = \mathbf{H} - N_{AA}\mathbf{M}_A - N_{AB}\mathbf{M}_B \tag{1.18}$$

and

$$\mathbf{H}_B = \mathbf{H} - N_{AB}\mathbf{M}_A - N_{BB}\mathbf{M}_B. \tag{1.19}$$

At thermal equilibrium, the sublattice magnetizations are given by

$$M_A = \sum_i N_i g_i \mu_B S_i B_{S_i}(x_A) \tag{1.20}$$

and

$$M_B = \sum_j N_j g_j \mu_B S_j B_{S_j}(x_B), \tag{1.21}$$

where,

$$x_{A,B} = \frac{S_{i,j} g_{i,j} \mu_B}{k_B T} \mathrm{H}_{A,B} \tag{1.22}$$

and $B_{S_{i,j}}(x_{A,B})$ are the Brillouin functions.[3] N_i is the number of atoms per unit volume with spin S_i. Above the transition temperature $\mathrm{T_{FI}}$, i.e. x appraoches zero, the Brillouin function can be approximated as $B_{S_{i,j}}(x_{A,B}) \sim \frac{g\mu_B(S_{i,j}+1)}{3k_B T}\mathrm{H}_{A,B}$, and the sublattice magnetizations are given by

$$M_A = \frac{C_A}{T} H_A \tag{1.23}$$

[3] $B_S(x) = \frac{2S+1}{2S}\coth\left(\frac{2S+1}{2S}x\right) - \frac{1}{2S}\coth\left(\frac{1}{2S}x\right)$

and

$$M_B = \frac{C_B}{T} H_B, \tag{1.24}$$

where, the sublattice Curie constants C_A and C_B are given, respectively, by

$$C_A = \sum_i \frac{N_i g^2 \mu_B^2 S_i(S_i+1)}{3k_B} = \sum_i \frac{N_i}{3k_B} \mu_B^2 \mu_{eff,A}^2 \tag{1.25}$$

and

$$C_B = \sum_j \frac{N_j g^2 \mu_B^2 S_j(S_j+1)}{3k_B} = \sum_j \frac{N_j}{3k_B} \mu_B^2 \mu_{eff,B}^2. \tag{1.26}$$

Here, $\mu_{eff,A}$ and $\mu_{eff,B}$ are effective magnetic moments in A and B sublattice, respectively. Substituting Eqs. (1.23) and (1.24) into Eqs. (1.18) and (1.19) and rearranging, we get

$$(T + C_A N_{AA}) M_A + C_A N_{AB} M_B = C_A H \tag{1.27}$$

and

$$C_B N_{AB} M_A + (T + C_B N_{BB}) M_B = C_B H. \tag{1.28}$$

Finally, we can solve the above coupled equations to obtain the sublattice magnetizations

$$M_A = \frac{C_A(T + C_B N_{BB}) - C_A C_B N_{AB}}{(T + C_A N_{AA})(T + C_B N_{BB}) - C_A C_B N_{AB}^2} H \tag{1.29}$$

and

$$M_B = \frac{C_B(T + C_A N_{AA}) - C_A C_B N_{AB}}{(T + C_A N_{AA})(T + C_B N_{BB}) - C_A C_B N_{AB}^2} H. \tag{1.30}$$

The total magnetization $M = M_A + M_B$ can then be used to determine the magnetic susceptibility $\chi = (M_A + M_B)/H$ and simplified to obtain the paramagnetic inverse susceptibility in Eq. (1.15)

$$\frac{1}{\chi} = \frac{T - \theta_a}{C} - \frac{\xi}{T - \theta'}, \tag{1.31}$$

where $C = C_A + C_B$ and

$$\theta_a = -\frac{1}{C}(C_A^2 N_{AA} + C_B^2 N_{BB} + 2C_A C_B N_{AB}), \tag{1.32}$$

$$\begin{aligned}\xi = \frac{C_A C_B}{C^3}\{&C_A^2(N_{AA} - N_{AB})^2 + C_B^2(N_{BB} - N_{AB})^2 \\ &-2C_A C_B[N_{AB}^2 - (N_{AA} + N_{BB})N_{AB} + N_{AA}N_{BB}]\},\end{aligned} \tag{1.33}$$

and

$$\theta' = -\frac{C_A C_B}{C}(N_{AA} + N_{BB} - 2N_{AB}). \tag{1.34}$$

Figure 1.7 shows the hyperbolic nature of the inverse susceptibility above the transition temperature T_{FI}. Clearly, at $T \gg T_{FI}$, $1/\chi$ follows a linear relationship with T, similar to the case of FM and AFM.

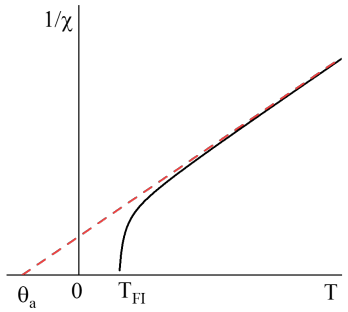

Figure 1.7. Temperature dependence of inverse susceptibility above the ferrimagnetic transition temperature T_{FI} (solid line). The red dashed line shows the asymptotic linear behavior at $T \gg T_{FI}$.

1.3 Geometric frustration

Frustration is a phenomenon in which competing interactions prevent the ground state from having a unique, well-defined structure in which all bonds are optimized [14]. This phenomenon was first studied in water ice. From a series of low temeprature thermodynamic measurements, William Giauque et al. found that the solid phase of water possesses a residual entropy, seemingly of no obvious origin [15, 16]. Their result was explained by Linus Pauling in terms of a macroscopic number of proton (H^+) configurations in ice [17]. The

mismatch between the crystalline symmetry and the local hydrogen bonding requirements of the H_2O molecule leads to frustration and give rise to the so-called "ice rules" [18]. The ice rules dictate that for each O-O bond there must be on average one H^+ ion, and for each O^{2+} ion two H^+s must be in "near position" and two H^+s in "far position." This leads to a degenerate ground state of the positions of the protons around the oxygen atom in an ice tetrahedron with "two-near/two-far" configuration, as shown in Figure 1.8(a and b). The residual entropy at 0 K is the result of the degenerate ground states that can satisfy the two-near/two-far configurations.

In the context of magnetism, an antiferromagnetic triangular lattice where the nearest neighbors of a site are themselves nearest neighbors, the ground state is frustrated. As shown in Figure 1.8(c), if the spin in site Y is up, then the antiferromagnetic interaction between sites Y and Z will result in a spin down configuration in site Z; however, since site X is nearest-neighbor to both sites Y and Z, it cannot achieve a stable ground state, resulting in a two-fold degenerate ground state.

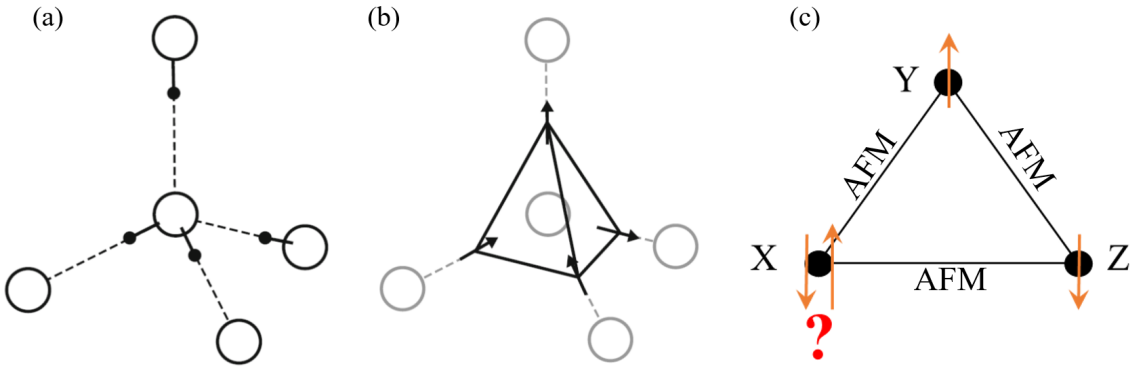

Figure 1.8. Geometric frustration. (a) Local proton arrangement in water ice, showing tetrahedrally coordinated oxygen ions (large white circles) and protons (small black dots). Following the ice rules, the four protons around the oxygen ion have a "two-near/two-far" configuration. (b) Same as (a), but with the position of a proton represented by a displacement vector (arrow). This is analogous to the two-in/two-out spin configuration in spin ice. (c) Frustration in a triangular AFM lattice. (a) and (b) are adapted from [1].

Therefore, in materials where the geometry of the magnetic lattice is based on triangles, the occurrence of the magnetic ordering depends on the subtle deviations from a

perfect triangular symmetry and/or the higher order nearest-neighbor interactions; it does not happen until temperatures far below what is expected from just the nearest neighbor interactions [19]. However, the presence of strong exchange interactions gives rise to a large Curie-Weiss temperature, making the ratio $\theta_{C-W}/\mathrm{T_{FI}} \gg 1$, where $\mathrm{T_{FI}}$ is the ordering temperature. The ratio $\theta_{C-W}/\mathrm{T_{FI}}$ is known as the frustration index (f) [1]. Systems whose magnetic geometry consists of planes of edge-sharing triangles, planes of corner-sharing triangles, pyrochlore-type 3D structures, Kagome lattice, and so on are known to show substantial geometric frustration (f $\gg$ 1). As discussed below, spinel oxides are among such systems.

1.4 Spinel oxides

Spinel oxides (AB_2O_4) are a fascinating class of materials that exhibit a host of complex physical properties that arise from geometric frustration [20]. A quick search through the literature yields several examples of highly frustrated spinel oxides, some of which are listed in Table 1.1.

Table 1.1. Some frustrated spinel oxides. Table adopted from [20].

Material	θ_{C-W} (K)	$\mathrm{T_{FI}}$ or $\mathrm{T_N}$ (K)	f	Ref.
MgV_2O_4	-600	45	14.3	[21–23]
ZnV_2O_4	-850	40	21.3	[24–27]
$ZnCr_2O_4$	-390	12.5	31.2	[26, 28]
$ZnFe_2O_4$	120	13	9.2	[29]
$CoCr_2O_4$	-650	93	6.99	[30, 31]
$MnAl_2O_4$	-143	40	3.6	[32]
$FeAl_2O_4$	-130	12	11	[32, 33]
$CoRh_2O_4$	-31	25	1.2	[33]

In a unit cell of a spinel oxide, which is displayed in Figure 1.9(a), 8 divalent A ions and 16 trivalent B ions reside in the tetrahedral (T) and octahedral (O) environments formed by 32 oxygen ions. Depending on the nature of the distribution of cations in the tetrahedra and octahedra sites, spinel oxides can be categorized into "normal" and "inverse" spinels. In a normal spinel, all T-sites are occupied by divalent ions and all O-sites are occupied by trivalent ions. Whereas, in an inverse spinel, the T-sites are occupied

by trivalent ions and the O-sites are randomly occupied by the remaining ions. In general however, the spinel oxides demonstrate some level of inversion, i.e. cation intermixing in the two sublattices. Therefore, the general chemical formula for a spinel oxide is written as $(A_{1-\alpha}B_{\alpha})_T[A_{\alpha}B_{2-\alpha}]_O O_4$, where the ions inside the parentheses are T-site ions, the ions inside the brackets are O-site ions, and α represents the *degree of inversion*, which can range from 0 (normal) to 1 (fully inverse) [10,11].

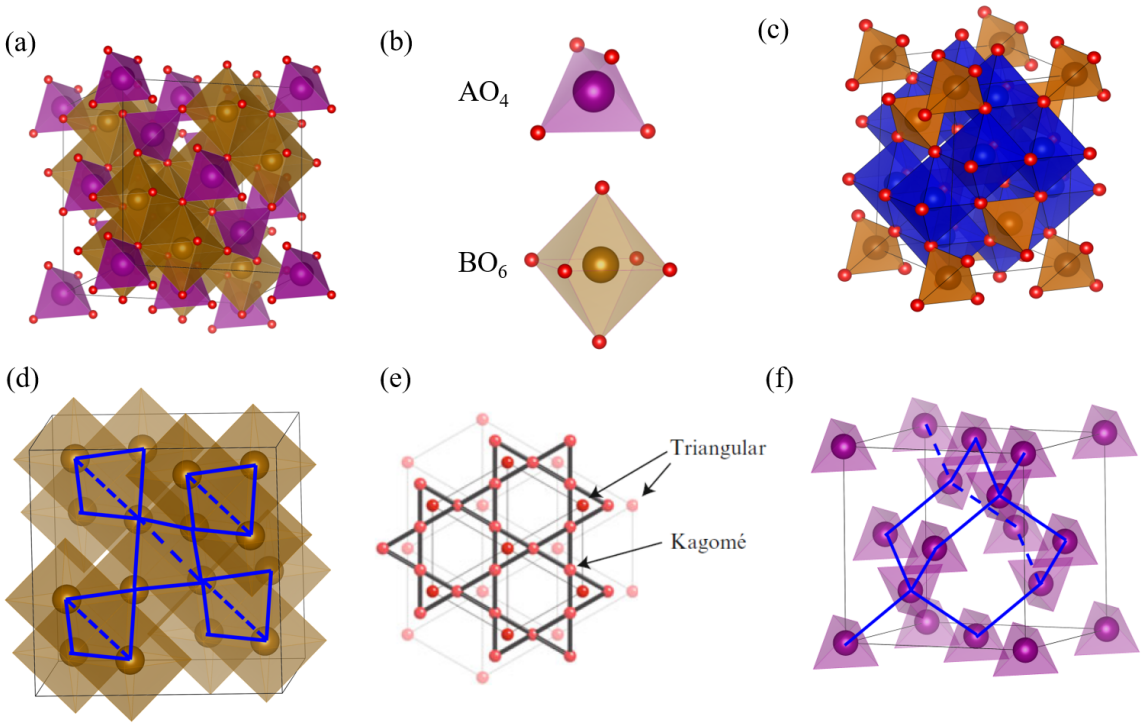

Figure 1.9. Spinel structure. (a) Unit cell of a cubic spinel oxide. (b) AO_4 and BO_6 structures. (c) Unit cell of a tetragonal spinel oxide. (d) Pyrochlore-like O-sublattice. (e) O-sublattice viewed from the [111] direction [20]. (f) Diamond-like T-sublattice.

The distribution of cations in spinels depend on several factors, such as their radii, Coulomb interactions, and crystal field effects on the octahedral site preference energy (OSPE). The OSPE energy is the difference in the crystal field between the octahedral and the tetrahedral environments. A greater absolute OSPE means it is energetically cheaper for the ions to occupy the octahedral sites. Table 1.2 shows the crystal field stable energy (CFSE) and the OSPE for some cations. The OPSE value of Fe^{3+} is 0, whereas that of

Fe^{2+} is -16.7 kJ mol^{-1}. So, in a spinel where Fe is present in both 2+ and 3+ oxidation states, the total energy is minimized when the Fe^{2+} ions are occupying the octahedral sites. This is the case in the inverse spinel Fe_3O_4, which has the cationic distribution of $Fe^{3+}[Fe^{3+}Fe^{2+}]O_4$.

Table 1.2. Number of 3d electrons, crystal field stable energy (CFSE), and octahedral site preference energy (OSPE) of some 3d transition metal ions. Values obtained from Refs. [34–36].

Cation	no. of 3d electrons	CFSE (kJ mol^{-1}) octahedral field	CFSE (kJ mol^{-1}) tetrahedral field	OPSE (kJ mol^{-1})	OPSE (eV)
Ti^{3+}	1	-87.4	-58.6	-28.8	-0.298
Mn^{3+}	4	-135.6	-40.2	-95.4	-0.988
Mn^{2+}	5	0	0	0	0
Fe^{3+}	5	0	0	0	0
Fe^{2+}	6	-49.8	-33.1	-16.7	-0.173
Ni^{2+}	8	-122.2	-36.0	-86.2	-0.893

As shown in Figure 1.9(d), within a spinel structure, the BO_6 octahedra chains form a three-dimensional network of corner-sharing tetrahedra known as the pyrochlore lattice, which can be highly frustrated [20]. This is due to their triangle-based geometry, which can be better seen from [111] direction (Figure 1.9(e)). The AO_4 tetrahedra form a corner-sharing diamond lattice, as shown in Figure 1.9(f). These are called O- and T-sublattices, respectively. The competition between the intra-sublattice exchange interactions (J_{TT} and J_{OO}) and inter-sublattice exchange interactions (J_{OT}) is responsible for the rich magnetic phase diagrams in these materials [20]. Therefore, based on the types of cations present in the T- and O-sites, magnetic or non-magnetic, there are three cases to consider.

1. Spinel oxides with magnetic O-site ions, like ACr_2O_4, show a significant geometric frustration [37]. This is because in the absence of a magnetic ordering in the T-sublattice, the main magnetic interaction is $J_{Cr\text{-}Cr}$ antiferromagnetic in the O-sublattice, leading to strong geometric frustration [37–39].

2. Spinel oxides with magnetic ions only in the T-sites are normally not supposed to be frustrated if only the nearest neighbor interactions are considered. However, in

some systems such as $CoAl_2O_4$ and $CoRh_2O_4$, the competition between the nearest and next nearest neighbor interactions can lead to magnetic frustration [20].

3. Spinel oxides with magnetic ions in both T- and O-sites also have a complex magnetic phase diagram. Generally, at high enough temperatures, the dominant interaction is that between the ions in T- and O-sublattices. Here, the spins in the two sublattices are antiparallel below the ordering temperature (T_{FI}), which together with the unequal number of tetrahedral and octahedral sites, generally results in a net ferrimagnetic[4] (FI) ordering [40–42]. At low temperatures, where all magnetic interactions become important, magnetic frustration can arise from their competition, resulting in quite complex magnetic behavior at low temperatures [43, 44].

1.4.1 Complex phase diagrams

Due to their unique geometry and the presence of competing interactions, magnetic spinel oxides demonstrate rich phase diagrams with multiple structural and magnetic phase transitions. For instance, MnV_2O_4, which has a FI ordering below 60 K, undergoes a collinear to non-collinear spin rearrangement below ∼52 K, where the V moments in the O-sites are canted by ∼65°, as shown in Figure 1.10(a and b) [43, 45]. Similarly, $CoCr_2O_4$ is reported to have a conical ferrimagnetic spin ordering at low temperatures, as displayed in Figure 1.10(c and d) [31]. Often times, the strong coupling between the orbital, spin, and lattice degrees of freedom in them gives rise to coupled phase transitions, like a magneto-structural phase transition. Therefore, it is not unusual to find spinels with large magnetodielectric and magnetoelastic couplings at low temperatures where the system is in a frustrated state. Table 1.3 contains a list of a few representative spinel oxides that undergo multiple phase transitions (magnetic, structural, etc).

[4]The magnetic susceptibility above T_{FI} follows the two sublattice model described by Eq. (1.15), where the Curie constant C is the sum of the Curie constants of T- and O-sublattices, i.e. $C = C_O + C_T$. Since the Curie constant is related to the effective magnetic moment (μ_{eff}) as $C \sim \mu_{eff}^2$, the effective moment of the system is given by $\mu_{eff}^2 = \mu_O^2 + \mu_T^2$ [7].

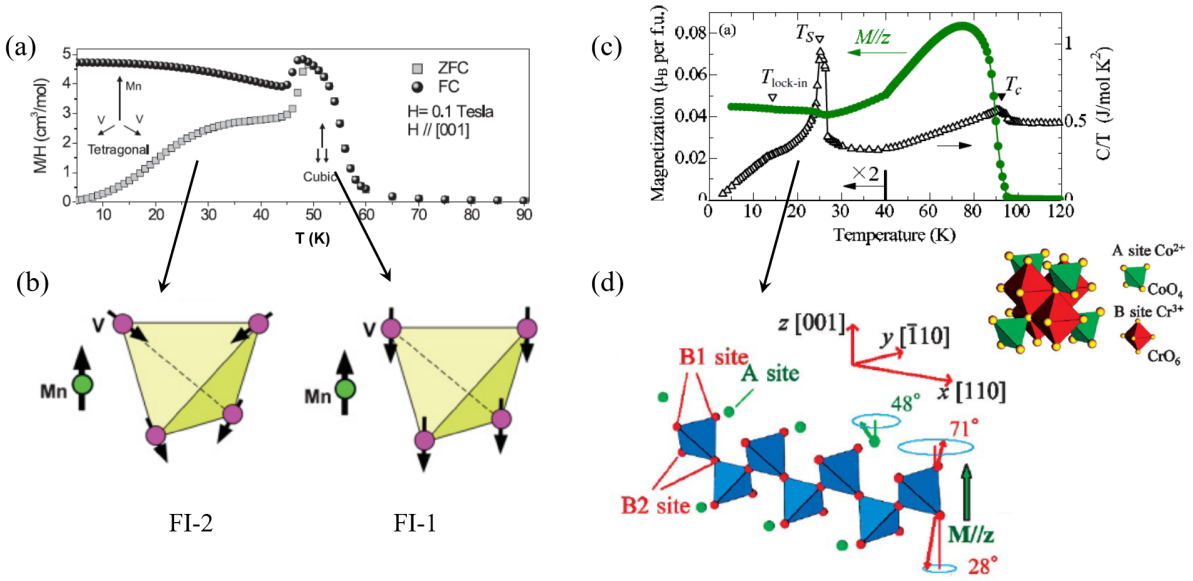

Figure 1.10. Complex magnetic phases in some spinel oxides. (a) $\chi = M/H$ as a function of temperature in MnV_2O_4 showing two transitions. (b) Arrangment of V moments in O-sublattice in the collinear (FI-1) and canted (FI-2) ferrimagnetic phases in MnV_2O_4. (c) Magnetization and specific heat as function of temperature in $CoCr_2O_4$ showing phase transitions. (d) Conical ferrimagnetic arrangement of spins in both O- and T-sublattices in $CoCr_2O_4$. Inset shows the position of Co and Cr in the lattice. Images adapted from [31, 43, 45].

Table 1.3. Multiple phase transitions in spinel oxides. $T_{FI\text{-}1,2,3}$ are magnetic transition temperatures and T_s is structural transition temperature.

Spinel	$T_{FI\text{-}1}$ (K)	$T_{FI\text{-}2}$ (K)	$T_{FI\text{-}3}$ (K)	T_s (K)	Ref.
MnV_2O_4	60	52	-	52	[43, 45]
$MnCr_2O_4$	51	45	14	14	[38]
$CoCr_2O_4$	93	86	13	24	[31]
FeV_2O_4	110	70	-	140, 110, 70	[46]
Mn_3O_4	42	39	33	1443	[47, 48]

1.4.2 Iron-based spinel oxides

Spinel ferrites, or iron-based spinel oxides, have garnered a significant amount of interest due to their wide range of technological applications. In nano-form, they have shown promising results as catalysts, gas and humidity sensors, magnetic drug delivery agent, water treatment agent, and so on [49]. Recent research has also highlighted their potential for spintronics applications as spin filters [50].

Spinel ferrites ($M_xFe_{3-x}O_4$, where M = transition metal ions) are spinel oxides that are derived from magnetite (Fe_3O_4). In addition to being one of the most magnetic naturally occurring minerals on Earth [51, 52], Fe_3O_4 is well-known for undergoing a first-order metal-to-insulator and structural transition at ∼124 K, known as Verwey transition, the mechanism of which is still perplexing [53, 54]. Fe_3O_4 has an inverse spinel structure with all of its T-sites occupied by Fe^{3+} ions and O-sites occupied by randomly distributed Fe^{2+} and Fe^{3+} ions, as shown in Figure 1.11(a). Magnetically, the most important interaction in magnetite is the antiferromagnetic interaction between the iron ions in the O- and T-sublattice. Since the O-sublattice contains both Fe^{2+} ($3d^6$) and Fe^{3+} ($3d^5$) ions, these ions are aligned ferromagnetically via a double exchange interaction [6], as shown in Figure 1.11(b). On the other hand, the Fe ions on the T- and O-sublattices are coupled via an antiferromagnetic superexchange interaction [6]. This results in a ferrimagnetic state. Replacing Fe by another magnetic ion in one or more lattice sites can thus distrupt this delicate arrangement, as it will result in additional exchange interactions of comparable strengths. This provides an excellent platform to study the physics of magnetic frustration and is the main motivation behind this dissertation.

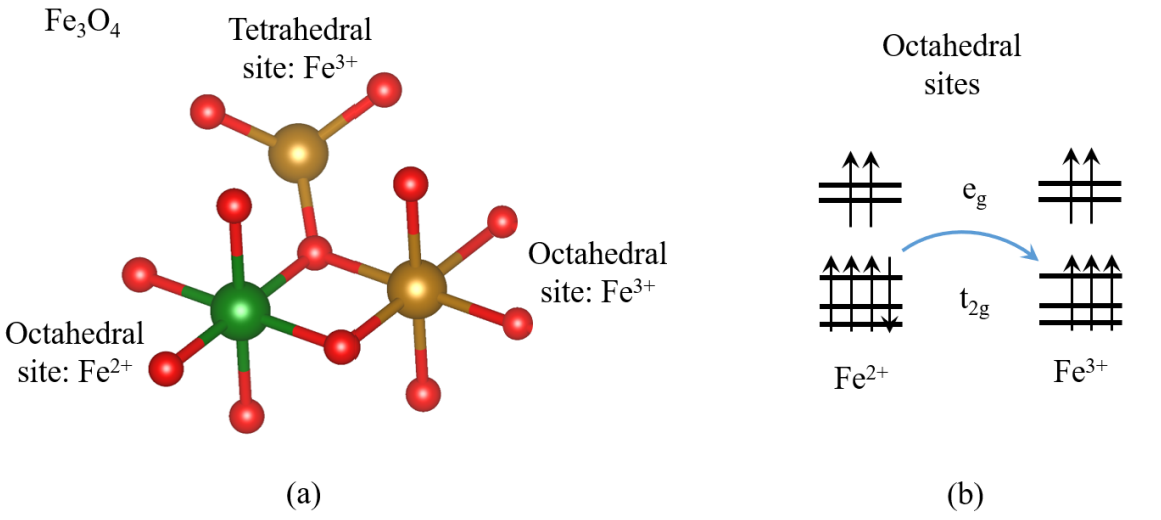

Figure 1.11. (a) Atomic arrangement in Fe_3O_4. (b) Double exchange interaction in the octahedral sites.

In this work, our aim is to investigate the properties of three spinel oxides derived from magnetite by partial replacement of iron by two other 3d magnetic cations, manganese and nickel, namely $FeMn_2O_4$, $MnFe_2O_4$, and $NiFe_2O_4$. The former two belong to a sub-family of spinel ferrites called manganese ferrites, where both Mn and Fe can oxidize in 2+ and 3+ states, potentially leading to complex magnetic landscapes. By growing large single crystals of $FeMn_2O_4$ and $MnFe_2O_4$ and measuring their physical properties, we observed that both of these materials undergo multiple phase transitions. The results from these two studies are presented in Chapters 3 and 4, respectively. To further extend our research into frustrated magnetism, we utilized single crystals $NiFe_2O_4$ with naturally occuring self-assembled NiO microstructures. This system provided us a novel avenue to study interface-induced magnetic phenomena. By combining our bulk physical properties measurements and microscopic studies, we were able to identify a spin glass state at the interface. These results are presented in Chapter 5.

Chapter 2
Experimental Procedure

In this chapter, a brief description of the experimental procedures employed in this dissertation is presented, including sample preparation, characterization methods, and instrumentation.

2.1 Sample preparation

A systematic investigation of the intrinsic properties of materials often requires large single crystal samples with minimal impurities. Often a material system can have directional anisotropic properties. For example, a layered material can be metallic along the in-plane direction and be semiconducting in the perpendicular direction. Such directional anisotropies can only be observed in single crystal samples because their effects on the properties are smeared in polycrystal samples due to the presence of many tiny crystallites with random orientations. Therefore, growing single crystals of a material is preferred whenever possible. There are several techniques that are used to obtain single crystal materials, such as flux method, melt method, travelling solvent method, and so on. While most of these techniques yield decent sized ($\sim$ mm) crystals, floating zone method is known best for its ability to produce large single crystals, often several centimeters long and several millimeters wide. Large crystals are desirable for several experimental techniques that rely on large sample size, such as neutron diffraction, thermal conductivity, and specific heat. Additionally, the crystals grown via this method are immune from external impurities as the crystals are grown without being in contact with any foreign objects such as a crucible. Floating zone method of crystal growth is a two-step process. In the first step, a polycrystalline sample is synthesized, which is used in the second step to grow the single crystal samples.

2.1.1 Synthesis of polycrystalline samples

We employ solid-state reaction method to synthesize the polycrystalline samples from a mixture of solid precursors. Depending on the nature of the final product that is sought,

the solid precursors can be pure elements or chemical compounds, such as oxides and carbonates. Solid state reaction is a diffusive process and takes place in a long-time scale, usually over several days. The reaction time can be reduced by increasing the reaction temperature and increasing the surface area of the reactants by grinding them into fine powder. Although a higher temperature is desirable for the reaction, a careful tailoring of the reaction temperature is needed to avoid the formation of impurity phases. The reaction atmosphere can also be controlled to avoid formation of impurity phases.

For spinel oxides, a mixture of high purity binary oxides with a desired molar ratio is hand-ground using a mortar and pestle and loaded in an alumina (Al_2O_3) crucible. The crucible is placed inside a programmable box furnace and heated to the reaction temperature, kept at that temperature for a desired amount of time, and then cooled. In some cases, the mixture is rapidly cooled in order to avoid forming secondary phases at intermediate temperatures. This is done by quenching the reaction mixture by submerging it in cold water or liquid nitrogen. After cooling, the mixture is re-ground and its purity is checked via x-ray diffraction (XRD). The process is repeated until the reaction is fully complete and the end product is impurity-free.

2.1.2 Single crystal growth

In this work, we utilize a two-mirror optical floating zone (FZ) furnace from Canon Machinery Inc. (model SC1MDH-20020), shown in Figure 2.1(a). The FZ furnace consists of two co-focused ellipsoidal mirrors with two halogen lamps placed at the second focal points of the mirrors, as shown in the schematic diagram in Figure 2.1(b). The ceramic rods, known as the feed rod (upper) and the seed rod (lower), are mounted in such a way that their tips meet at the mutual focal point of the mirrors. By increasing the power in the lamps, the tips of the ceramic rods are melted and brought together to establish a melt zone. Once established and stabilized, the melt zone is moved up by lowering the seed and feed rods in a controlled manner. As the melt zone moves up, the liquid at the bottom of the zone cools and the material crystallizes on top of the seed rod. During the growth,

the two rods are rotated in the opposite direction to increase the homogeneity in the melt zone. After the completion of the growth process, the power in the lamp is slowly lowered to separate the feed rod and the crystal. The furnace is also equipped with a gas line that can be used to control the growth atmosphere by flowing a desired mixture of gas through the line as well as maintain a pressure of up to 1 mega Pascals.

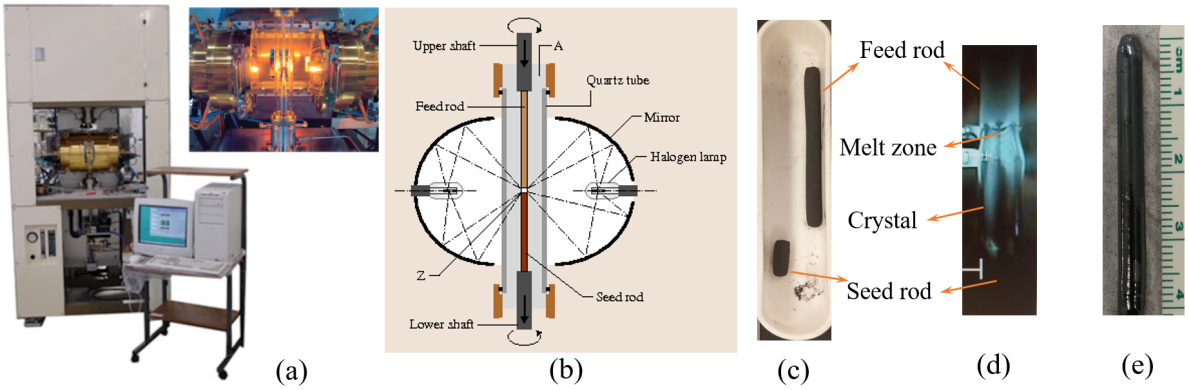

Figure 2.1. Sample preparation techniques. (a) Canon Machinery Inc. Model SC1MDH 20020 two-mirror optical floating zone furnace. (b) Schematic of the two-mirror furnace. Adapted from Ref. [55]. (c) Hydrostatically pressed ceramic rods. (d and e) Picture of a single crystal during and after the growth process, respectively.

The feed and seed rods used in this step are prepared using the polycrystalline product from the solid-state reaction. The polycrystalline material is ground thoroughly and loaded into a rubber balloon of diameter about five millimeters and packed using a glass rod. Once the balloon is packed up to the desired length, it is tied, ensuring no air bubble is present inside it. The tied balloon is then placed inside a hydrostatic press and subjected to a pressure of 50 mega Pascals for 10-15 minutes. The balloon is then carefully removed from the press, and the resulting polycrystalline rod is obtained by surgically cutting the balloon down its length. The obtained polycrystalline rods are placed on an alumina boat and sintered at high temperature to further densify them. The polycrystalline rods obtained in this way are straight and dense enough to properly align them in the optical floating zone and establish a stable melt zone.

2.2 Structural analysis

2.2.1 X-ray diffraction

The first step towards exploring the physical properties of single crystals is to determine their structure. The periodic arrangement of atoms in a crystal enables us to probe the crystal structure with diffraction experiments, such as x-ray diffraction. The x-ray diffraction geometry is shown in Figure 2.2(a). As the incident x-ray beam interacts with the sample, the diffraction peaks are obtained at the detector as a result of the constructive interference of the x-rays reflected from the successive planes. The positions and intensities of the diffraction peaks are determined by the crystal structure of the material according to the Bragg's condition $n\lambda = 2dsin(\theta)$, where n is the peak order, λ is the wavelength of x-ray, θ is the semi-angle of diffraction, and d is the distance between the two successive planes along the normal direction. At a given diffraction normal direction, there are several planes that can produce constructive interference of x-rays. Such planes are indexed by Miller indices hkl which are used to calculate the lattice spacing d. For example, for a tetragonal crystal with lattice constants a $(= b)$ and c, the lattice spacing is given by $1/d^2 = (h^2 + k^2)/a^2 + l^2/c^2$. Therefore, the positions of the diffraction peaks can be used to identify the lattice spacing and consequently the crystal structure of a sample.

In this work, we employ a PANalytical Empyrean X-ray Diffractometer, shown in Figure 2.2(b), to perform powder x-ray diffraction (XRD) at room temperature to decipher the crystal structure. This instrument is equipped with a copper x-ray source which produces K_α radiation with a wavelength of 1.5418 Å. Both polycrystalline and single crystal samples can be characterized using this instrument. For polycrystalline samples, a small compact layer of sample is loaded on a zero-background sample holder. The holder is placed inside the instrument and the XRD pattern is collected as a function of diffraction angle 2θ, while rotating the holder to get a homogenous signal. The crystal structure can then be determined by comparing the XRD pattern to the standard pattern (PDF files) from the International Center for Diffraction Data (ICDD) database.

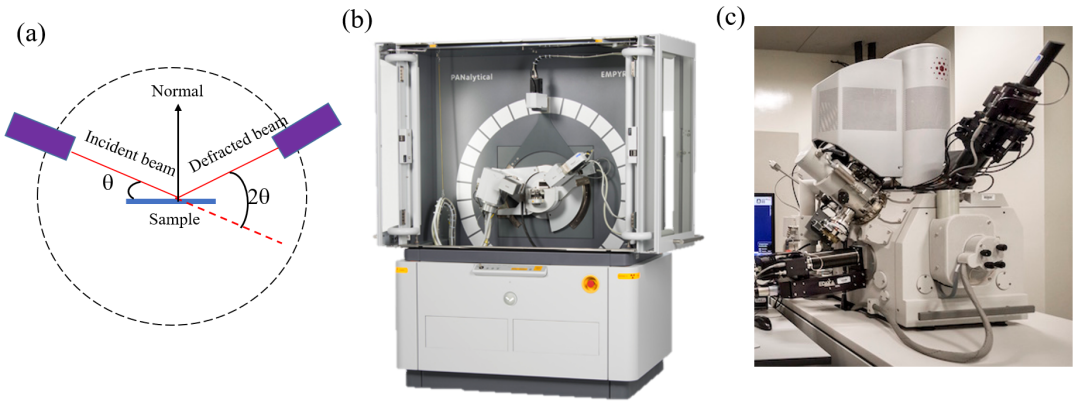

Figure 2.2. Structural and chemical characterization techniques. (a) X-ray diffraction geometry. (b) PANalytical Empyrean x-ray diffractometer. (c) FEI Quanta 3D with EDS.

The orientation of a large single crystal sample can also be determined using this instrument. To do so, the single crystal is fixed on the sample holder with the crystal plane of interest parallel to the sample holder, and the 2θ scan is performed. The resulting XRD pattern will contain diffraction peaks from the family of the corresponding planes only. By comparing this pattern with the pattern from a powder sample, the orientation of the single crystal can be determined with ease.

2.2.2 Neutron diffraction

The principle of neutron diffraction is similar to that of x-ray diffraction, as both of these techniques rely on the scattering of an incident beam by the ordered arrangement of scattering sites in the crystal. While both of these techniques can provide the crystallographic information of a specimen, neutron diffraction provides additional information due to the magnetic moments ($s = \frac{1}{2}$) they carry. In a neutron diffraction experiment, a beam of neutrons is incident upon a sample and is scattered by both the atoms on the lattice sites as well as the magnetic moments. In a paramagnetic solid where there is no long-range magnetic order, the neutron diffraction peaks contain information about the crystal structure. However, in a magnetically ordered solid, the diffraction peaks are the sum of lattice peaks and magnetic peaks. Provided there are no structural changes, the peak intensities

of the lattice peaks remain constant at all temperatures. Therefore, by performing neutron diffraction on a solid as a function of temperature and mapping out the change in the peak intensities, one can determine the magnetic transition temperature. In addition, by refining the magnetic plus structural peaks, the spin arrangement in the lattice can also be resolved. The neutron diffraction measurements in this work were performed at Oak Ridge National Laboratory (ORNL). We use neutron powder diffraction measurements to study both the crystallographic and magnetic structures of our samples.

2.2.3 Energy dispersive x-ray spectroscopy

We determined the chemical composition of the samples via energy dispersive x-ray spectroscopy (EDS or EDX). In this technique, a focused beam of high-energy electrons or x-rays is incident on a sample and the x-rays emitted from the sample due to the interaction with the electrons are analyzed to obtain the elemental composition of the sample. EDS is a counting experiment. When a photon excites an electron (with energy E_1) in an inner shell of an atom, a hole is created in that shell. This hole is filled by a higher energy shell electron with energy E_2. During this process, the excess energy $E_2 - E_1$ is emitted as a characteristic photon. The energies of the emitted x-rays are therefore characteristic of the atomic structure of the emitting element. Hence, by counting the number of photons with a given energy and comparing it with the total number of photons emitted, the relative proportions of the elements in the sample can be obtained. To accurately determine the composition of a sample, x-rays can be collected from several points or areas on the sample to get an average value.

In this work, we used a FEI Quanta 3D system equipped with EDS in the Shared Instrument Facility at LSU, which is photographed in Figure 2.2(c). This EDS measurement setup is built up on a scanning electron microscope (SEM). SEM is a type of electron microscope which creates the topographical images of a sample by focusing a high energy electron beam on the sample surface and detecting the backscattered electrons. A representative SEM image of a sample and the EDS spectra are shown in Figure 2.3.

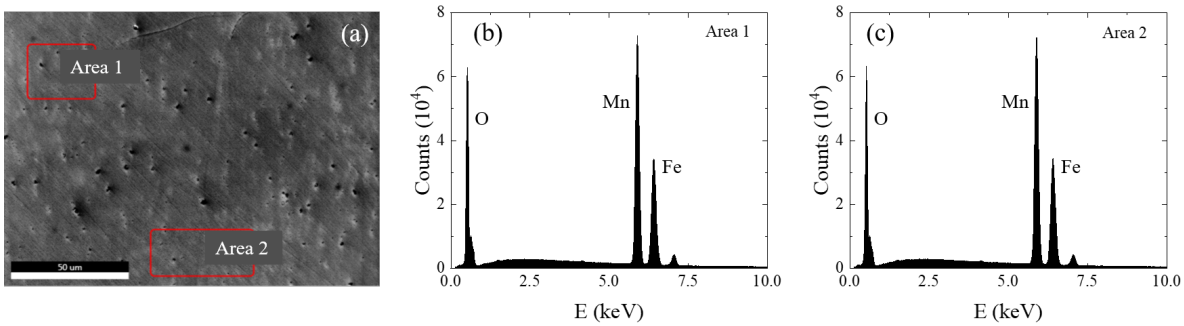

Figure 2.3. Examples of SEM and EDS measurements. (a) SEM image of a polished single crystal. (b and c) EDS spectra obtained from the selected areas in (a).

2.3 Physical properties measurements

After carefully determining the structure and chemical composition of the single crystals, their physical properties are measured. For this, we utilize the Physical Properties Measurement System with a 14 Tesla magnet (PPMS-14T) and the Magnetic Properties Measurement System with a 7 Tesla magnet (MPMS-7T) made by Quantum Design Inc. The following sections briefly outline the procedure involved in measuring these properties.

2.3.1 Magnetization

The magnetization of the single crystal samples is measured using both PPMS and MPMS. The MPMS is used to measure low temperature magnetization measurements (1.85 K to 400 K) and the PPMS with a Vibrating Sample Magnetometer (VSM) is used for high temperature measurements (300 K to 1000 K). The MPMS is a superconducting quantum interference device (SQUID) based magnetometer, whereas the VSM is a traditional Faraday coil magnetometer.

The MPMS, shown in Figure 2.4(a), consists of a superconducting magnet, which is kept cool using liquid helium, a superconducting detection coil, and a SQUID connected to the detection coil [56]. The detection coil and the magnet are arranged in concentric circles around the central sample chamber of the MPMS. To measure the magnetization of a sample in this setup, the sample is mounted in a minimal background plastic drinking straw, as shown in Figure 2.4(b). The straw is attached to a sample rod and inserted into

the sample chamber. While inside the MPMS sample chamber, the sample rod can be moved through the detection coils. Before the measurement is started, the sample must be centered at the detection coil by performing a centering scan to ensure the sample is at the middle of the detection coils (Figure 2.4(c)). As the sample is moved vertically along the sample space through the pickup coils, the MPMS reads the output voltage of the detector circuit as a function of the sample's position in the coils. At each position, several voltage readings are recorded and averaged to improve the accuracy. The voltage readings are used to compute the magnetic moment of the sample based on the principles of SQUID, which is described below.

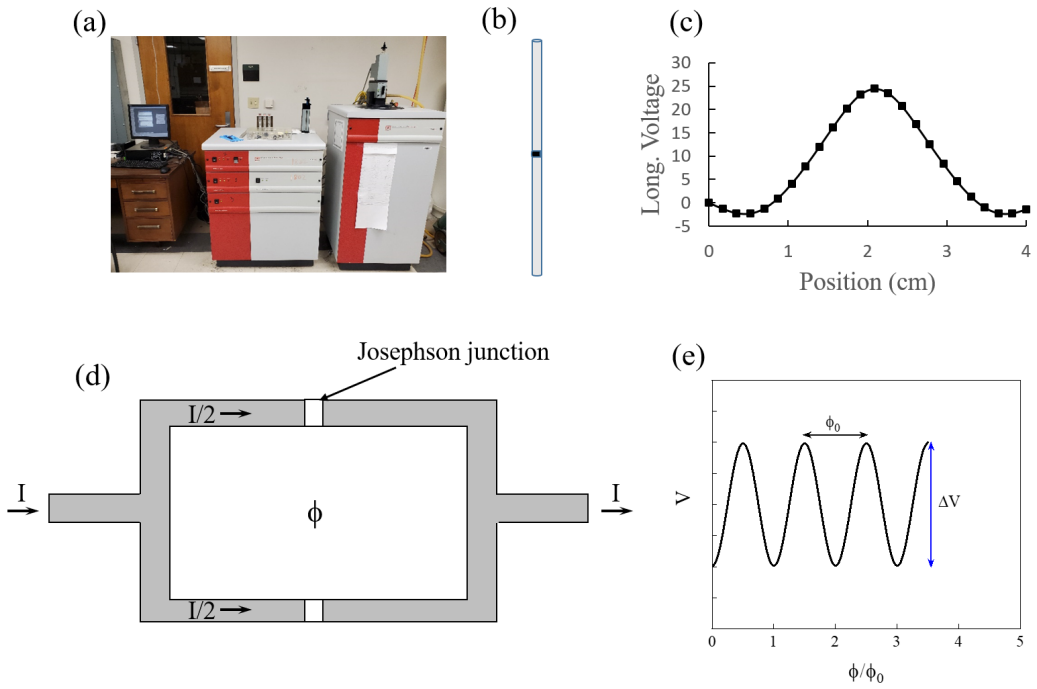

Figure 2.4. Magnetic Properties Measurement System. (a) Quantum Design MPMS with a 7 Tesla magnet. (b) A plastic drinking straw with a sample (black) in it. (c) A voltage profile of a good centering scan. (d) schematic of a superconducting quantum interference device. (e) Periodic voltage response due to an external flux through a SQUID.

A Superconducting Quantum Interference Device (SQUID) is a closed loop with two parallel Josephson junctions, as shown in the schematic in Figure 2.4(d). A Josephson junction is two superconductors separated by a thin insulating layer. In this arrangement, the superconducting Cooper pair of electrons can tunnel through a thin enough barrier of

non-superconducting material. This phenomenon, known as the Josephson effect, is named after Brian David Josephson, who predicted it in 1962 and received the Nobel Prize for it in 1973. The Josephson effect can be summarized by the following two equations:

$$I_J = I_0 sin(\delta) \tag{2.1}$$

and

$$V = \frac{\phi_0}{2\pi}\frac{d\delta}{dt}. \tag{2.2}$$

Here, I_J is the tunneling current flowing through the junction, I_0 is the critical current, δ is the phase difference, V is the voltage across the junction, and ϕ_0 is the flux quantum ($= \frac{h}{2e}$).

In addition to the Josephson effect, the working principle of a SQUID also relies on the fact that the magnetic flux enclosed by a superconducting loop must be an integer number of the flux quanta. When a dc current I is passed through a SQUID loop, it splits equally between the two sections, as shown in Figure 2.4(d). If a small magnetic field is applied to the loop, a screening current I_s is induced, generating a magnetic field opposite to the applied field to keep the total magnetic flux through the loop constant. This results in the total current flowing through the two branches to be $I/2 + I_s$ and $I/2 - I_s$. If either of these currents are greater than the critical current of the Josephson junction, a voltage is generated across the loop. If the applied magnetic field is further increased so that the external flux is bigger than $\phi_0/2$, then it is energetically favorable for the loop to induce a current I_s such that the total flux inside the loop increases from $n\phi_0$ to $(n+1)\phi_0$. As the external flux is further increased, the screening current I_s starts to decrease and becomes zero when the external flux is exactly equal to one flux quantum. This behavior results in a periodic nature of the external field dependence of I_s. By operating the SQUID in a resistive mode, i.e. by having $I > I_c$, and measuring the voltage V across the loop as a function of the applied magnetic field, a characteristic voltage versus magnetic field curve

can be obtained, as shown in Figure 2.4(e). Thus, a voltage reading across the SQUID can be converted into the magnetic flux and then converted to the magnetic moment of the sample.

In contrast to the MPMS, PPMS utilizes a *vibrating sample magnetometer* (VSM) to measure the magnetization of a sample [57]. The basic operating principle of a VSM is governed by Faraday's law of magnetic induction, i.e. a change in the magnetic flux ϕ through a closed loop of wire induces a voltage in the loop $V_{induced}$. This induced voltage is proportional to the rate of change of the magnetic flux, $V_{induced} = \frac{d\phi}{dt}$. To measure the magnetization in a sample, it is placed inside the pickup coils and oscillated at a fixed frequency while measuring the resultant voltage in the pickup coils. The VSM option in PPMS consists of a linear transport motor which is capable of vibrating the sample with an oscillation amplitude of up to 3 mm at a frequency of 40 Hz. It is also equipped with an "oven," which is a sample stick with a built-in heater and thermometer. The oven is capable of heating the samples up to 1000 K. Since this option does not utilize a SQUID device to measure the magnetization, the measurements are less accurate than those from the MPMS. In this work, we mostly rely on the MPMS for magnetization measurement and only use VSM for high temperature measurements.

2.3.2 AC magnetic measurement

In a dc magnetic measurement, the magnetization of a sample is measured by applying a constant dc magnetic field. This measurement yields the equilibrium value of the magnetization in the sample. If the sample in consideration has a dynamic magnetization, then ac magnetic measurements are preferred. In ac measurements, a small ac driven magnetic field is superimposed on the background dc magnetic field [58]. By applying the ac field to a sample, the time-dependent sample moment can be measured, which provides information about the magnetization dynamics in the sample. For the ac measurements, a pickup circuitry is configured to detect ac magnetization in only a narrow frequency band around the fundamental frequency of the ac field [58]. Because the ac field is time dependent, the

measured magnetization of the sample will often lag behind the field. As a result, the ac measurements produce two physical quantities: the magnitude χ and the phase shift ϕ. In practice, the ac susceptibility is written in terms of its two components as

$$\chi' = \chi \cos\phi \qquad \chi'' = \chi \sin\phi \tag{2.3}$$

$$\chi = \sqrt{\chi'^2 + \chi''^2} \qquad \phi = \tan^{-1}(\chi''/\chi'). \tag{2.4}$$

The two components are called the in-phase component (χ') and the out-of-phase component (χ'') and are also known as the real and imaginary parts of susceptibility, respectively. Both χ' and χ'' are useful to extract information about the dynamic processes and phase transitions.

2.3.3 Specific heat

PPMS-14T, photographed in 2.5(a), was used to measure the thermal and electrical properties. It is a modular measurement system which provides various measurement "options," such as resistivity, thermal conductivity, and heat capacity. In addition to the options, a breakout box can be used to connect external electronics to setup a desired experiment. Such versatility, a large magnetic field of 14 Tesla, and an operable temperature range of 1.85 to 400 K makes PPMS an important tool in the experimental study of materials.

The specific heat of a material provides important information about its structural (lattice), electronic, and magnetic properties, as well as its phase transitions. The Heat Capacity (HC) option in PPMS allows for the measurement of the specific heat at a constant pressure (C_p). This is done by controlling the heat added to and removed from a sample while monitoring the resulting change in the sample temperature [59]. Figures 2.5(b and c) show a picture and a schematic diagram of the heat capacity sample puck, respectively. A platform heater and platform thermometer are attached to the bottom side of the sample platform, which is supported by the wires connecting the heater and thermometer to the

puck. A small layer of grease is applied on the platform to attach the sample as well as to provide thermal contact between the sample and the platform. Once the sample puck is inserted inside the sample chamber of the PPMS, a high vacuum ($\sim 10^{-6}$ Torr) is created inside the sample chamber by using a cryopump. This is done to minimize the heat loss to the environment.

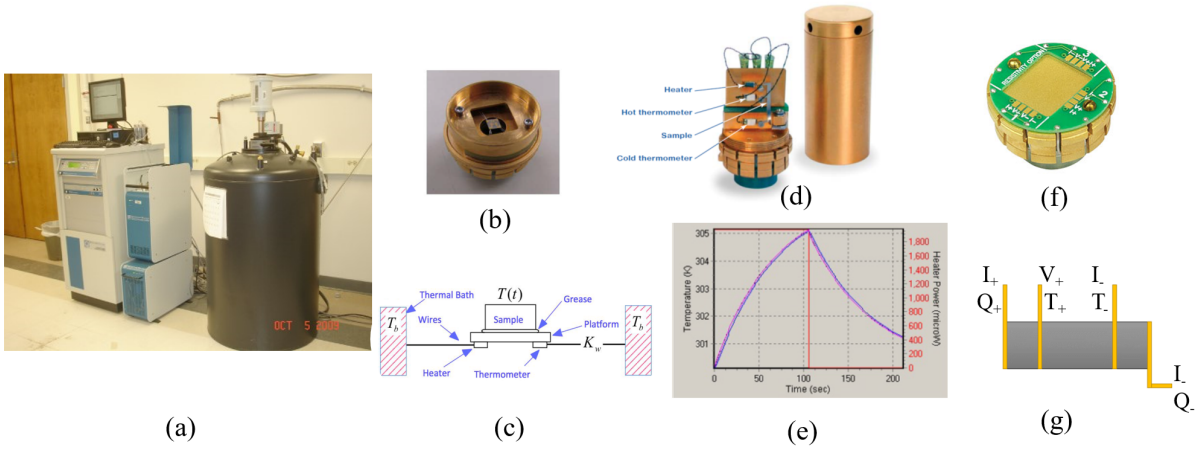

Figure 2.5. Physical Properties Measurement System. (a) A photograph of Quantum Design PPMS with 14 Tesla magnet with a temperature range of 1.85 K to 400 K [60]. (b) Sample puck for heat capacity option. (c) Schematic of heat capacity puck sample stage. (d) Sample puck for thermal transport option. (e) Temperature profile of a sample during a thermal property measurement. (f) Sample puck for dc resistivity option. (g) Four-point contact method of transport measurement. (b - f) were adapted from PPMS users' manuals [59, 61, 62].

The PPMS HC option uses a relaxation technique to measure C_p. In this technique, a measurement cycle consists of a heating period, where a known amount of heat is supplied to the sample platform at a constant power for a fixed time, and a cooling period of the same time duration, where the heat supply is cut off. After each measurement cycle, the HC option fits the entire temperature response of the sample to a model that accounts for the thermal relaxation of the sample, the platform, and the puck [59] to compute the specific heat. In this model, the time dependence of the platform temperature T obeys the following equation:

$$C_{total}\frac{dT}{dt} = -K_w(T - T_b) + P(t). \tag{2.5}$$

Here, C_{total} is the total heat capacity of the sample and the platform, K_w is the thermal conductance of the wires, T_b is the temperature of the puck, and $P(t)$ is the power applied by the sample heater, which is P_0 during the heating period and zero during the cooling period. The solution to Eq. (2.5) is an exponential function with a characteristic time constant $\tau = C_{total}/K_w$, displayed below

$$T(t) = T(0)(1 - Ae^{-\frac{t}{\tau}}), \tag{2.6}$$

where A is a constant. A typical temperature profile obtained during a measurement cycle is shown in Figure 2.5(e). By fitting Eq. (2.6) to the experimental temperature profile, the specific heat is obtained from the time constant. To calculate the sample specific heat, the measurement process is done twice over the desired temperature range—first to determine the $C_{addenda}$ with no sample placed on the platform (i.e. only puck and grease) and then to determine the C_{total} with the sample mounted on the platform. The specific heat of the sample is computed by subtracting $C_{addenda}$ from C_{total}, i.e. $C_p = C_{total} - C_{addenda}$.

2.3.4 Thermal and electrical transport

The Thermal Transport Option (TTO) in PPMS is used to measure the thermal conductivity (κ) and thermopower (S) of the samples [61]. A TTO sample puck with a standard sample is shown in Figure 2.5(d). For the measurement, a rectangular-shaped sample of the desired dimensions is cut from the single crystal and four copper leads are attached to it with the help of conductive silver epoxy, as shown in Figure 2.5(g). The two end leads are connected to the heater and the cold bath, whereas the inner two leads are connected to two thermometers capable of measuring both temperature and voltage. Once again, the measurement is done in a high vacuum environment. During the measurement, a known amount of heat is applied to the sample for time t and the temperatures T_+ and T_- as well as Seebeck voltage ($\Delta V = V_+ - V_-$) are measured. In the simplest terms, the thermal conductance (K) and thermopower are calculated as $K = Q/(t\Delta T)$ and $S = \Delta V/\Delta T$,

where $\Delta T = T_+ - T_-$. κ is then calculated based on the known dimensions of the sample as $\kappa = K * \Delta l/A$, where Δl is the distance between the thermometer leads and A is the cross-sectional area of the sample.

The electrical resistivity of the samples is measured using the DC Resistivity option of the PPMS [62]. Four platinum wires are attached to the sample using silver epoxy in the four-probe configuration. The sample is then mounted onto the sample puck (Figure 2.5(f)) and inserted into the PPMS sample chamber. With the sample chamber evacuated, a known current (I) is sent through the sample using the outer two wires and the voltage drop (ΔV) across the inner two leads is measured. From Ohm's law, the sample resistance (R) is calculated as $\Delta V/I$. The sample resistivity (ρ) is then calculated as $\rho = RA/l$, where l is the separation between the two voltage leads and A is the cross-sectional area of the sample.

The DC resistivity option in PPMS is capable of measuring resistances up to a few $M\Omega$. To measure the resistivity of highly insulating samples, a Keithley 2001A electrometer is used in conjunction to the PPMS's temperature controller. Keithley 2001A is capable of measuring much higher resistances ($\sim G\Omega$) [63].

2.4 Microscopic measurements

In the macro-scale or bulk measurement techniques, such as magnetization measurements and neutron scattering, the measured quantities are averaged over a large number of unit cells. Such averaging of properties prevents us form truly understanding the micro-scale properties of the material. In fact, in such studies, small-scale imperfections and inhomogeneities are often over-looked. This can be problematic because interpreting the bulk properties require a use of theoretical models developed under the assumption of no imperfections. Therefore, a microscopic study that can gap the bridge between the nano-scale, i.e. spin structure, and macro-scale, i.e. magnetization, is tremendously helpful in understanding the true magnetic properties of a material.

The generally accepted value for the resolving power of human eyes is about 0.1-0.2 mm, and therefore, any instrument that can resolve details finer than 0.1 mm could be described as a microscope [64]. The resolution of a visible-light microscope can be approximated by the Rayleigh criterion $\delta = \frac{0.61\lambda}{\mu sin(\beta)}$, where λ is the wavelength of the light, μ is the refractive index of the medium, and β is the semi-angle of collection of the magnifying lens. For a green light with a wavelength of about 500 nm, which is in the middle of the visible spectrum, the theoretical resolution can be at best about 300 nm. Although, much better than the resolution of our naked eyes, 300 nm is still far too large in the atomic scale and corresponds to about 1000 atoms. Thus, many atomic scale features that are of interest in condensed matter physics are too small to resolve using a visible-light microscope. To resolve such details, scientists have developed several non-optical techniques, such as electron microscope, scanning tunneling microscope, and scanning probe microscope, that are capable of obtaining images at atomic scale. In this work, we used two such techniques to complement our bulk properties measurements: transmission electron microscope and magnetic force microscope.

2.4.1 Transmission electron microscopy

Electron microscopes, such as TEM, are made possible due to the wave-like nature of electrons, which was first theorized by Louis de Broglie and experimentally verified by Davisson and Germer and Thomson and Reid through electron-diffraction experiments [65, 66]. According to de Broglie's equation, the wavelength of electrons is related to their energy E as $\lambda = \frac{1.22}{\sqrt{E}}$, where the energy is in eV and the wavelength is in nm. For a 100 keV electron, the wavelength is about 0.004 nm, much smaller than the size of an atom. The Airy disk radius, which gives the theoretical resolution of an electron lens, is given by $r_{theory} = 1.22\frac{\lambda}{\beta}$, where β is the diameter of the aperture. A higher resolution can be achieved by lowering λ or increasing β. In practice, the resolution is limited by several factors, such as spherical aberration and chromatic aberration [64].

When an incident high-energy electron beam interacts with a sample, the ionizing radiation from the electrons produce a wide range of secondary signals from the sample, as shown in Figure 2.6. Many of these signals can be used to extract information about the structure and composition of the sample. For example, the secondary electrons (SE) are used to image the surface topography of the sample in SEM. TEM, on the other hand, relies on the transmitted electrons that go through the sample, which is known as the direct beam. As the electron beam interacts with the sample, the electrons are diffracted by the sample, which allows us to obtain the diffraction patterns or an image in the viewing screen.

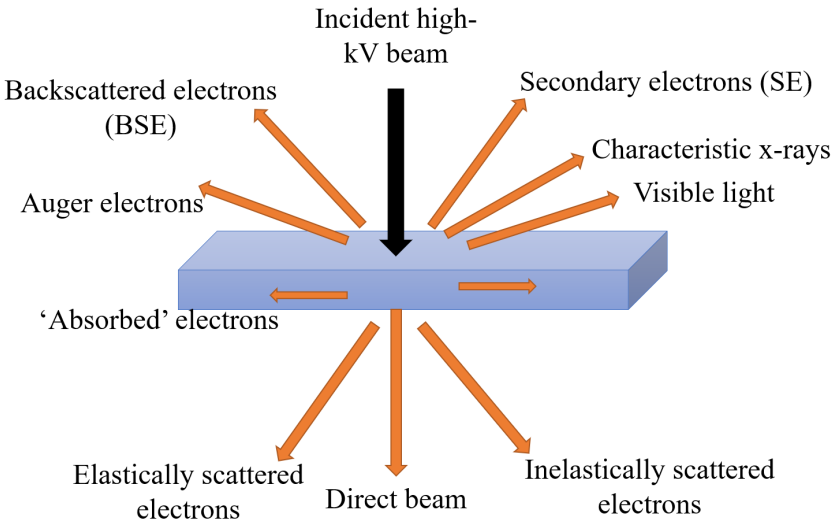

Figure 2.6. Signals generated from the interaction of a high-energy electron beam with a sample. Figure adapted from [64].

The schematic of the working principle of TEM is displayed in Figure 2.7. There are two modes of operation. In the imaging mode, the direct electron beam goes through the objective aperture and then through the intermediate lens, which is situated in the image plane of the objective lens, before being projected on the screen. This procedure results in the real space imaging of the specimen. In the diffraction mode of operation, the objective aperture is removed, and the direct beam is passed through the selected area aperture and then through the intermediate lens, which is located in the back focal plane of the objective lens, before being projected on the screen. This mode results in the diffraction

pattern. The diffraction patterns combined with the direct images of a specimen allow us to characterize the crystal structure in a much-detailed manner.

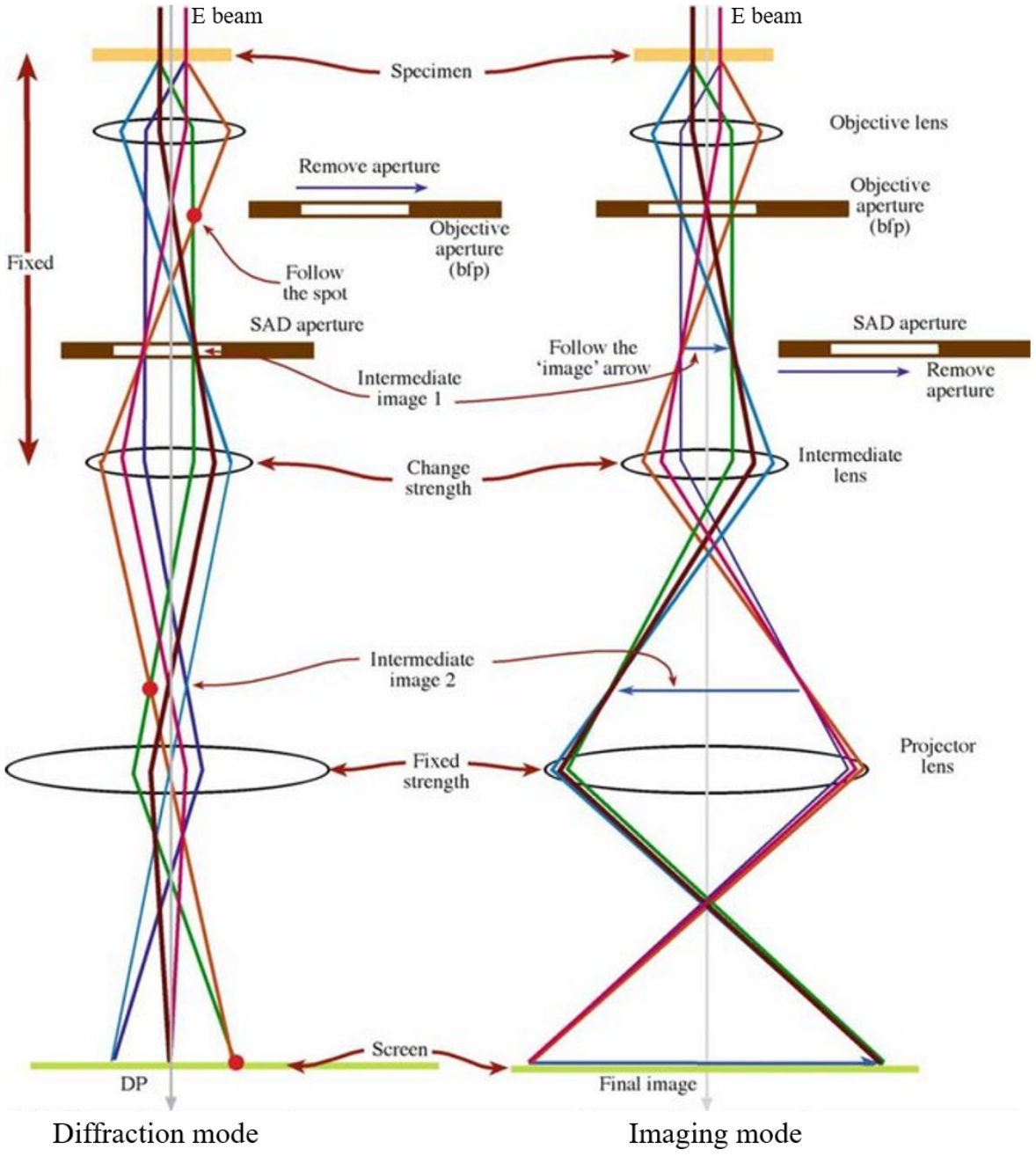

Figure 2.7. The two basic modes of TEM: diffraction mode and imaging mode. Figure adapted from [64].

While it offers a high-resolution view of a sample, there are some shortcomings in TEM. One such shortcoming is the sampling problem, i.e. only a small portion of the sample can be viewed at a time in a TEM. So, this technique must be coupled with techniques with larger sampling size, such as SEM. Sample preparation is another limitation of TEM. Since it relies on the electrons that travel through the specimen, they have to be thin enough to be electron transparent so that a reasonable number of transmitted electrons can be detected. The thickness of the specimen depends on the energy of the electrons and the atomic number of the elements in the specimen [64]. For a typical 100 keV electron beam, a iron sample would have to be some hundred nm thick, whereas a lighter metal like aluminum could be about 1 μm thick to be electron transparent [64]. Therefore, the samples should be made as thin as possible ($<$ 100 nm), especially if the goal is to obtain high resolution TEM images to resolve atomic structures [64].

In this work, TEM was performed at Brookhaven National Laboratory. TEM samples were prepared using Focused Ion Beam (FIB) with Ga^+ ions that were further milled using Nanomill with Ar^+ ions to remove the surface damage. The TEM and Electron Energy Loss Spectroscopy (EELS) experiments were performed using the 200 keV JEOL ARM electron microscope equipped with double aberration correctors, a dual-energy-loss spectrometer, and a cold field emission source. The atomic resolved STEM images were collected with condenser aperture (30 μm) of 21 mrad and collection angle of 67 - 275 mrad for HAADF and 11 - 23 mrad for ABF images. The STEM imaging conditions were optimized for EELS spectroscopy with a probe size of 0.8 Å, a convergence semi-angle of 20 mrad, and the collection semi-angle of 88 mrad. The fine structure of the EELS spectrum (Fe/Ni-L and O-K edge) was obtained with an energy resolution of about 0.8 eV with energy dispersion of 0.25 eV. Dual EELS mode was used to remove the intrinsic energy shifts of the electron beam introduced in the EELS scanning process. The EELS spectra were background subtracted with a power-law function, and multiple scattering was removed by a Fourier deconvolution method.

2.4.2 Magnetic force microscopy

Magnetic Force Microscopy (MFM) is a special mode of operation of the non-contact scanning force microscope (SFM) which allows the detection of magnetostatic interactions at a local scale by using a ferromagnetic probe [67]. Therefore, it is an important analytical tool whenever the near-surface stray-field variation of a magnetic sample is of interest [67], and has been extensively used in both scientific research and industrial applications. For example, MFM can be used to map magnetic domains and interdomain boundaries at high-spatial resolution. It has also been used to image magnetic vortices in superconductors.

An SFM consists of a cantilever, which is brought close and held at a fixed distance from a sample surface to measure long-range forces exerted on it by the sample. In the simplest terms, an SFM obtains the information about a sample's surface by mapping the sample-cantilever interaction forces. To improve the sensitivity of measurements, a dynamic approach is employed where an oscillating cantilever is brought close to the sample and the changes in its oscillation is measured as the cantilever interacts with the sample. Each cantilever can be described by its resonant frequency given by its stiffness c and mass m, i.e. $\omega_0 = \sqrt{c/m}$. When the cantilever is excited sinusoidally at its clamped end with a driving frequency ω and an amplitude d_0, the tip oscillates sinusoidally with a certain amplitude δ, but with a phase shift α with respect to the driving signal. The phase difference between the driving signal and the oscillation of the probe tip can be monitored optically using laser interferometer to monitor the motion of the probe tip.

The equation of motion that describes the output from the cantilever sensor can be written as [67]

$$\frac{\partial^2 d}{\partial t^2} + \frac{\omega_0}{Q}\frac{\partial d}{\partial t} + \omega_0^2(d - d_0) = \delta_0\omega_0 \cos(\omega t), \tag{2.7}$$

where $d(t)$ is the instantaneous probe-sample separation and d_0 is the distance between the probe and the sample at zero oscillation amplitude. Q is the so-called Q-factor of the cantilever, which is determined by the damping factor γ, $Q = m\omega_0/2\gamma$. The above equation

is the equation of motion of a damped driven harmonic oscillator, the steady-state solution to which is

$$d(t) = d_0 + \delta \cos(\omega t + \alpha), \tag{2.8}$$

with its oscillation amplitude and phase shift given by

$$\delta = \frac{\delta_0 \omega_0^2}{\sqrt{(\omega^2 - \omega_0^2)^2 + 4\gamma^2\omega^2}} \tag{2.9}$$

and

$$\alpha = \arctan \frac{2\gamma\omega}{\omega^2 - \omega_0^2}, \tag{2.10}$$

respectively. When the probe is brought sufficiently close to the sample, the tip-sample interaction force F affects the motion of the cantilever and its equation of motion will be modified to include a term F/m. Although F could be a function of both d and $\partial d/\partial t$, in the first order approximation for $\delta_0 << d_0$, one can simply take $F = F(d)$ [67]. In this approximation, the force microscope detects the vertical component of the force gradient $\partial F/\partial z$. The modified spring constant of the cantilever under the influence of $F(d)$ can be written as $c_F = c - \partial F/\partial z$. If the tip-sample interaction is attractive, the cantilever spring is softened, whereas if the interaction is repulsive, the spring is stiffened. This change in spring constant of the cantilever also changes its resonant frequency as

$$\omega = \omega_0 \sqrt{1 - \frac{1}{c}\frac{\partial F}{\partial z}}, \tag{2.11}$$

with a shift in the resonance frequency given by

$$\Delta\omega \simeq -\frac{1}{2c}\frac{\partial F}{\partial z}. \tag{2.12}$$

Thus, the lateral variation of $\partial F/\partial z$ can be obtained by mapping out the experimentally measurable quantities $\Delta\omega$, δ, and α.

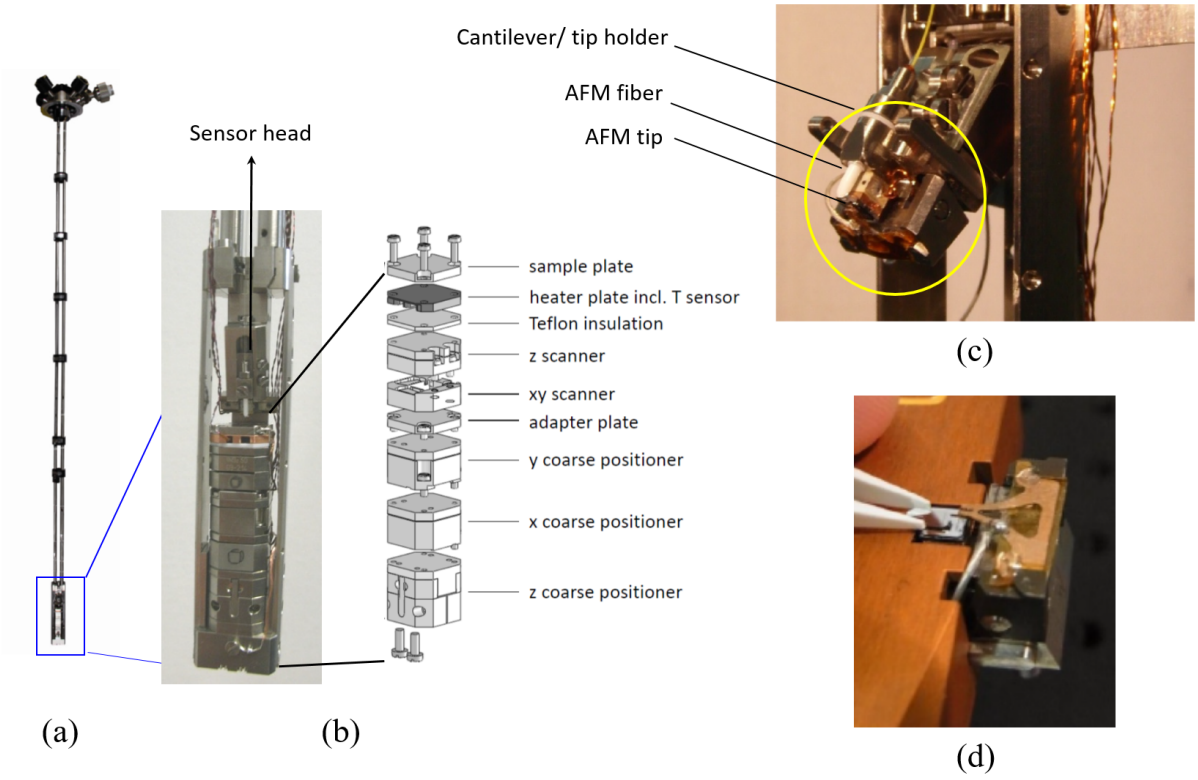

Figure 2.8. Instrumentation for MFM imaging. (a) Atomic Force Moicroscopy insert for PPMS with attoAFM/MFM Ixs head from Attocube Systems AG. (b) Enlarged picture of the probe head with a blow-up of constituent parts. (c) Enlarge picture of the sensor head. (d) A MFM cantilever being inserted into the clamping mechanism of the tip holder. Figures adapted from [68].

In this work, we use a MFM measurement system made by Attocube Systems AG [68]. The system, pictured in Figure 2.8(a), consists of an insert, which is roughly the length of the sample space of PPMS. When inserted into the PPMS, the bottom end of the insert, where the MFM probe head is located, sits roughly at the location where the magnetic field is constant. The blown-up images of the probe head are shown in Figure 2.8(b). It consists of a piezo stack and the sensor head. The piezo stack includes three coarse piezo positioners (x, y, and z) and two scanners (xy and z). The sample plate is attached on the top of the piezo stack with a teflon insulating plate separating it from the z scanner. An optional heater plate with a temperature sensor can be inserted under the sample plate. The sensor head, which houses the tip holder and AFM fiber, lies directly above the sample

plate and has a hinging mechanism for easy access to the fiber and the tip holder, as shown in Figure 2.8(c). The tip holder is easily removed from the sensor to replace the tips. As shown in Figure 2.8(d), the tip holder has a clamping mechanism that keeps the tip in place without the need to use any adhesive.

MFM samples are prepared by cutting single crystals into flat disks of ∼5 mm diameter and mechanically polishing the surface to a sub-micron roughness. The sample is mounted on the sample holder using vacuum grease, and silver paint is used to ground the sample. All MFM imaging is done in the dual pass mode to get rid of the surface topography contribution. As depicted in Figure 2.9, in the first pass, an AFM topography scan is done in tapping mode with the tip close to the sample surface. In the second pass, the tip is lifted by a lift height h and a second scan is done following the topography profile. This way, the signal from the second pass scan contains just the magnetic information. Prior to MFM imaging the samples, a piece of zip disk is imaged to check the tip quality and to optimize the signal to noise ratio. Representative AFM/MFM images obtained from a zip disk are displayed in Figure 2.10. The MFM image consists of a periodically arranged regions of "up" and "down" magnetization, representing the individual bits.

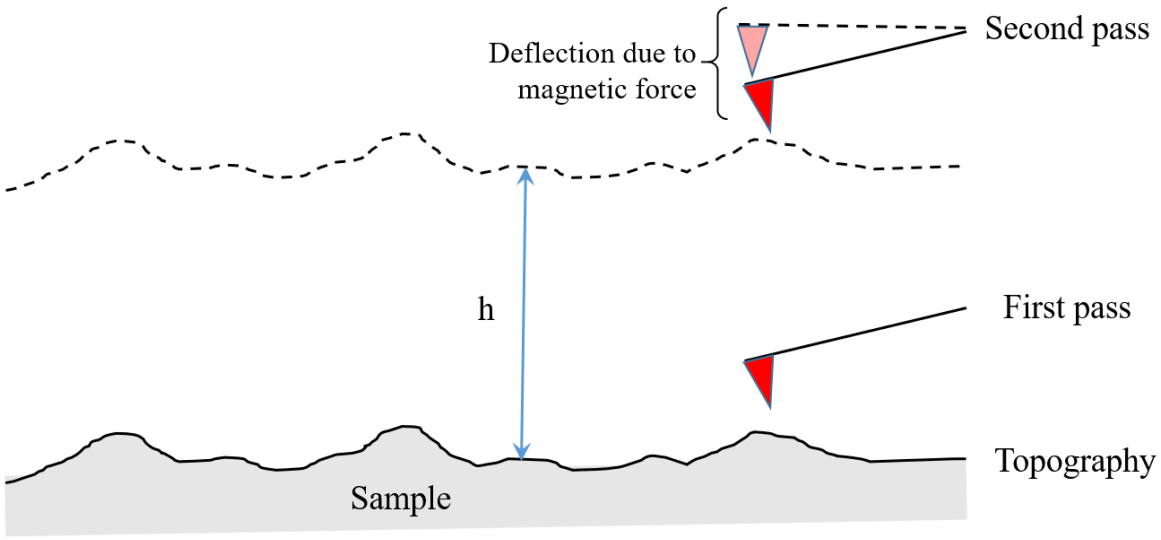

Figure 2.9. A schematic of the dual pass mode of magnetic force microscopy scan.

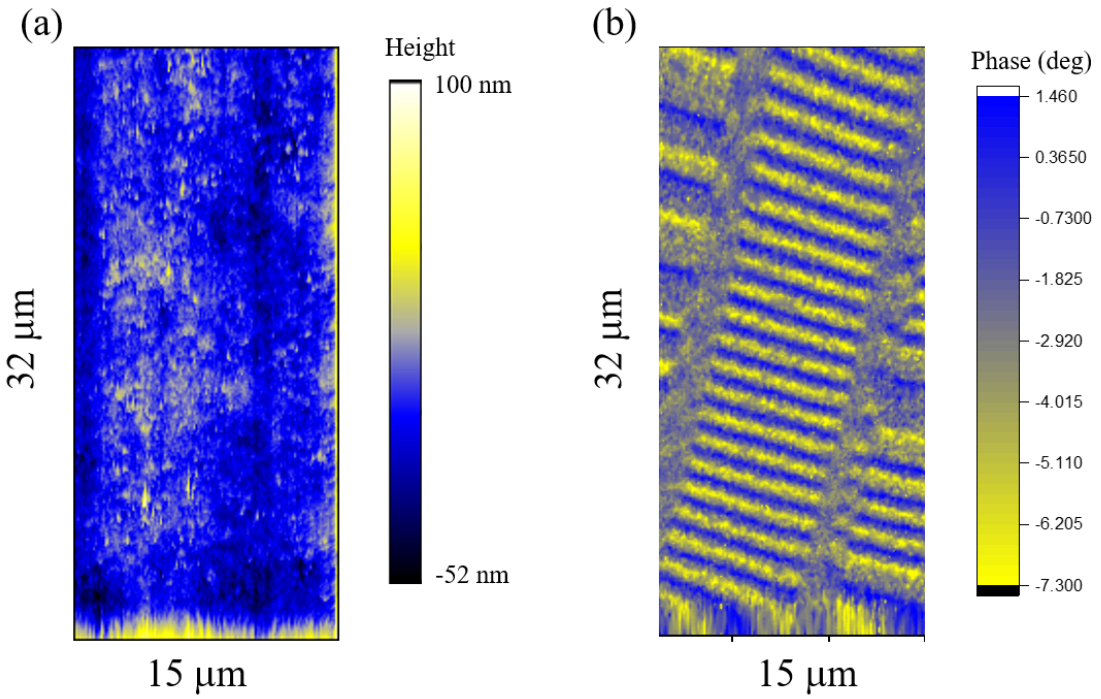

Figure 2.10. (a) AFM and (b) MFM images obtained from a piece of zip disk.

Chapter 3
Structural and Magnetic Transitions in Spinel $FeMn_2O_4$ Single Crystals

3.1 Motivation

As described in Chapter 1, substitution of iron from one or more sublattice sites by another magnetic ion in spinel ferrites allows us to study the competition between various magnetic interactions and resulting magnetic frustration. Such a substitution can lead to dramatic changes to the magnetic landscape and new magnetic ground states can emerge. Manganese ferrites ($Mn_xFe_{3-x}O_4$) are one such group of compounds where the Fe ions are replaced by Mn ions. Since both Fe and Mn can have multiple oxidation states, the cationic distribution can be quite complex. Based on their octahedral site preference energies, presented in Table 1.2, Mn^{2+} and Fe^{3+} cations prefer the T-sites, and Mn^{3+} and Fe^{2+} prefer the O-sites. This leads to the presence of multiple magnetic ions in both T-and O-sites, resulting in multiple competing exchange interactions [69–71]. Additionally, due to the presence of J-T active Mn ions in them, their structures depend on the amount of manganese present in them. At room temperature, they crystallize in a cubic structure for $x < 2$, but are tetragonally distorted for $x \geq 2$ due to a cooperative J-T distortion of the MnO_6 octahedra [70–72]. Magnetically, due to the presence of magnetic ions in both sublattices, this system orders in a FI configuration at high temperature, with T_{FI} decreasing with increasing x. However, most of these studies have been performed on the iron-rich region, i.e. $x < 1$, and there have only been a few reports on the manganese-rich compounds [73–76].

$FeMn_2O_4$ ($x = 2$) is an interesting member of this family. It has a reported cation distribution of $(Mn0.9^{2+}Fe^{3+}_{0\,1})_T(Mn1.1^{3+}Fe^{3+}_{0\,9})_OO_4$ [78]. Among the three types of cations that are present, the Fe^{3+} and Mn^{2+} have five 3d electrons in their outer shell, making them

A major portion of the work presented in this chapter was previously published as Roshan Nepal, Qiang Zhang, Samuel Dai, Wei Tian, S. E. Nagler, and Rongying Jin, *Physical Review B* **97**, 024410 (2018) [77]. Please refer to the Appendix for the permission from American Physical Society.

orbitally inactive. On the other hand, the Mn^{3+} ions residing in the O-sites have orbital degree of freedom. Their cooperative J-T distortions causes $FeMn_2O_4$ to crystallize in a tetragonal structure at room temperature. $FeMn_2O_4$ is reported to have a ferrimagnetic transition at ∼381 K [69]. In addition, there is a report that claims that the magnetic structure at 5 K is different from that at higher temperatures with canted spins at O-sites [73]. The origin of this low temperature spin arrangement is not clear, and the effects of these magnetic transitions on other overall physical properties are not fully explored. In this work, we present the structural, magnetic, and thermal properties of $FeMn_2O_4$ single crystals. We identified one structural and two magnetic transitions from magnetization and neutron diffraction measurements. Additionally, we found that the magnetic excitations have significant impacts on low temperature thermal properties, including thermal conductivity and specific heat.

3.2 Results and discussion

Single-crystalline $FeMn_2O_4$ was grown using floating zone furnace, as described in Chapter 2. For the growth, we first synthesized polycrystalline $FeMn_2O_4$ via the solid-state reaction of the mixture of Fe_2O_3 and Mn_2O_3 with a 1 : 2 molar ratio. The ground mixture was heated at 1250°C for 12 hours and quenched in liquid nitrogen in order to obtain the spinel structure. The quenched sample was reground and annealed in air at 200°C for five days to get rid of the high-temperature cubic phase. The polycrystalline sample was then hydrostatically pressed into rods and further sintered at 1250°C for 12 hours. The growth rate of 3 mm/h was used while the top and bottom rods were rotated in opposite directions at 30 rpm to minimize inhomogeneity.

A typical single-crystal boule obtained from the floating zone furnace is shown in the inset of Figure 3.1(b). The room-temperature x-ray diffraction data obtained from powder made by crushing single crystals is shown in the main panel of Figure 3.1(b). All peaks could be indexed under a tetragonal crystal structure ($I4_1/amd$, No. 141) with $a = b = 5.91$ Å and $c = 8.91$ Å ($a' = \sqrt{a} = 8.36$ Å and $c' = c = 8.91$ Å in pseudocubic notation [79], with

$c'/a' = 1.07$), indicating a single phase. These values are comparable with the previous reports [73, 76]. Interestingly, neutron diffraction indicates that the single crystal grows along the $(111)_c$ direction, as illustrated in the inset of Figure 3.1(b). This suggests that the chemical bond is the strongest along the $(111)_c$ direction. From the EDS measurements, we found that the actual Fe:Mn ratio was indeed 1:2 in our single crystal, indicating the correct spinel phase.

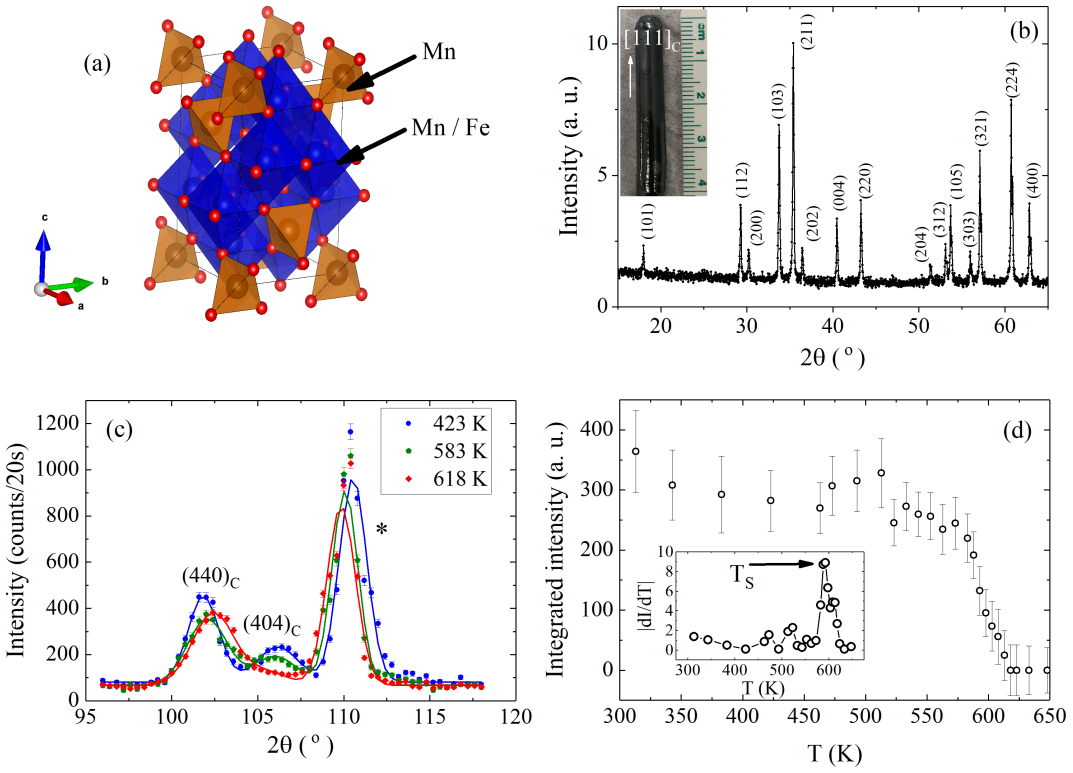

Figure 3.1. Structural properties of $FeMn_2O_4$. (a) Crystal structure of $FeMn_2O_4$. (b) Room temperature powder x-ray diffraction pattern with all peaks indexed in the $I4_1/amd$ tetragonal symmetry. Inset: An as-grown single crystal with the growth direction indicated by an arrow; (c) $(440)_c$ and $(404)_c$ nuclear peaks indexed in pseudocubic notation at indicated temperatures via neutron powder diffraction measurements. The peak indicated by * is the aluminum (220) peak from the Al sample holder. (d) Temperature dependence of the integrated intensity of $(404)_c$ nuclear peak. Inset: The derivative of the $(404)_c$ peak intensity for T_s determination.

Our neutron powder diffraction measurement confirmed the tetragonal (pseudocubic) structure at room temperature. Figure 3.1(c) shows the neutron diffraction pattern in

the range of $96^0 < 2\theta < 118^0$ at three different temperatures. The peaks are labeled in pseudocubic notation, and the peak at $2\theta \sim 111^o$ can be indexed as aluminum (220) reflection from the aluminum sample holder. It can be seen that at 423 K (blue points), both $(440)_c$ and $(404)_c$ peaks are present and well separated. At 583 K (green points), the two peaks have slightly lower intensity and move towards each other. At a higher temperature of 618 K (red points), the two peaks merge together into a single peak, indicating a structural transition between 583 K and 618 K in $FeMn_2O_4$. The absence of the $(404)_c$ peak at 618 K demonstrates that the structure becomes cubic at higher temperatures. In order to accurately determine the transition temperature, we traced the $(404)_c$ peak intensity as a function of temperature, which is shown in Figure 3.1(d). It is clear that the $(404)_c$ peak becomes detectable below 618 K. Furthermore, its intensity increases and tends to saturate below 550 K, suggesting a transition window of about $\Delta T_s \sim 618 - 550 = 68$ K. We thus determine the transition temperature $T_s \sim 595$ K, corresponding to the peak position in the derivative of peak intensity with respect to the temperature (inset of Figure 3.1(d)). This transition temperature is much higher than that obtained from thermal expansion measurement [75]. However, it was also reported that the structural transition occurs near 623 K for $Fe_{0.9}Mn_{2.1}O_4$ ($x = 2.1$) [75]. This suggests that the structural transition is intimately connected to Mn concentration and distribution as discussed previously [41].

The temperature dependence of magnetization $M(T)$ of $FeMn_2O_4$ is shown in Figure 3.2(a). The data was collected between 2 and 800 K with an external field of 0.1 T applied along the $(111)_c$ direction. The black open circles represent the zero-field-cooling (ZFC) and field-cooling (FC) magnetization data obtained from SQUID, while the red circles represent the data from VSM magnetometer. A good agreement can be seen between the two sets of data in the overlapping region between 300 and 400 K. Interestingly, there is no anomaly near the structure transition region (see the inset of Figure 3.2(a)). Instead, a sharp increment in magnetization is seen below ∼400 K followed by an obvious decrease below ∼50 K, indicating two magnetic transitions. Two peaks are observed in the plot of

dM/dT (Figure 3.2(b)) that can be used to estimate the transition temperatures to be T_{FI-1} $\sim$ 373 K and T_{FI-2} $\sim$ 50 K, which are comparable to those previously reported [69, 73]. In a previous neutron diffraction study, the authors reported an occurrence of a ferrimagnetic ordering below 390 K, which was followed by sublattice spin reorientations below 55 K, resulting in a noncollinear ferrimagnetic ordering [73]. The downturn in both ZFC and FC M(T) curves below T_{FI-2} indicates the reduced net magnetic moment, consistent with the noncollinear behavior. Applying magnetic field perpendicular to the $(111)_c$ direction yields similar behavior, with a small difference in saturation moment, as shown in the inset of Figure 3.2(b). This indicates that the magnetic easy axis is also along the $(111)_c$ direction.

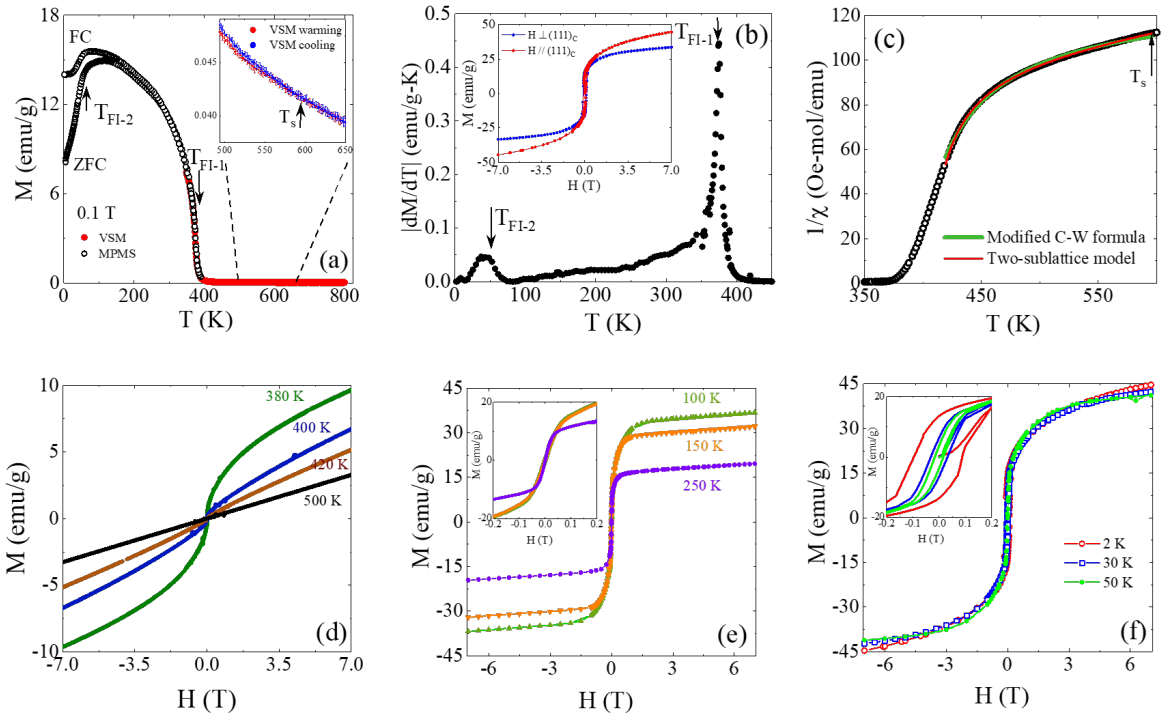

Figure 3.2. Magnetic properties of $FeMn_2O_4$. (a) Temperature dependence of magnetization in $FeMn_2O_4$ under H = 0.1 T. Inset: zoomed-in view of M near T_s. (b) First derivative of magnetization with respect to temperature for the determination of T_{FI-1} and T_{FI-2}. Inset: field dependence of magnetization with magnetic field parallel (red) and perpendicular (blue) to $(111)_c$. (c) Inverse susceptibility as a function of temperature in the paramagnetic region. (d-f) Isothermal magnetization hysteresis loops at indicated temperatures with T $>$ T_{FI-1}, T_{FI-1} $>$ T $>$ T_{FI-2}, and T $<$ T_{FI-2}, respectively. Insets of (e and f): zoomed-in view of M(H) from -0.2 to 0.2 T.

To further understand the nature of these magnetization anomalies, we analyzed the high-temperature inverse susceptibility $\chi = M/H$ using a modified Curie-Weiss formula

$$\chi = \chi_0 + \frac{C}{T - \theta}. \tag{3.1}$$

Here, χ_0 describes the temperature-independent contribution, θ is the Curie-Weiss temperature, and C is the Curie constant. By fitting our paramagnetic susceptibility data up to T_s to Eq. (3.1), we obtained $\chi_0 = 0.00776$ emu/mol, $C = 0.259$ emu-K/mol, and $\theta = 393$ K. Figure 3.2(c) displays $1/\chi$ as a function of temperature between 350 and 600 K and the fitting curve (green). While Eq. (3.1) fits our data reasonably well between 450 and 600 K and the value of θ is close to $T_{FI\text{-}1}$, χ_0 is high, and C is considerably small. In view of the field dependence of magnetization at high temperatures, as shown in Figure 3.2(d), it is simply linear behavior above 420 K. This indicates that large χ_0 is unlikely due to a ferromagnetic-like impurity. On the other hand, from $C = N_A \mu_{eff}^2 / 3k_B$ (N_A is the Avogadro constant and k_B is the Boltzmann constant), we obtained the effective magnetic moment $\sim 1.44\mu_B$/formula unit. According to Ref. [73], the magnetic moment is $\sim 4.3\mu_B$ for the T-sublattice and $\sim 3.1\mu_B$ for the O-sublattice. This indicates that the ferrimagnetic interaction in $FeMn_2O_4$ cannot be described by the simple Curie-Weiss law. According to the molecular field theory of ferrimagnetism described in Section 1.2, the susceptibility above the transition temperature is better characterized by the Néel's expression

$$\frac{1}{\chi} = \frac{T - \theta_a}{C'} - \frac{\xi}{T - \theta'}. \tag{3.2}$$

Here, the first term describes the high-T asymptotic behavior, and the second term describes the hyperbolic behavior near the ferrimagnetic transition. The red curve in Figure 3.2(c) represents the results from the fit of Eq. (3.2) to the experimental data between 420 and 595 K with $\theta_a = -824$K, $C' = 11.91$ emu-K/mol, $\theta' = 389.9$K, and $\xi = 1495$ mol-K/emu.

As described in Section 1.2, θ_a, C', θ', and ξ are parameters derived from the two-sublattice model of ferrimagnetism. The parameter θ_a, known as the asymptotic Curie temperature, measures the strength of antiferromagnetic coupling of spins between the two sublattices [47, 80]. The large value of θ_a, with the ratio $|\theta_a|/\mathrm{T_{FI\text{-}1}} \sim 2.2 > 1$, suggests an appreciable frustration in the system [1]. The characteristic temperature θ' should be close to the ferrimagnetic transition temperature [81], which is seen in our case. The parameter C' is the sum of the sublattice Curie constants, i.e. $C' = C_T + C_O$ [7, 40, 71], which allows us to estimate the effective magnetic moment $\sim 9.76\mu_B$ per formula. Assuming the cation distribution is $(\mathrm{Mn^{2+}})_T\ [\mathrm{Fe^{3+}Mn^{3+}}]_O\mathrm{O_4}$, we can calculate the theoretical magnetic moment using $5.9\mu_B/Mn^{2+}$ ($S = 5/2$: the high-spin state) in the tetrahedral environment, and $\sim 4.9\mu_B/Mn^{3+}$ ($S = 2$: the high-spin state) and $5.9\mu_B/Fe^{3+}$ ($S = 5/2$: the high-spin state) in the octahedral environments [7]. Using $\mu_{eff}^2 = \mu_O^2 + \mu_T^2$ [7, 80, 82] the theoretical effective moment is calculated to be $\mu_{eff} \sim 9.68\mu_B$, close to our experimental value. If it is distributed as $(\mathrm{Mn^{2+}_{0.9}Fe^{3+}_{0.1}})_\mathrm{T}(\mathrm{Fe^{3+}_{0.8}Fe^{2+}_{0.1}Mn^{3+}_{1.1}})_\mathrm{O}\mathrm{O_4}$ as concluded previously by Refs. [73, 78, 83], the calculated value should be even larger, i.e. closer to our experimental value. This suggests that the Mn and Fe ions are in their high-spin states.

To further confirm the ferrimagnetic nature below $\mathrm{T_{FI\text{-}1}}$, we measured the isothermal field dependence of magnetization in $\mathrm{FeMn_2O_4}$, which is presented in Figure 3.2(d). At temperatures greater than $\mathrm{T_{FI\text{-}1}}$, a linear dependence of $M(H)$ is observed, confirming a paramagnetic order. At 400 K, a non-linear dependence is observed at low fields, indicating the emergence of a magnetically ordered state. The non-linear $M(H)$ curves become more profound upon further cooling the sample. At the same time, we also notice the emergence of a hysteresis loop centered at the origin. With the decreasing temperature, the saturation magnetization and coercive field increase. These observations and the negative value of θ_a confirm that the magnetic ordering that emerges below $\mathrm{T_{FI\text{-}1}}$ is ferrimagnetic. This result is in accord with a previous neutron diffraction study [73].

At $T_{FI\text{-}2} < T < T_{FI\text{-}1}$, the magnetization reaches saturation easily, as seen in Figure 3.2(e), suggesting soft ferrimagnetic nature. Below $T_{FI\text{-}2}$, the behavior of $M(H)$ differs from that at high temperatures. As shown in Figure 3.2(f), M continuously increases with increasing H without saturation up to 7 T down to 2 K. This implies that the ordering below $T_{FI\text{-}2}$ is more difficult than that above $T_{FI\text{-}2}$. Such a low temperature transition usually arises due to the canting of O-site spins, a manifestation of geometric frustration, which has been reported in spinel systems with magnetic ions in both T- and O-sites [43, 46]. Due to the presence of magnetic ions in both the T- and O-sites in $FeMn_2O_4$, the transition at $T_{FI\text{-}2}$ is likely to have the same origin. As highlighted in the inset of Figure 3.2(f), the noncollinear magnetic alignment results in a larger hysteresis loop than that in the collinear situation at high temperatures. With decreasing temperature, the decrease of magnetic susceptibility (Figure 3.2(a)) and the enhanced coercive field seen in hysteresis loops (Figure 3.2(f)) indicate the noncollinear magnetic ground state.

To resolve the exact nature of the magnetic ordering in the two regions, we performed further neutron diffraction experiments. In order to obtain an accurate spin arrangement information in the magnetic regions, we first refined the structure to determine the cation distribution across the sublattices. From refinement of the NPD data obtained above $T_{FI\text{-}1}$, we determined the cation distribution to be $(Mn^{2+}_{0.904}Fe^{3+}_{0.096})_T(Mn^{3+}Fe^{3+}_{0.904}Mn^{2+}_{0.096})_OO_4$. The T-sites are occupied mostly by Mn^{2+} ions and the O-sites have a mixed occupation of Mn and Fe ions. With the structure and cation distribution obtained, we carried out similar refinement of the NPD data in the two magnetically ordered regions. Figure 3.3(a) shows the refinement result of NPD data obtained at 300 K, i.e. in the FI-1 ordered region. The spin arrangement obtained from the refinement is displayed in Figure 3.3(b). At 300 K, the spin arrangement is collinear, i.e. the spins at the T-sites are ordered antiparallel to those at the O-sites. The average magnetic moment at the T-site was found to be 3.485 μ_B and that at the O-site was found to be -1.386 μ_B, resulting in a net moment of $\sim$0.713 μ_B per formula unit.

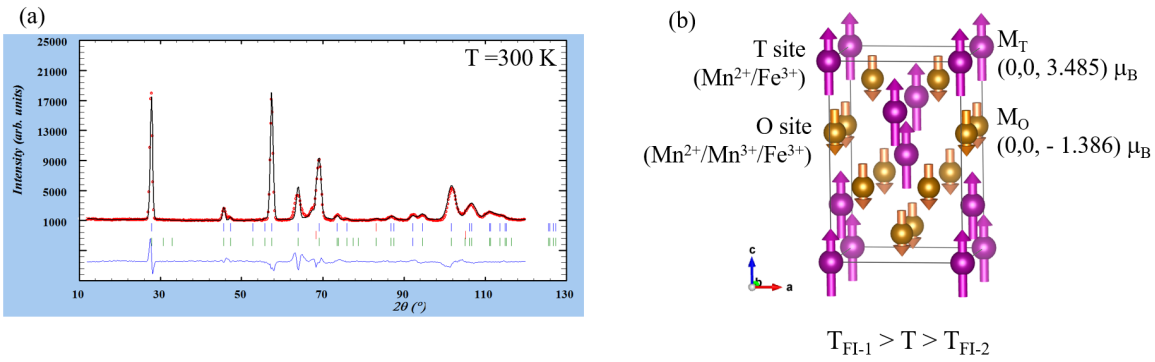

Figure 3.3. (a) Neutron powder diffraction pattern obtained at 300 K. (b) Spin arrangement in $T_{FI\text{-}1} > T > T_{FI\text{-}2}$ region.

In contrast, the spin arrangement below $T_{FI\text{-}2}$ is much more complex. Figure 3.4 shows the NPD data obtained at 5 K and the corresponding spin arrangement obtained from the refinement. Here, the O-site spins are canted to those at T-sites by approximately 28°. The average T-site moment is 4.95 μ_B along c axis, whereas the O-site moment is (±1.08, 0, -2) μ_B or (0, ±1.08, -2) μ_B. This results in a net moment of ~0.95 μ_B along c axis. In this arrangement, the pyrochlore O-sublattice follows the so-called ice rules and orders in two-in-two-out arrangement, i.e spin ice arrangement, as shown in Figure 3.4(c).

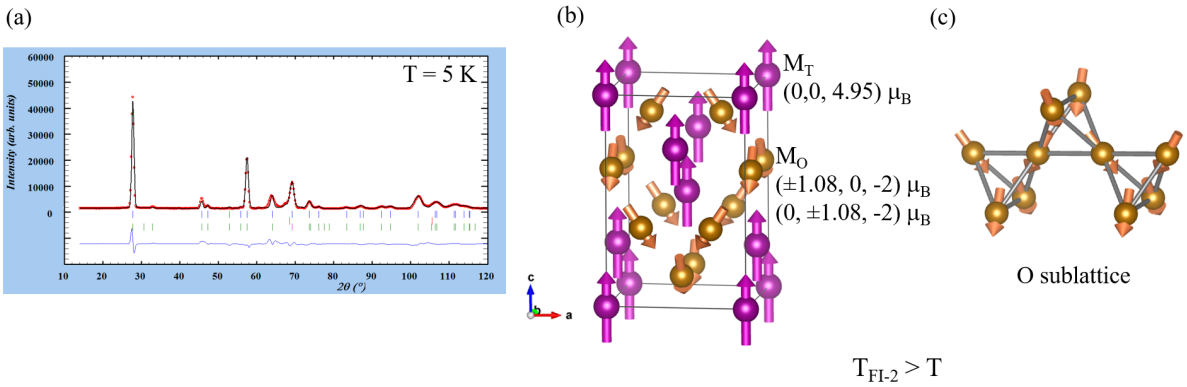

Figure 3.4. (a) Neutron powder diffraction pattern obtained at 5 K. (b) Spin arrangement in $T_{FI\text{-}2} > T$ region (c) The two-in-two-out spin arrangement in the O-sublattice.

Magnetic ordering usually involves entropy change, thus resulting in specific heat anomaly. The temperature dependence of the specific heat C_p of $FeMn_2O_4$ between 2 K and 400 K is shown in Figure 3.5(a). There is clearly a peak at $T_{FI\text{-}1}$, indicating a true

phase transition. The small peak suggests that most entropy is removed prior to ordering. Even though there is a sharp decrease in magnetization due to spin canting transition, there is no sign in specific heat at $T_{FI\text{-}2}$, while it tends to vary slower at low temperatures as seen in dC_p/dT [see the inset of Figure 3.5(a)]. Nevertheless, we find the low-temperature specific heat can be described by the following equation:

$$C_p(T) = \beta T^3 + \delta T^{3/2} e^{-\Delta_m/T}. \tag{3.3}$$

Here, the first term is the low temperature approximation of the Debye phonon specific heat with $\beta = (12\pi^4/5) n N_A k_B/\theta_D^3$, where θ_D is the characteristic Debye temperature and n is the number of atoms in the formula unit ($n = 7$ for spinel oxides). The second term is the magnetic contribution to the specific heat in a ferri- or ferromagnetic system [84–86], with δ, a spin-wave stiffness related constant, and Δ_m, the anisotropy related spin-wave gap. As shown in Figure 3.5(b), the behavior of specific heat below 10 K is well described by Eq. (3.3) with the fitting parameters $\beta = 2.2{\cdot}10^{-4}$ J/mol K^4, $\delta = 0.033$ J/mol K$^{5/2}$, and $\Delta_m = 1.03$ K. From the fitted value of β, we can estimate the Debye temperature $\theta_D \sim 395$ K, which is comparable to the previous reports on other manganese ferrites [87]. For comparison, we plot the magnetic contribution (C_{mag}) and the phonon contribution (C_{ph}) in Figure 3.5(b) as well. Remarkably, the magnetic contribution is much larger than the phonon contribution, indicating that heat is mostly carried by magnetic excitation. Below 10 K, C_{ph} is almost negligible. This is similar to a previous observation in $MnFe_2O_4$ nanoparticles [87].

The small phonon contribution is also reflected in thermal conductivity. Figure 3.5(c) shows the temperature dependence of the thermal conductivity κ. Overall, the temperature profile is prototypical for crystalline materials with a broad peak around 80 K because of umklapp scattering processes at high temperatures. On the other hand, the "tail" above ~250 K is likely due to the thermal radiation at high temperatures. Similar to the

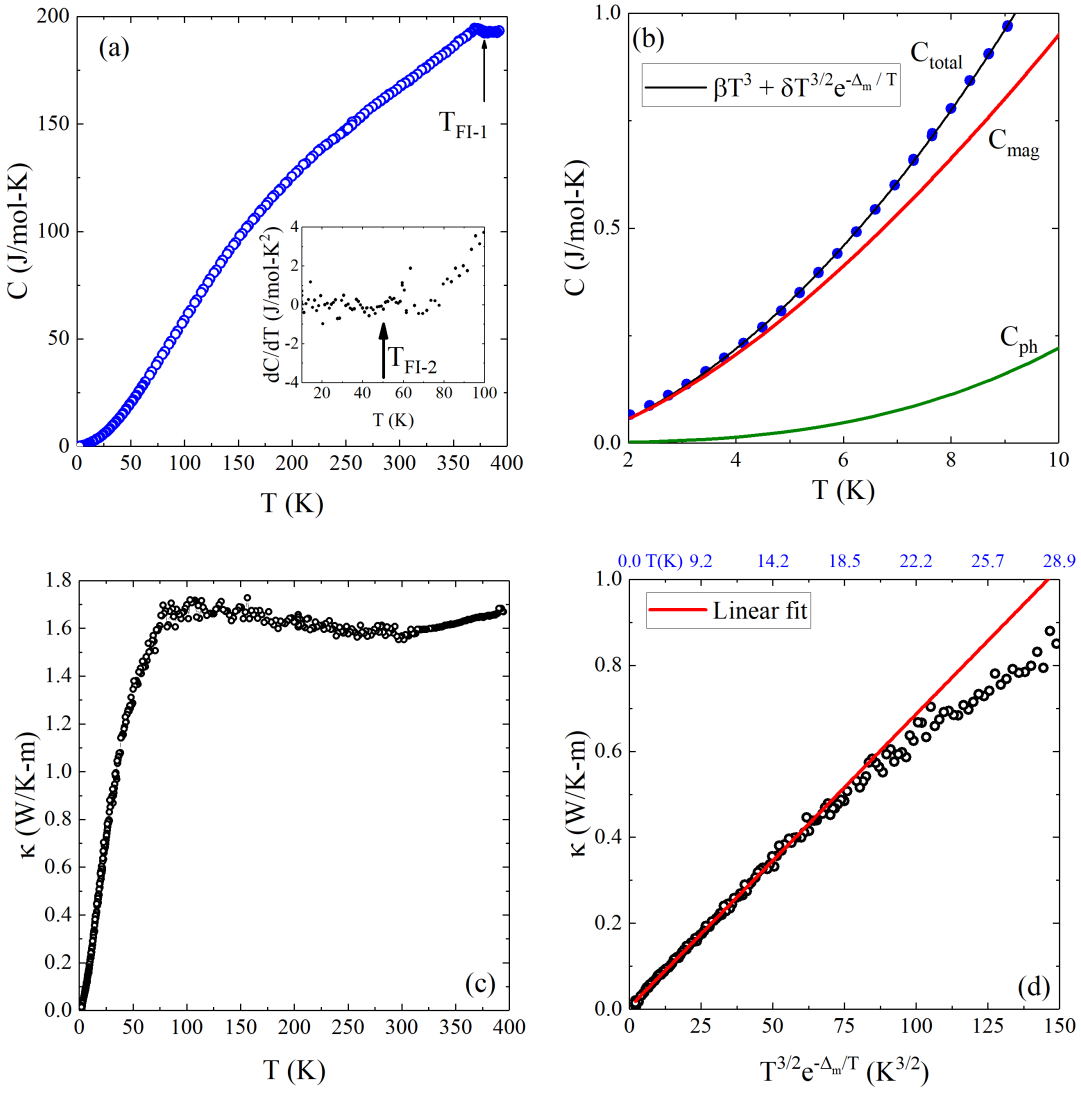

Figure 3.5. Thermal properties of $FeMn_2O_4$. (a) Temperature dependence of specific heat of $FeMn_2O_4$. Inset: Temperature dependece of dC/dT below 100 K. (b) Various contributions to the total specific heat below 10 K. (c) Temperature dependence of thermal conductivity. (d) Low temeprature thermal conductivity as a function of $T^{3/2}e^{-\Delta_m/T}$.

specific heat, no apparent anomaly is observed at $T_{FI\text{-}2}$, suggesting little entropy removal. What is remarkable is the low thermal conductivity in the entire temperature range for a solid, with the maximum ∼1.7 W/K m. There are several possible origins for such a low thermal conductivity: (1) geometric frustration due to the spinel structure as reflected by the high Debye temperature, (2) scattering due to disorder as discussed above with

both manganese and iron partially occupying the T- and O-sites, and (3) magnon-phonon scattering processes [88, 89].

We now focus on the low-temperature behavior of κ. Being an electrical insulator, the thermal conductivity κ of $FeMn_2O_4$ can be written as a sum of phonon contribution κ_{ph} and magnetic contribution κ_{mag}, both solely depending on the respective specific heat at low temperatures. Given that Eq. (3.3) describes our low-temperature specific heat, one would expect two contributions to κ as well. Figure 3.5(d) displays $\kappa(T)$ plotted as κ versus $T^{3/2}e^{-\Delta_m/T}$ from 2 to 35 K using the Δ_m value obtained from specific heat. Below 20 K, κ clearly shows a linear dependence to $T^{3/2}e^{-\Delta_m/T}$, as illustrated by the red linear fitting line. This indicates that the low-temperature κ is proportional to C_{mag}, without any sign of the contribution from phonons.

The low thermal conductivity makes crystalline $FeMn_2O_4$ promising for applications, such as thermoelectrics. The temperature dependence of the Seebeck coefficient (S) of $FeMn_2O_4$ is shown in Figure 3.6(a). While it is negligible at temperatures below 250 K, the magnitude of negative thermopower increases with increasing temperature, reaching the maximum at the onset of ferrimagnetic transition. The negative thermopower indicates that heat is mainly carried via electrons (n type). The downturn of S at T_{FI-1} indicates the effect of magnetic transition, which likely changes the electronic structure [90].

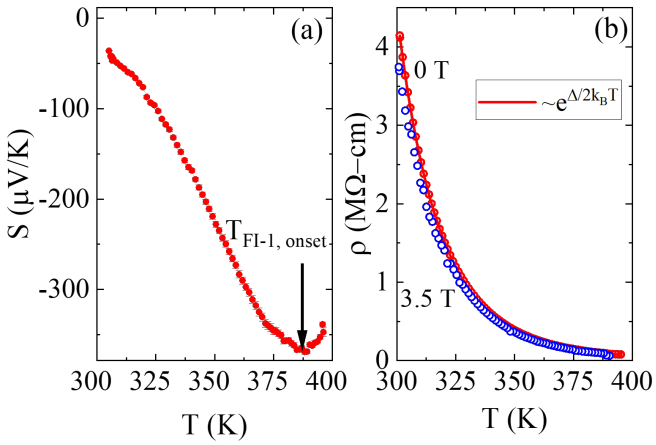

Figure 3.6. (a) Temperature dependence of the Seebeck coefficient where T_{FI-1} onset is indicated. (b) Electrical resistivity (ρ) as a function of temeprature at H = 0 and 3.5 T.

Large thermopower and small thermal conductivity are desired properties for thermoelectrics. Unfortunately, the electrical resistivity (ρ) of $FeMn_2O_4$ is too high, and it only becomes measurable above room temperature. Figure 3.6(b) shows the temperature dependence of ρ between 300 and 400 K, which decreases exponentially with increasing temperature. With the application of a magnetic field, a negative magnetoresistance is seen, consistent with the ferrimagnetism. The temperature dependence of ρ can be modeled by the Arrhenius equation

$$\rho(T) = \rho(0)e^{-\Delta/2k_{\mathrm{B}}T}, \tag{3.4}$$

where Δ is the activation energy. Our experimental data fit quite well with Eq. (3.4), as shown in Figure 3.6(b). From the fit, we obtain $\Delta \sim 0.88$ eV at zero field.

While the thermoelectric figure of merit $ZT = S^2T/\kappa\rho$ increases with increasing temeprature, it is very low, reaching only $\sim 4 \times 10^{-8}$ at 400 K. As mentioned previously, this is due to a high resistivity. According to the first-principles calculations, $FeMn_2O_4$ is expected to be half-metallic [91]. Whether this is true requires further study, as it related to the degree of inversion in spinel materials [91]. One way to improve the thermoelectric properties of $FeMn_2O_4$ is to introduce chemical doping for suppressing magnetic interaction and increasing the concentration of charge carriers so as to further decrease thermal conductivity and electrical resistivity. Of course, this requires the retention of the spinel structure.

3.3 Conclusion

In summary, we have investigated the structural, magnetic, thermal, and electrical properties of single-crystal $FeMn_2O_4$ in a wide temperature range. As summarized in Figure 3.7, three phase transitions are identified. One is the structural transition at $T_s \sim 595$ K from cubic at high temperatures to tetragonal at low temperatures determined through neutron powder diffraction measurement. The other two are magnetic transitions at $T_{FI\text{-}1}$ ~ 373 K and $T_{FI\text{-}2} \sim 50$ K, respectively. Due to a negative asymptotic Curie temperature extracted above $T_{FI\text{-}1}$ and magnetic hysteresis loops below $T_{FI\text{-}1}$, the transition at $T_{FI\text{-}1}$

is considered as a ferrimagnetic magnetic ordering with anomaly reflected in the magnetization, specific heat, and thermopower. The reduction of the magnetization and wider hysteresis loops indicates the spin rearrangement below $T_{FI\text{-}2}$. The results from magnetization measurements were further confirmed via temperature dependent neutron powder diffraction measurement. The refinement of neutron diffraction patterns revealed that the collinear ferrimagnetic order with antiparallel spins in T- and O-sublattices become non-collinear below $T_{FI\text{-}2}$ with the O-site spins canted by $\sim 28^{o}$ with respect to the T-site spins. Further analysis revealed the two-in-two-out spin configuration in the O-sublattice that obeys the ice rules. Surprisingly, no clear anomaly was observed in either thermal conductivity or specific heat, suggesting little entropy removal for the low-temperature spin configuration. Remarkably, the low-temperature specific heat and thermal conductivity have significant contributions from magnetic excitation, giving rise to $T^{3/2}e^{-\Delta_m/T}$ dependence. This strongly suggests that phonons in this crystalline system conduct little heat, particularly at low temperatures. This characteristic is promising for thermoelectric application. However, much better electrical conduction is required, as it is currently insulating with an energy gap of 0.88 eV.

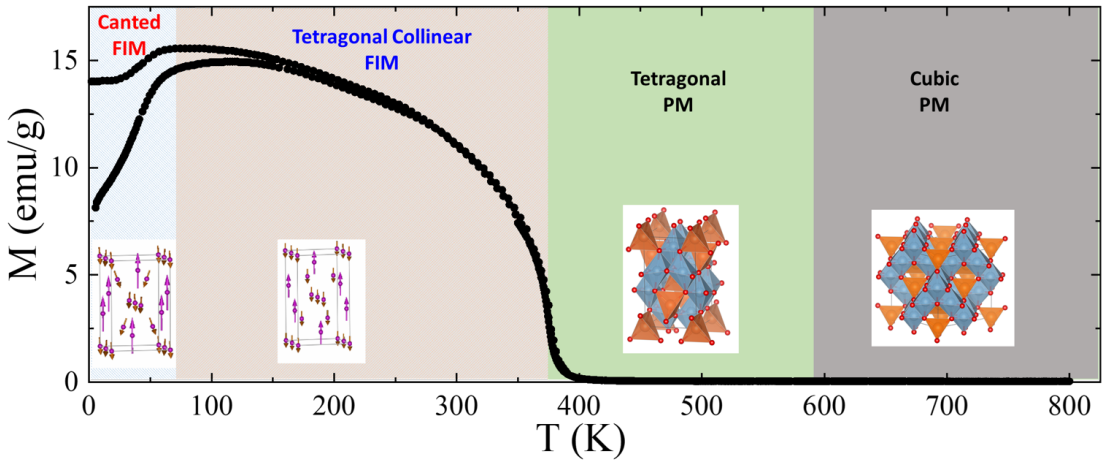

Figure 3.7. A summary of structural and magnetic phase transitions in $FeMn_2O_4$.

Chapter 4
Observation of Three Magnetic States in Spinel $MnFe_2O_4$ Single Crystals

4.1 Motivation

The previous chapter demonstrated the rich phase diagram in a manganese-rich ferrite $FeMn_2O_4$. Here, we explore the magnetic phase diagram of its iron-rich counterpart $MnFe_2O_4$. A well-known room temperature magnetic semiconductor, $MnFe_2O_4$ has been reported to order ferrimagnetically (FI) with a collinear spin arrangement at high temperatures [7, 92, 93]. Despite its well understood high temperature magnetic behavior, there are some discrepancies about its low temperature magnetic order. According to some previous reports, the Mn^{2+} ions at the T-sites are rearranged by $\sim 53^{o}$ canting to the Fe^{3+} ions at the O-sites [94, 95]. In another report, the Mn^{55} nuclear spin-lattice relaxation time revealed anomalies at 3 K and 14 K, both of which were attributed to the existence of Fe^{2+} ions [96]. However, other measurements do not support this picture. Especially, the specific heat [97] and magnetic permeability [98] anomalies that tend to decrease with increasing Fe^{2+} concentration. These inconsistencies are likely a result of the presence of mixed valence manganese and iron cations leading to additional interactions other than the usual O-O, O-T, and T-T interactions that become relevant at low temperatures. A thorough study of $MnFe_2O_4$ is therefore warranted to understand its low-temperature magnetic behavior.

In this work, we have performed a detailed investigation of the structural (via x-ray diffraction), composition (via energy-dispersive x-ray spectroscopy and x-ray photoemission spectroscopy), magnetization, electrical and thermal (electrical resistivity, specific heat, thermal conductivity, and thermopower) properties of $MnFe_2O_4$ single crystals. In addition to the known paramagnetic to ferrimagnetic transition at $T_{FI\text{-}1} \sim 575$ K, two other

The work presented in this chapter was previously published as Roshan Nepal, Mohammad Saghayezhian, Jiandi Zhang, and Rongying Jin, *Journal of Magnetism and Magnetic Materials* **497**, 165955 (2020) [99]. Please refer to the Appendix for the permission from Elsevier.

anomalies are observed at $T_{FI\text{-}2} \sim 50$ K and $T_x \sim 15$ K. The anomaly at $T_{FI\text{-}2}$ has not been previously reported. In addition, we have investigated the magnetic field effect on the low-temperature specific heat and thermal conductivity, which allowed us to elucidate the difference between these two anomalies, even though both have magnetic origins.

4.2 Results and discussion

Single-crystalline $MnFe_2O_4$ was grown via floating zone method, as described in Chapter 2. Similar to the case of $FeMn_2O_4$, here we first synthesized polycrystalline samples via the solid-state reaction between a 1 : 2 molar ratio mixture of Mn_2O_3 and Fe_2O_3. The mixture was heated to 1250°C, kept at that temperature for 12 hours, and cooled to room temperature in 8 hours. The feed and seed rods were prepared from the polycrystalline sample and sintered at 1250°C for 12 hours. The growth rate was set to 3 mm/h, while the feed and seed rods were rotated at 30 rpm in opposite directions. The room temperature x-ray diffraction pattern obtained from a crushed single crystal sample is shown in Figure 4.1(b). All of the observed peaks can be indexed using a cubic crystal structure ($Fd\bar{3}m$, S.G. No. 227) with no detectable impurity phase. From the Rietveld refinement, we obtain the lattice parameter $a = 8.518$ Å, which is in agreement with the previous report [100]. Furthermore, from the EDS measurements, we confirm that the atomic ratio of Mn : Fe is 1 : 2, indicating a stoichiometric composition.

Since the physical properties of this material is highly dependent on the oxidation states of the cations, we performed the XPS measurements on a single crystal of $MnFe_2O_4$ to probe the oxidation states of Mn and Fe. Figures 4.1(c and d) show the Mn-2p and Fe-2p core-level spectra, respectively. As shown in Figure 4.1(c), the Mn $2p_{3/2}$ peak splits into two peaks: a main peak at 641.0 eV and a satellite peak at 647.1 eV. The Mn $2p_{3/2}$ satellite peak is a characteristic of Mn^{2+}. As shown in Figure 4.1(d), a similar splitting of Fe $2p_{3/2}$ peak with the main peak at 710.0 eV and a satellite peak at 715.9 eV, which is a feature of Fe^{3+}. The satellite structures for both Fe and Mn, along with their sharpness (full width half max ∼4.5 eV for Fe 2p and ∼3.2 eV for Mn 2p), indicate that the majority

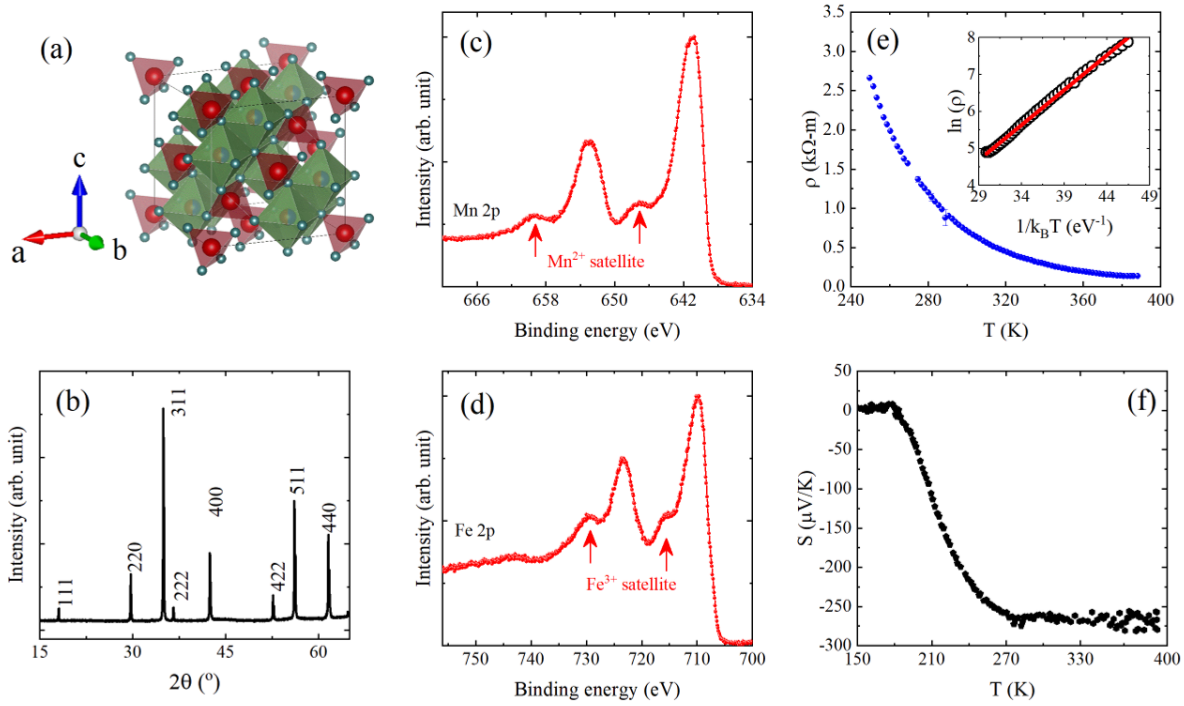

Figure 4.1. Structure, XPS spectra, electrical resistivity, and thermopower in $MnFe_2O_4$. (a) Crystal structure of $MnFe_2O_4$. (b) Room temperature XRD pattern from a crushed single crystal. (c-d) XPS core level spectra related to Mn 2p (c) and Fe 2p (d) regions, respectively. (e) Temperature dependence of electrical resistivity ρ. Inset: $\ln\rho$ as a function of inverse temperature $1/k_BT$. The solid line is the fit to $\rho(T) = \rho_0 e^{\Delta/2k_BT}$ (f) Temperature dependence of thermopower (S).

of the Fe and Mn ions in our samples are in the 3+ and 2+ states, respectively. To estimate the fraction of Fe^{3+} and Mn^{2+} cations in our single crystals, each XPS spectrum was fitted to four Gaussian-Lorentzian peaks after subtracting the Shirley background. The area under each peak was then calculated to estimate the ratios of Mn^{3+}/Mn and Fe^{2+}/Fe, both being $\sim$0.25. To ensure the fitting reliability, the branching ratio and full width at half maximum were held constant to extract the relevant area. According to the crystal field theory (Table 1.2), Mn^{3+} has a higher propensity towards the octahedral sites, while the Mn^{2+} tends to occupy the tetrahedral sites [36, 101, 102]. On the other hand, Fe^{2+} prefers the octahedral sites [36, 102]. Such preferential occupations are observed in spinels with mixed valence cations such as magnetite $Fe^{3+}[Fe^{3+}Fe^{2+}]O_4$ [103] and $Mn^{2+}[Mn^{3+}Mn^{3+}]O_4$ [47]. Additionally, the simulatneous presence of the Mn^{3+}/Fe^{2+} ion pairs in the nearest

neighboring sites have been observed in other manganese-rich manganese ferrites [104]. We thus assume that all Mn^{3+} and Fe^{2+} ions in our crystal reside in the octahedral sites, i.e. a cation distribution of $(Mn^{2+}_{0.75}Fe^{3+}_{0.25})_T[Mn^{3+}_{0.25}Fe^{2+}_{0.5}Fe^{3+}_{1.25}]_O O_4$.

The temperature dependence of electrical resistivity $\rho(T)$ is displayed in Figure 4.1(e). Note that ρ increases with decreasing temperature, and becomes too high to measure below 250 K, an indication of its insulating nature. Plotting data as $\ln(\rho)$ versus $1/k_BT$ as shown in the inset of Figure 4.1(e), we find it is more or less linear above 300 K. This suggests that the resistivity follows the thermally activated behavior. We thus fit the data to $\rho(T) = \rho_0 e^{\Delta/2k_BT}$, obtaining the activation energy $\Delta \sim 0.37$ eV. The solid line in the inset of Figure 4.1(e) is the fitting result, describing the experimental data well. Figure 4.1(f) shows the temperature dependence of the thermopower S. Due to its high electrical insulation, $MnFe_2O_4$ has a negligible thermopower below ∼200 K. Negative S is observed above ∼200 K, which increases with increasing temperature, corresponding to n-type charge carriers due to thermal activation. Above ∼ 270 K, thermopower shows very little temperature dependence, suggesting a saturation of carrier concentration.

Figure 4.2(a) shows the temperature dependence of magnetization M(T) under field H = 0.1 T (H ⊥ a) in both the zero-field cooling (ZFC) and field cooling (FC) modes. Upon cooling, M increases with a sharp rise below $T_{FI\text{-}1} \sim 575$ K, indicating the entrance of an ordered state. The transition temperature is close to the previously reported value [7], which was attributed to the transition from a high temperature paramagnetic to a collinear ferrimagnetic transition. Below $T_{FI\text{-}1}$, M continuously increases until $T_{FI\text{-}2} \sim 50$ K, as shown in the inset of Figure 4.2(a). This behavior is comparable to the low temperature transition in the case of $FeMn_2O_4$ and is similar to what is observed in many ferrimagnetic spinel systems due to a spin re-arrangement from high-temperature collinear to low-temperature non-collinear configuration [31, 46, 105]. Upon further lowering temperature, both ZFC and FC develop a kink at $T_x \sim 15$ K, suggesting a new magnetic state.

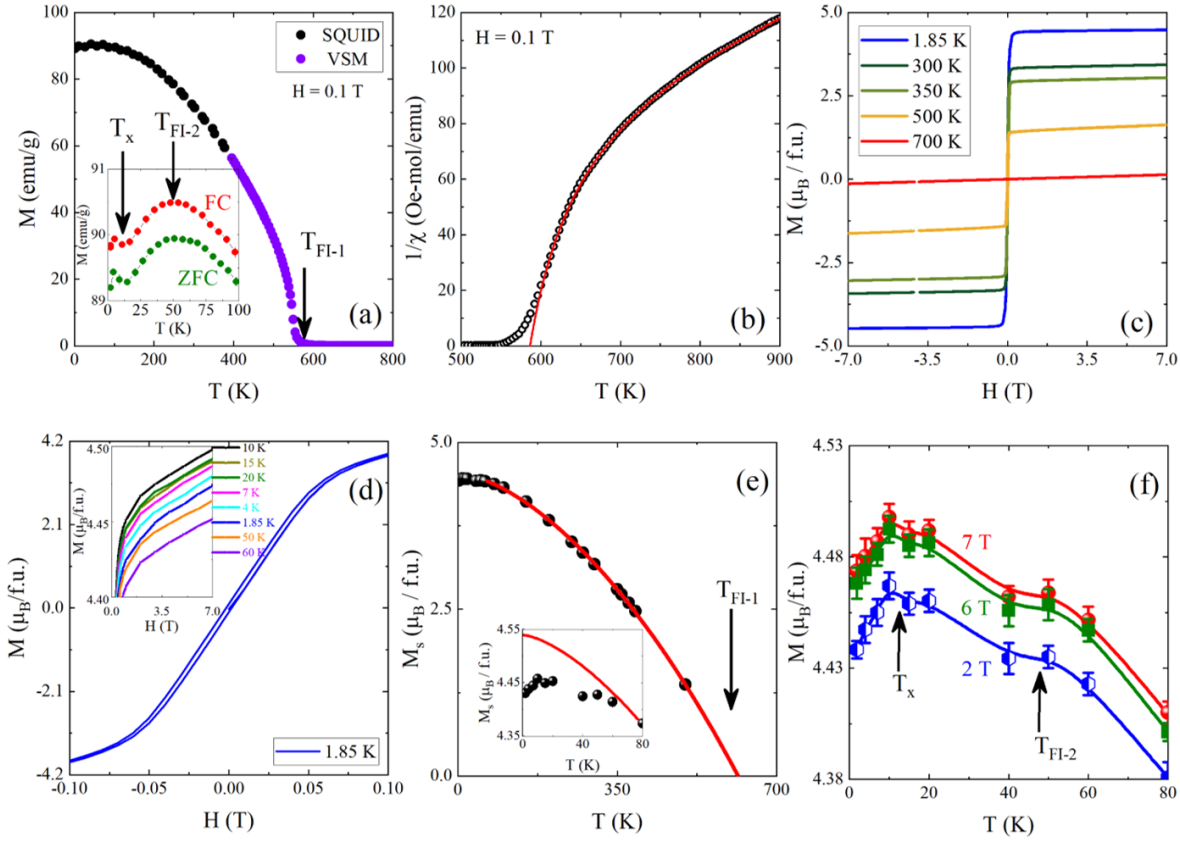

Figure 4.2. Magnetic properties of $MnFe_2O_4$.(a) Temperature dependence of the magnetization in $MnFe_2O_4$. Inset shows the magnified view of zero-field cooled (ZFC, green data points) and field cooled (FC, red data points) M(T) below 100 K, highlighting the anomalous behaviors at T_{FI-2} and T_x. (b) Temperature dependence of $1/\chi$ in the paramagnetic region. The red solid curve represents the best fit to the two-sublattice model. (c) $M(H)$ curves at indicated temperatures. (d) $M(H)$ hysteresis loop at 1.85 K. Inset shows the linear H dependence of M below 60 K. (e) Temperature dependence of spontaneous magnetization $M_s(T)$ with the low temperature data highlighted in the inset. (f) Low temperature magnetization data under H = 2, 6, and 7 T obtained from the $M(H)$ curves highlighting the anomalous behaviors at T_{FI-2} and T_x.

In order to elucidate the magnetic properties, we analyze the magnetic susceptibility (χ) in the paramagnetic region, which is displayed in Figure 4.2(b) as $1/\chi$ versus T. The solid curve in Figure 4.2(b) demonstrates the excellent fit of Eq. (1.15) to the experimental data with the fitting parameters θ_a = -401 K, C = 9.65 emu-K/mol, θ'= 524 K, and ξ = 6390 mol-K/emu. From the fitted value of C = 9.65 emu-K/mol, we can estimate the total effective magnetic moment to be $\mu_{eff} \sim 8.8\ \mu_B$/f.u. Theoretically, the magnetic moment

can be calculated using the usual relation $\mu_{theo} = \sqrt{\mu_{\mathrm{T}}{}^2 + \mu_{\mathrm{O}}{}^2}$, where μ_T and μ_O are the T- and O-sublattice magnetic moments, respectively. If Mn and Fe are in the high-spin state (S = 5/2 for both) [93], $\mu_{theo} \sim 10.2\ \mu_B$ is expected for $\alpha = 0$.

To further understand the nature of magnetic orders, we measured the isothermal magnetization M(H) as a function of applied magnetic field. The M(H) curves at selected temperatures are shown in Figure 4.2(c). At 700 K, M shows a linear dependence on H, indicating paramagnetic behavior above $\mathrm{T_{FI\text{-}1}}$. Below $\mathrm{T_{FI\text{-}1}}$, M(H) develops a non-linear dependence at low fields and quickly approaches saturation upon increasing magnetic field (H > 0.1 T). Figure 4.2(d) shows the hysteresis loop of M(H) at 1.85 K, with small coercive field ($\mathrm{H_c} \sim 0.005$ T). This indicates that the system has large magnetic permeability, which corresponds to the large saturation magnetization [106]. Interestingly, $\mathrm{H_c}$ is almost temperature independent in a wide temperature range, attesting to high-quality single crystal samples.

Strictly speaking, M is not completely saturated up to 7 Tesla as demonstrated in the inset of Figure 4.2(d). Above 2 Tesla, M(H) exhibits linear behavior with a positive slope. Extrapolating the linear behavior to H = 0, we obtain spontaneous magnetization, $\mathrm{M_s}$ (H = 0). The temperature dependence of $\mathrm{M_s}$ is presented in Figure 4.2(e). The overall $\mathrm{M_s(T)}$ profile is similar to M(T) (see Figure 4.2(a)), initially increasing from $\mathrm{T_{FI\text{-}1}}$, then decreasing with decreasing temperature below $\mathrm{T_x}$. At 2 K, $\mathrm{M_s}$ reaches ~4.5 μ_B/f.u. Above $\mathrm{T_{FI\text{-}2}}$, $\mathrm{M_s}$ can be described by the modified Bloch's law, $\mathrm{M_s(T) = M_s(0)(1\text{-}}B_1\mathrm{T^{3/2}\text{-}}B_2\mathrm{T^{5/2}})$, as indicated by the fitting curve. From the fit, we obtain $\mathrm{M_s(0)} = 4.54(1)\ \mu_B$/f.u., $B_1 = 4.97(9)\cdot10^{-5}\ \mathrm{K^{-3/2}}$, and $B_2 = 2.5(1)\cdot10^{-8}\ \mathrm{K^{-5/2}}$. The value of $\mathrm{M_s(0)}$, the spontaneous magnetization at 0 K, obtained from the fit is comparable to what was previously reported [92, 93]. According to Refs. [95, 107], $\mathrm{M_s}$ in manganese ferrites decreases with increasing inversion, $\mathrm{M_s(0)} = 5 - 2\alpha$. For $\mathrm{MnFe_2O_4}$, we estimate $\alpha \sim 0.23$. Furthermore, the Bloch's constant B_1 is related to the spin wave stiffness parameter D as $B_1 = 2.61V_0(k_B/4\pi D)^{3/2}$, where V_0 is the molar volume [108, 109]. For $\mathrm{MnFe_2O_4}$, we obtain $D \sim 174$ meVÅ^2, which

is comparable to the values reported for gallium-doped manganese spinel oxides and zinc-doped magnesium ferrites [110, 111]. As shown in the inset of Figure 4.2(e), M_s deviates from Bloch's law below $T_{FI\text{-}2}$. Especially, M_s decreases with decreasing temperature below T_x, reaching 4.43 μ_B at 1.85 K. This indicates magnetic rearrangement below T_x.

In Figure 4.2(f), we plot M(T) curves under H = 2 T, 6 T, and 7 T below 80 K obtained from the isothermal curves. Note that there is a downturn below T_x and a shoulder-like feature at $T_{FI\text{-}2}$. Interestingly, both T_x and $T_{FI\text{-}2}$ remain unchanged up to 7 Tesla. If the anomaly at T_x were due to low-lying excitation in Fe^{2+} [96], one would expect the increase of T_x and the suppression of the anomaly with increasing field because of Zeeman energy. Our result thus excludes this scenario. Recent theoretical calculations including direct exchange and super exchange interactions in $MnFe_2O_4$ have shown antiferromagnetic J_{OT} and J_{OO} for both normal ($\alpha = 0$) and inverse ($\alpha = 1$) cases [112]. The magnetic ground state can then be explained by the Yafet-Kittel extension to Néel's model, which predicts several non-collinear arrangements of spins [113]. The system may thus undergo several transitions from one type of spin arrangement to another upon varying temperature [113]. The suppression of M_s below $T_{FI\text{-}2}$ and the downturn of M(T) below T_x indicate stronger antiferromagnetic interaction with decreasing temperature.

A magnetic order involves a release of entropy manifesting as an anomaly in the specific heat. Figure 4.3(a) displays the temperature dependence of the specific heat at constant pressure (C_p) measured between 2 K and 250 K under H = 0 T and 5 T. The data is plotted in a log-log scale to highlight the low-temperature behavior. Note that there is no obvious anomaly in $C_p(T)$ near $T_{FI\text{-}2}$, which suggests that most of the magnetic entropy is removed at higher temperatures. On the other hand, there is a clear kink in C_p at T_x, which develops into a broad hump-like feature at $T < T_x$. This feature is present in both H = 0 T and 5 T with little magnetic field dependence, precluding the Schottky effect or low-lying excitation of Fe^{2+}. The persistence of the specific heat anomaly under field is consistent with what is observed in the magnetization (see Figure 4.2(f)).

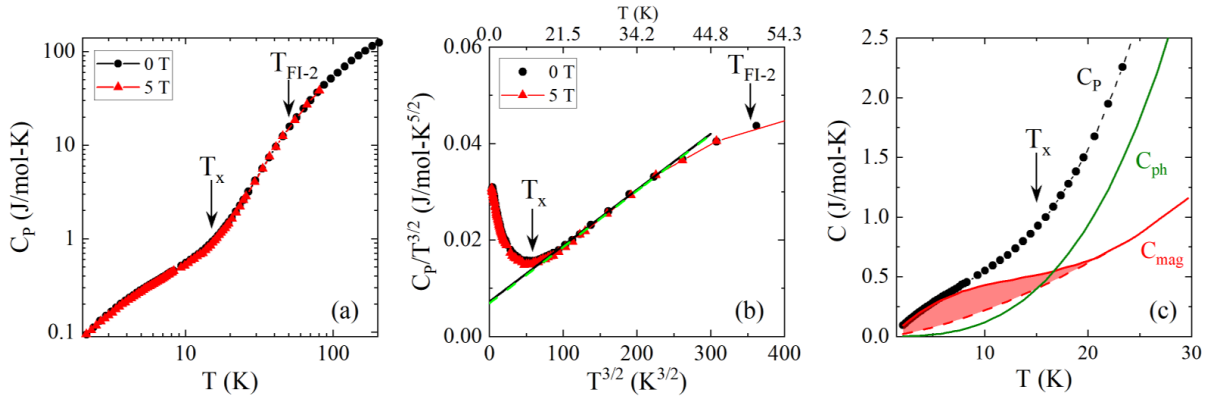

Figure 4.3. Specific heat of $MnFe_2O_4$. (a) Temperature dependence of specific heat of $MnFe_2O_4$ with H = 0 and 5 T. (b) $C/T^{3/2}$ versus $T^{3/2}$ below 45 K. (c) Various contributions to low temperature specific heat below 30 K. The dashed line represents the extrapolation of high-temperature $T^{3/2}$ behavior. The shaded region highlights the excess C_{mag} below T_x.

To understand the nature of the specific heat anomaly, it is necessary to separate various contributions to the specific heat. Since the specific heat of a ferrimagnetic system has contributions from the phonons (C_{ph}) and spin waves (C_{mag}), at sufficiently low temperatures, i.e. $T \ll \theta_D$(Debye Temperature), C_p should be described by the following equation:

$$C_p(T) = \beta T^3 + \delta T^{3/2}, \tag{4.1}$$

where the first term is the low temperature approximation of the Debye phonon specific heat, with $\beta = (12\pi^4/5)nR/\theta_D^3$ ($n = 7$ for $MnFe_2O_4$ and R is the universal gas constant), and the second term is the low temperature approximation of spin wave contributions [84]. Therefore, $C/T^{3/2}$ is expected to exhibit a linear function of $T^{3/2}$ at $T \ll \theta_D$. Figure 4.3(b) is the plot of $C/T^{3/2}$ versus $T^{3/2}$, which is linear only at $T_x < T < T_{FI\text{-}2}$. The solid line is the fit of data above T_x to Eq. (4.1). From the fit, β and δ are found to be $1.16(1)\cdot10^{-4}$ J/mol-K^4 and 0.0072(2) J/mol-K$^{5/2}$ for H = 0 T and $1.16(1)\cdot10^{-4}$ J/mol-K^4 and 0.0068(2) J/mol-K$^{5/2}$ for H = 5 T, respectively. As expected, the phonon specific heat is field independent, whereas there is slight suppression of magnetic specific heat at H = 5 T. From β, we can estimate the Debye temperature to be $\theta_D \sim 489$ K, which is comparable

to previously reported value [87]. On the other hand, the δ value decreases with increasing H, suggesting the suppression of antiferromagnetic interactions under magnetic field at $T_x < T < T_{FI\text{-}2}$. Figure 4.3(c) shows the temperature dependence of the total specific heat C_p, the phonon contribution C_{ph}, and the magnetic contribution C_{mag}. Note that $C_{mag} > C_{ph}$ and clearly deviates from high-temperature $T^{3/2}$ dependence (dashed line) below T_x.

The thermal conductivity κ of a system depends intimately on the specific heat as $\kappa \sim (1/3)Cvl$ for a 3D system, where v is the velocity and l is the mean free path of the heat carriers (phonons, electrons, magnons) [114]. It can therefore help shed light on the intrinsic characteristics of an insulating magnetic system, probing particularly magnetic excitations. Figure 4.4(a) shows the temperature dependence of κ in $MnFe_2O_4$ between 2 K and 400 K, measured with H = 0 T and 14 T applied perpendicular to the applied heat current. Note that κ(T) shows the typical temperature dependence for a single crystal sample: upon heating up, κ initially increases then decreases after reaching a peak near $T_{FI\text{-}2}$. Under the application of a 14 T magnetic field, κ(T) exhibits the same profile, but with a significant suppression of the peak magnitude. Since its position is unchanged under 14 T, the thermal conductivity peak should be related to the magnetic rearrangement at $T_{FI\text{-}2}$ rather than reaching the maximum phonon mean free path. Especially, the magnetic field effect occurs below $\sim 2T_{FI\text{-}2}$, as can be seen in the inset of Figure 4.4(a). The magneto-thermal conductivity, $[\kappa(H,T)\text{-}\kappa(H=0,T)]/\kappa(H=0,T)]$, initially increases in magnitude, then decreases after reaching a maximum near $T_{FI\text{-}2}$. Below T_x, the magneto-thermal conductivity becomes positive. The negative magneto-thermal conductivity can be explained by an increase in phonon-magnon scattering under magnetic field. The non-collinear magnetic ordering at $T_{FI\text{-}2}$ disfavors the thermal transport. Upon further cooling the sample, the magneto-thermal conductivity changes sign at T_x, implying that the magnetic moment is more ordered under field below T_x.

To explain the origin of the positive magneto-thermal conductivity, it is important to know the mechanism of the thermal transport in the system. In a non-magnetic insulator,

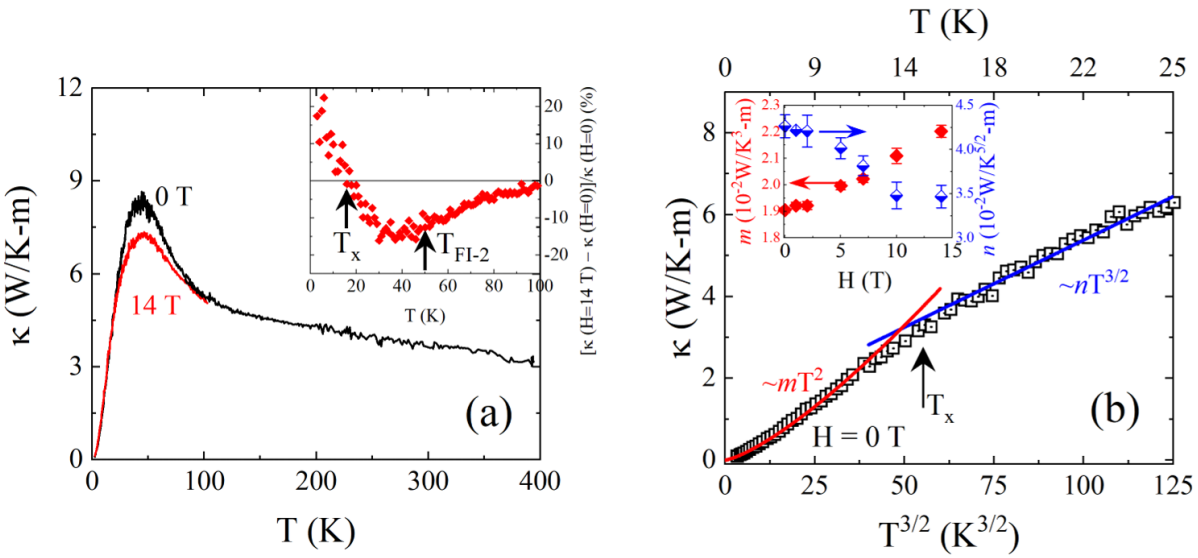

Figure 4.4. Thermal conductivity in $MnFe_2O_4$. (a) Temperature dependence of thermal conductivity in the presence of H = 0 T (black curve) and H = 14 T (red curve) magnetic field applied perpendicular to the direction of thermal current. Inset: Temperature dependence of magneto-thermal conductivity at H = 14 T. (b) Low field thermal conductivity with H = 0 T plotted as a function of $T^{3/2}$. The solid blue and red curves show the $T^{3/2}$ and T^2 dependence of thermal conductivity above and below T_x, respectively. Inset: Magnetic field evolution of the low temperature fitting parameters m and n.

phonon is the sole carrier of heat with $\kappa_{ph} \propto T^3$ at low temperatures [114, 115]. For $MnFe_2O_4$, heat can be transported by phonons and magnons, i.e. $\kappa \sim \kappa_{ph} + \kappa_{mag}$ [114]. Despite a simple linear dependence of thermal conductivity on phonon and magnetic specific heat, it is difficult to separate the two contributions because the drift velocity and mean free path of magnons can be temperature dependent even at low temperatures. Furthermore, magnons and phonons can scatter each other and affect the total thermal conductivity. Nevertheless, the low temperature behavior of κ can provide several insights about the mechanism of heat transport in the system. Figure 4.4(b) shows the low temperature zero field κ as a function of $T^{3/2}$, where it can be clearly seen that κ shows different temperature dependence above and below T_x. Above T_x, κ shows a linear dependence on $T^{3/2}$, whereas below T_x, it shows a T^2 dependence. The experimental data can be fitted well by $\sim mT^2$ at $T < T_x$ and $\sim nT^{3/2}$ at $T > T_x$, as shown by the solid curves in Figure 4.4(b). The inset of Figure 4.4(b) shows the effect of magnetic field on the coefficients m and n. With

increasing magnetic field, m increases, but n decreases. The $T^{3/2}$ nature of κ above T_x indicates that $\kappa \propto C_{mag}$ at $T_x < T < T_{FI\text{-}2}$. The decrease of n with increasing field suggests that field suppresses the $T_{FI\text{-}2}$ ordering, i.e. disfavoring canted magnetic ordering. At lower temperatures ($T \ll \theta_D$) where the mean free path is greater than the crystal size, the magnon thermal conductivity is of the form $\kappa_m = (\zeta(3)k_B^3 l_m/4\pi^2\hbar D)T^2$, where $\zeta(3) \sim 1.202$, l_m is the magnon mean free path, and $\hbar$ is the Planck's constant [115]. The observed T^2 dependence of the thermal conductivity below T_x indicates that magnons dominate thermal conduction process at low temperatures, and the enhanced m under field implies longer l_m. This further implies that the magnetization is more ordered under field below T_x.

4.3 Conclusion

In summary, we have investigated the bulk physical properties of single crystals of $MnFe_2O_4$ synthesized via floating zone technique. In addition to the high-temperature paramagnetic to ferrimagnetic transition at $T_{FI\text{-}1} \sim 575$ K, the magnetization, specific heat, and thermal conductivity show two additional anomalies at $T_{FI\text{-}2} \sim 50$ K and $T_x \sim 15$ K. Magnetic field suppresses the spin wave contribution at $T_x < T < T_{FI\text{-}2}$ but enhances the magnetic contribution below T_x. This indicates different spin configurations in these two states.

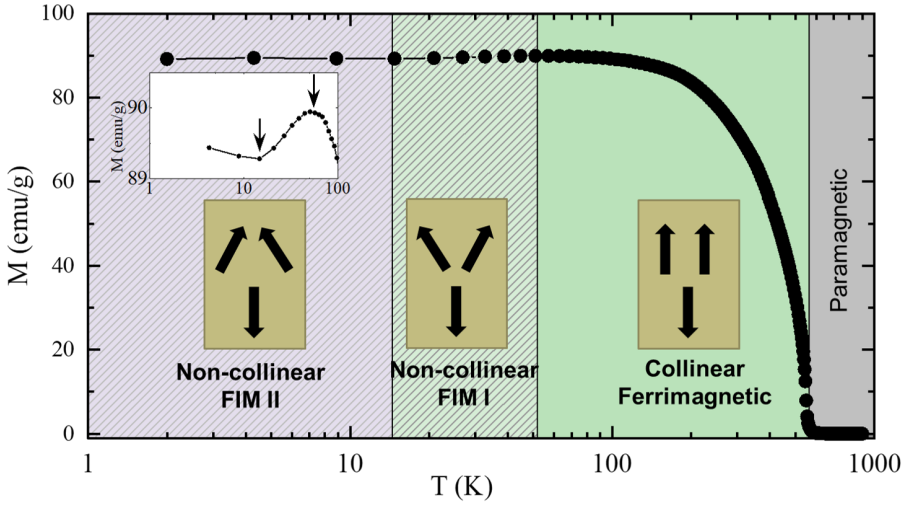

Figure 4.5. A summary of magnetic phase transitions in $MnFe_2O_4$.

Chapter 5
Emergent Spin Glassy Behavior in $NiFe_2O_4$ with Self-assembled NiO Columns

5.1 Motivation

Spin glass (SG) is one of the magnetic systems in which the magnetic interactions are competing with each other preventing the formation of the conventional long-range magnetic orders [10, 116]. First observed in the dilute solutions of manganese in copper in the mid-20th century [117–119], its similarity to structural glass inspired the term spin glass [120]. The physics of spin glass has attracted interests from not only condensed matter physicists but also scientists from fields such as mathematics, computer science, and biology. This is because SG displays features that are widespread in several complex phenomena. For example, SG models have been used to analyze interesting real-world problems such as the Traveling Salesman Problem in the field of combinatorial mathematics [121, 122], to model neural networks [122] and protein folding dynamics [123], to design new algorithms for image restoration [124] and machine learning [125], and even to model for the collective price changes of stock portfolios [126]. SG models have also been proposed to study the accuracy threshold in quantum computation algorithms [127]. As a result, SG, which were once thought to be lacking much intellectual glamor [128], have continuously sparked interest among the research community.

In the search for novel magnetic states, such as the SG state, interfaces between materials have proven to be a fertile ground [129–132]. The symmetry breaking and the spin-orbit coupling at the interface between two materials with different magnetic properties can give rise to a plethora of interface-induced magnetic properties [129, 133]. There have been some recent reports on the emergence of interfacial spin glass states in bilayers of materials with competing magnetic orders due to the Dzyaloshinskii-Moriya (DM) and spin frustration arising from the competing interactions at the interface [132, 134]. A SG-like state could also arise from the spin fluctuations resulting from the noncoplanar spin

configurations at the interface [116]. However, the effects of interfaces are only significant in systems with a high surface-to-material volume ratio. This limits the types of systems suitable for the exploration of interfacial effects to thin films, heterostructures, and superlattices and prohibits the use of bulk single crystals. In theory, the requirement of a large surface-to-material interface volume ratio could be achieved in bulk single crystals by the presence of a large number ordered nano- or micro-structures inside a single crystal, effectively creating an array of interfaces. Lithography could be an avenue to obtain such structures in single crystal samples. Recently, magnetic skyrmion lattice was reported in a hybrid structure with arrays of cobalt nanodots grown on magnetic thin films using electron beam lithography [135]. If such a technique could be expanded to implement the nano- or micro-structures within the sample, it would open a new door to exploit the interfaces. Alternatively, single crystals with naturally assembled microstructures during the crystal growth process could be exploited to gain insights in the interface physics. These naturally occurring micro-structures might even hold an edge over the artificially created ones, as their formation is governed by thermodynamics during the crystal growth process and can be free from the restrictions imposed during the artificial implantation process. More importantly, the current techniques used to create interfaces via thin film growth, or hypothetically, via lithography are highly expensive, as opposed to relatively cheaper process of single crystal growth. Therefore, investigation of single crystals with naturally self-assembled micro-structures could help us understand how the interfaces affect the physical properties in a large scale and at a much cheaper price point.

In this chapter, we present a case study of interface-induced magnetic behavior in $NiFe_2O_4$ containing self-assembled micro-columns of crystalline NiO. As shown in Figure 5.1(a and b), $NiFe_2O_4$ has a spinel structure (symmetry $Fd\bar{3}m$), whereas NiO has a rock-salt type crystal structure (symmetry $Fm\bar{3}m$). The lattice parameter of $NiFe_2O_4$ is about two times that of NiO, potentially allowing them to grow congruently. $NiFe_2O_4$ is known to order ferrimagnetically (FI) with the transition temperature $\sim$860 K [7]. In its spinel

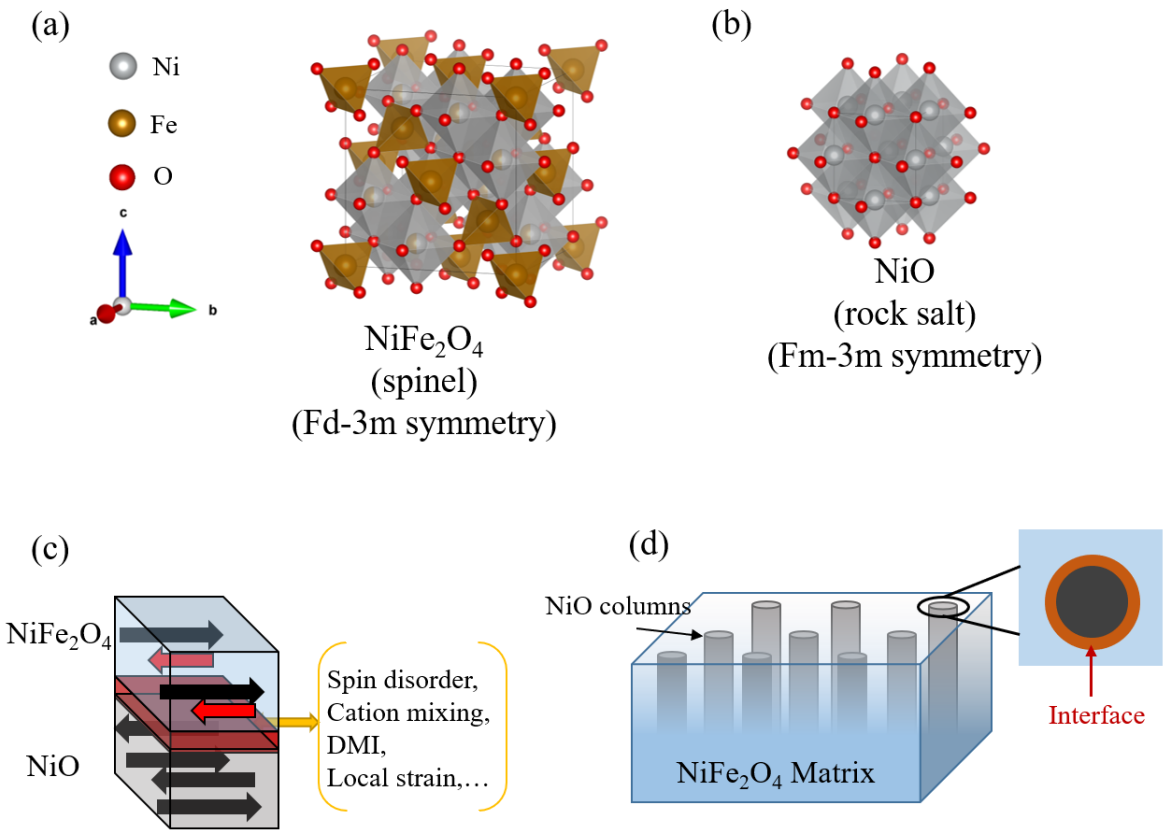

Figure 5.1. (a and b) Crystal structures of $NiFe_2O_4$ and NiO, respectively. (c) A schematic of $NiFe_2O_4$-NiO bilayer highlighting the emergent complexities at the interface. (d) An envision of self assembled microcolumns within a single crystalline matrix.

structure, the diamond-like tetragonal (T) sublattice sites are occupied mostly by Fe^{3+} ions, whereas the pyrochlore-like octahedral (O) sublattice sites are occupied randomly by Fe^{3+} and Ni^{2+} ions. The strongest exchange interaction is the O-T interactions [136], leading to an antiparallel ferrimagnetic arrangement of spins in the two sublattices, with the easy axis along the [111] direction. In contrast, NiO has an AFM order with Néel temperature ~523 K, where the Ni^{2+} spins are constrained to lie in the {111} planes forming the FM sheets that are coupled antiferromagnetically to the neighboring sheets [137, 138]. Their drastically different magnetic orders and compatible crystal structures have made them a popular pair in the study of interface physics in bilayer thin films and core-shell nanoparticles [139, 140]. Here, we have grown single crystal samples of $NiFe_2O_4$ with naturally assembled single crystalline NiO micro-structures and systematically studied the emergent magnetic

properties via bulk magnetization measurements and microscopic investigations via scanning electron microscope (SEM), scanning transmission electron microscopy (STEM), and magnetic force microscopy (MFM). The analysis of our bulk measurements indicates the existence of a spin glass state below $T_{SG} \sim 28$ K with magnetic memory effect, dynamic spin relaxation, and frequency-dependent ac susceptibility. The microscopic measurements revealed the presence of highly organized NiO columns within the matrix of $NiFe_2O_4$. We show that the low temperature spin glass state is due to the interface effects between the two magnetically, structurally, and chemically distinct regions.

5.2 Results and discussion

The single crystal samples containing self-assembled columns were grown via floating zone technique. First, polycrystalline $NiFe_2O_4$ was synthesized from a solid state reaction of a molar ratio mixture of Fe_2O_3 and NiO. The mixture was heated to 1250°C, kept there for 12 hours, and slowly cooled to room temperature. The end product of the reaction was ground and its phase purity was determined via x-ray diffraction (XRD). Figure 5.2(a) shows the room temperature XRD pattern obtained from the polycrystalline $NiFe_2O_4$. As indicated by the red vertical lines, all diffraction peaks could be indexed with the spinel $Fd\bar{3}m$ symmetry, demonstrating the phase purity of the sample. Figure 5.2(b) shows the temperature dependence of dc magnetic susceptibility in the polycrystalline sample measured under 0.1 T magnetic field from 400 K to 2 K (purple triangles), which shows that the sample is magnetically ordered in the temperature range with a much higher transition temperature (dashed line), as expected for $NiFe_2O_4$.

The seed and feed rods were prepared from the polycrystalline $NiFe_2O_4$. The self assembly of NiO columns within the $NiFe_2O_4$ matrix requires heating the raw materials to a temperature higher than the melting points of both $NiFe_2O_4$ (∼1600°C) and NiO (∼1955°C) [141], which can be easily achieved in the floating zone furnace. To determine the optimal growth condition, we started by growing single crystals in a 1 MPa oxygen atmosphere. A photograph of a representative crystal is presented in the inset of Figure 5.3(a) along

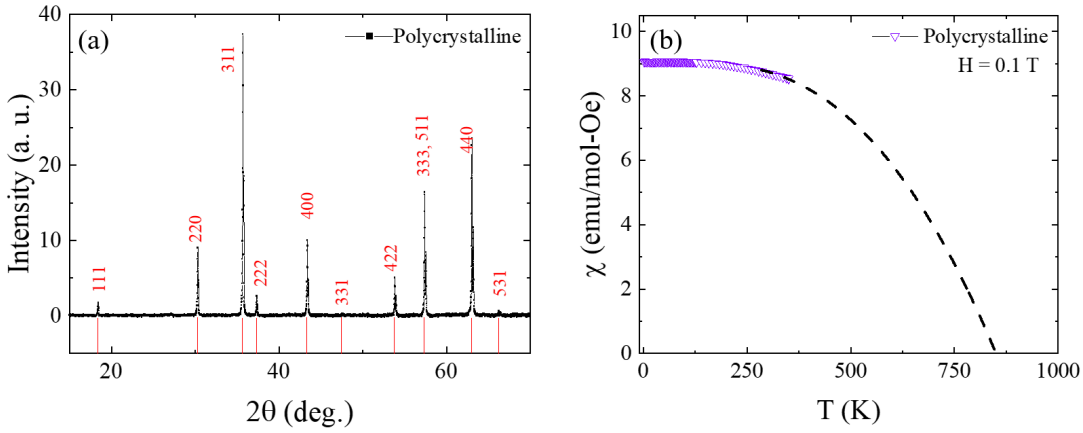

Figure 5.2. Polycrystalline $NiFe_2O_4$. (a) Room temperature XRD pattern from polycrystalline $NiFe_2O_4$. (b) Temperature dependence of dc susceptibility in polycrystalline $NiFe_2O_4$ measured under 0.1 T magnetic field. The dashed line shows that the magnetic transition occurs at a much higher temperature, as expected.

with the room temperature XRD pattern obtained from a crushed single crystal. All of the observed peaks belong to $NiFe_2O_4$ and no obvious impurities were detected. Figure 5.3(b) shows the temperature dependence of dc magnetic susceptibilities in the polycrystalline sample (purple points) and the single crystal (red points). At a first glance, both samples show similar behavior with a high transition temperature. The smaller magnitude of susceptibility in the polycrystalline sample is expected as the measurement on a polycrystalline sample yields a value averaged over many tiny crystallites oriented in different directions. A closer inspection of the data, highlighted in the inset of Figure 5.3(b), shows that the susceptibility in the single crystal sample shows an anomalous downturn. The downturn, which is absent in the polycrystalline sample, demonstrates that the low temperature magnetic state of the single crystal sample is different from that of the polycrystalline sample.

Having observed the anomalous behavior in the crystal grown under oxygen pressure, we changed the crystal growth condition in an effort to enhance the low temperature anomaly. Figure 5.4(a) shows the room temperature XRD pattern obtained from a single crystal grown under a flowing oxygen atmosphere, along with a photograph of a representative sample in the inset. Just like before, we did not observe any impurity peaks in

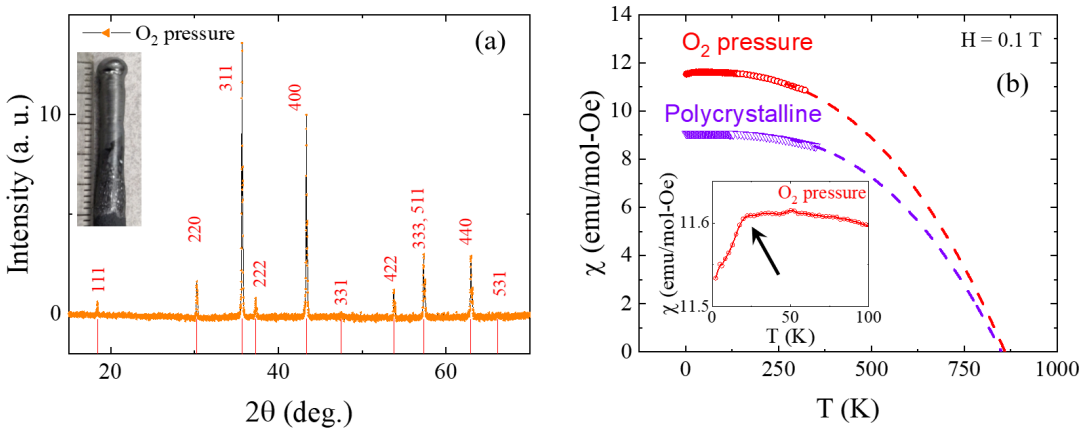

Figure 5.3. $NiFe_2O_4$ single crystal C1. (a) Room temperature XRD pattern from crushed single crystal $NiFe_2O_4$ grown under 1 MPa oxygen pressure. Inset shows a representative single crystal sample. (b) Temperature dependence of dc susceptibility in polycrystalline $NiFe_2O_4$ (purple points) and single crystal $NiFe_2O_4$ grown under 1 MPa oxygen gressure (red points) measured under 0.1 T magnetic field. Inset highlights the low temperature anomalous drop in susceptibility in the single crystal sample.

the XRD pattern and all of the observed peaks belong to $NiFe_2O_4$. Figure 5.4(b) shows a comparison of magnetic susceptibilities in the single crystal grown under oxygen flow (black points) and the polycrystalline sample (purple points). As highlighted in the inset, the low temperature anomaly is more pronounced in this sample.

Figure 5.5 shows the temperature dependence of normalized magnetic susceptibilities below 100 K in polycrystalline sample (P) and single crystals grown under 1 MPa oxygen pressure (C1) and under a flowing oxygen atmosphere (C2). Clearly, the low temperature anomaly is sample-dependent. It is not present in the polycrystalline sample and is enhanced in crystal C2. Seemingly, the oxygen pressure environment during the crystal growth process suppresses the anomalous behavior. To determine the nature of the low temperature anomaly and its origin, we undertook further microscopic and macroscopic measurements on single crystal C2.

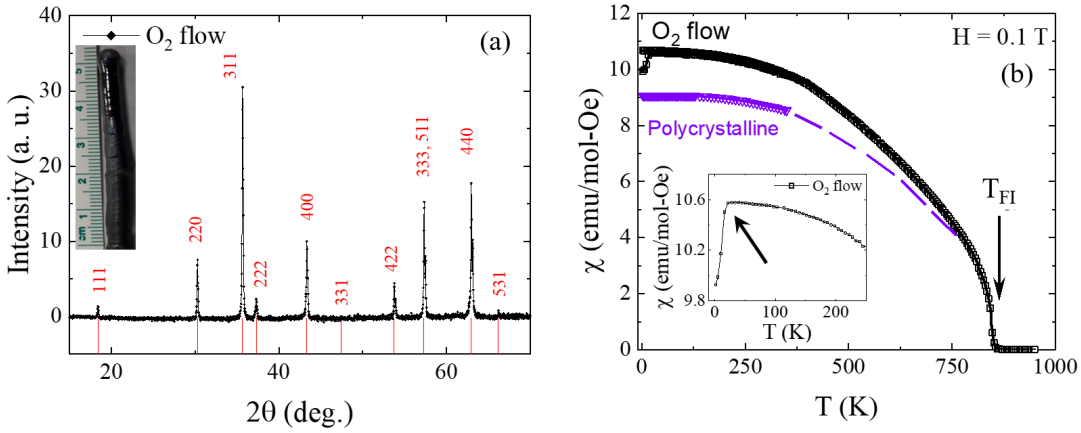

Figure 5.4. $NiFe_2O_4$ single crystal C2. (a) Room temperature XRD pattern from crushed single crystal $NiFe_2O_4$ grown in a flowing oxygen gas atmosphere. Inset shows a representative single crystal sample. (b) Temperature dependence of dc susceptibility in polycrystalline $NiFe_2O_4$ (purple points) and single crystal $NiFe_2O_4$ grown in a flowing oxygen gas atmosphere (black points) measured under 0.1 T magnetic field. Inset highlights the low temperature anomalous drop in susceptibility.

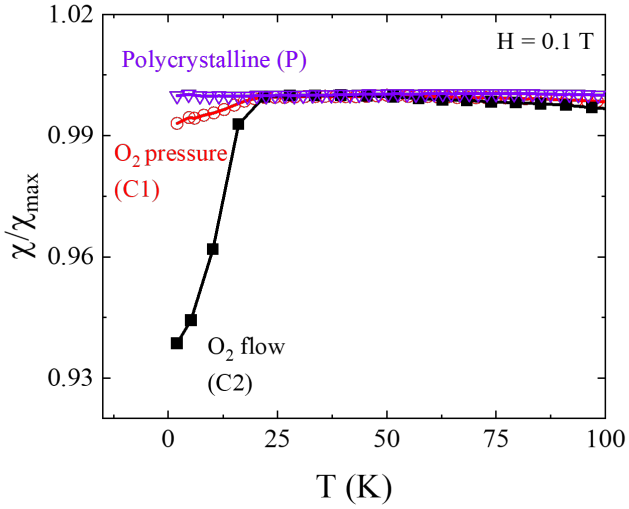

Figure 5.5. Temperature dependence of normalized magnetic susceptibility in polycrystalline and two single crystal samples highlighting the low temperature anomaly.

A disk parallel to the crystal growth direction ([111] direction) was cut from the crystal C2, as shown in Figure 5.6(a). The disk was polished mechanically up to a sub-micron roughness and SEM images of the surface were taken. Figure 5.6(b) shows a representative SEM micrograph obtained from the disk. The micrograph shows a striking presence of

a secondary phase (light colored region) embedded within a matrix of main phase (dark colored region). The hexagonal shaped columns are naturally organized and are distributed almost uniformly within the main matrix. The inclusions make up about 10 - 15% of the total area and have a typical edge length of about $\sim$4 μm. The hexagonal columns are oriented vertically parallel to the direction of crystal growth and have a typical separation of 23 ± 3 μm. In some cases, the closely located columns appear to have merged together. Figure 5.6(c) is a close-up SEM image of a column showing the irregular hexagonal cross section of the columns.

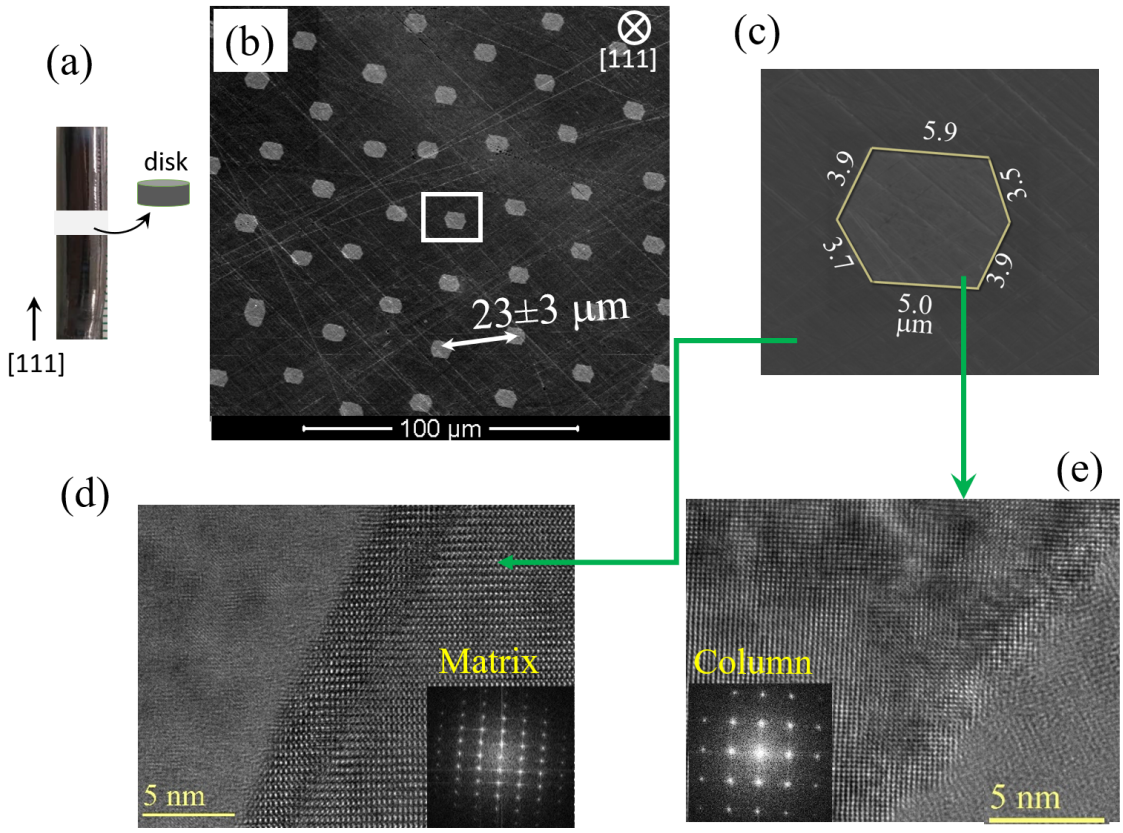

Figure 5.6. SEM and TEM images of $NiFe_2O_4$ single crystal C2. (a) Optical photograph of the single crystal showing the SEM sample preparation process. (b) SEM micrograph of the polished disk showing self-assembled hexagonal columns (light contrast) in a matrix of the primary phase (dark contrast). (c) A magnified view of the hexagonal column highlighted in (b) by a white square. (d and e) TEM images obtained from the matrix and column, respectively. The insets show the respective 2D FFT images.

To get a fundamental understanding of the secondary phase, TEM samples containing both matrix and columns were prepared. Figures 5.6(d and e) show the large area STEM images obtained from the main matrix phase and the column, respectively. Both regions show high crystallinity. The diffraction spots obtained from the fast Fourier transform (FFT, Figures 5.6(d and e) insets) from the two regions clearly show that they have distinct crystal structures. For accurate determination of the structure and lattice parameters of the two regions, we collected selected area electron diffraction (SAED) patterns. Figure 5.7(a) shows the SAED patterns obtained from the matrix along the [100] and [111] direction. The top and bottom panels show the experimental data and the simulated pattern for the spinel structure, respectively. The experimental data show an excellent agreement with the simulated pattern, confirming that the main matrix crystallizes in the spinel structure. The experimental SAED pattern obtained from the columns are shown in Figure 5.7(b). The observed pattern (top) agrees with the a rock-salt type structure, i.e. NiO structure (bottom). By collecting the SAED patterns along several directions, we obtained the lattice parameters of the matrix to be $a \sim 8.36$ Å and that of the columns to be $a \sim 4.18$ Å.

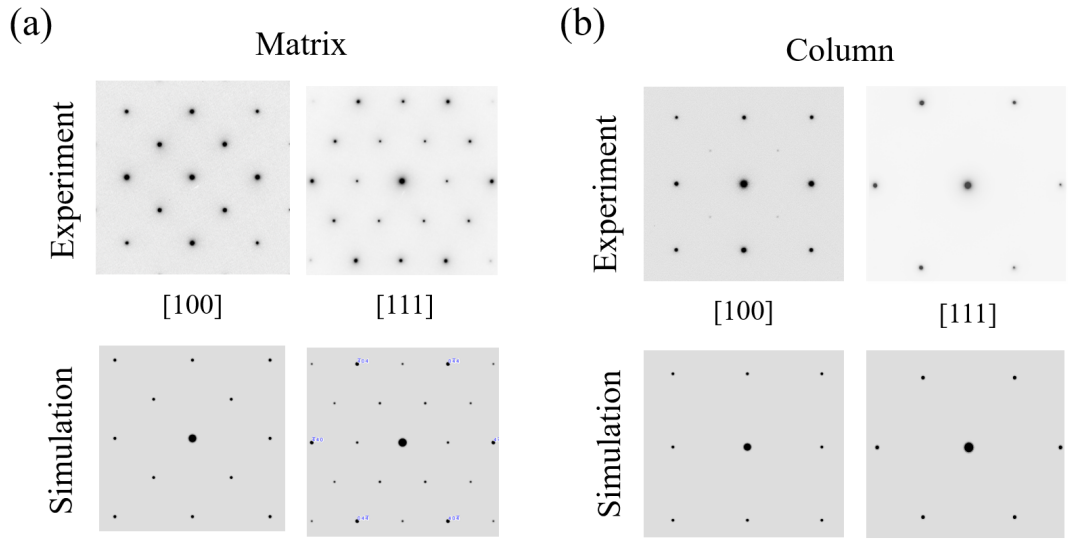

Figure 5.7. Selected area electron diffraction (SAED) patterns of (a) the matrix and (b) the column. The SAEDs were taken along [100] and [111] directions. Both experimental data (upper row) and simulated patterns (lower row) are presented.

For a detailed atomic structure, we obtained high resolution STEM images. Figure 5.8(a) shows a STEM image of a region containing both matrix and column phases, with the interfacial region highlighted in panel (b). Figure 5.8(c and d) show the HAADF- and ABF-STEM images obtained from the matrix and the column viewed along [110] direction, respectively. The two-dimensional atomic arrangements of spinel structure ($Fd\bar{3}m$) and rock-salt structure ($Fm\bar{3}m$) are overlaid on the experimental data for comparison and show excellent agreements. Despite having different symmetries $Fd\bar{3}m$ and $Fm\bar{3}m$, both spinel and rock-salt structures have the same close-packed anions stacking sequence, i.e. the spinel can be transformed to a rock-salt and vice versa by simple rearrangements of cations without changing the oxygen framework [142]. The spinel oxide (AB_2O_4) structure can be written as $(A)_{8a}[BB]_{16d}[\square]_{16c}O_4$, where 8a, 16c, and 16d denote the Wyckoff positions in the unit cell. In this arrangement, the 8a and 16d Wyckoff positions are occupied by the cations whereas the 16c positions are vacant [143]. When viewed along [110] direction, this atomic arrangement creates an array of inter-penetrating diamonds formed by the octahedral (16d) cations and hexagons formed by the tetrahedral (8a) cations. Our experimental data displayed similar behavior, as highlighted by the solid lines in the HAADF images in Figure 5.8(c). The center of each diamond in the HAADF image where there is no contrast represents the 16c Wyckoff position that is vacant. In the rock-salt structure, these 16c positions are not vacant; rather, they are occupied by the cations along with the 16d positions, leaving the 8a positions vacant. When viewed along [110] direction, the vacancies at the tetrahedral sites result in the absence of the hexagonal pattern in the atomic arrangement, leaving just the array of diamond structures formed by the 16d cations with the 16c cations located at the center of the diamonds. This agrees with our STEM images from the self-assembled columns as shown in Figure 5.8(d).

To quantitatively determine the chemical composition in the two phases, we utilized the electron energy-loss spectroscopy (EELS) elemental mapping. Figures 5.9(a–d) show the HAADF-STEM images and EELS elemental maps of O, Fe, and Ni across the interface

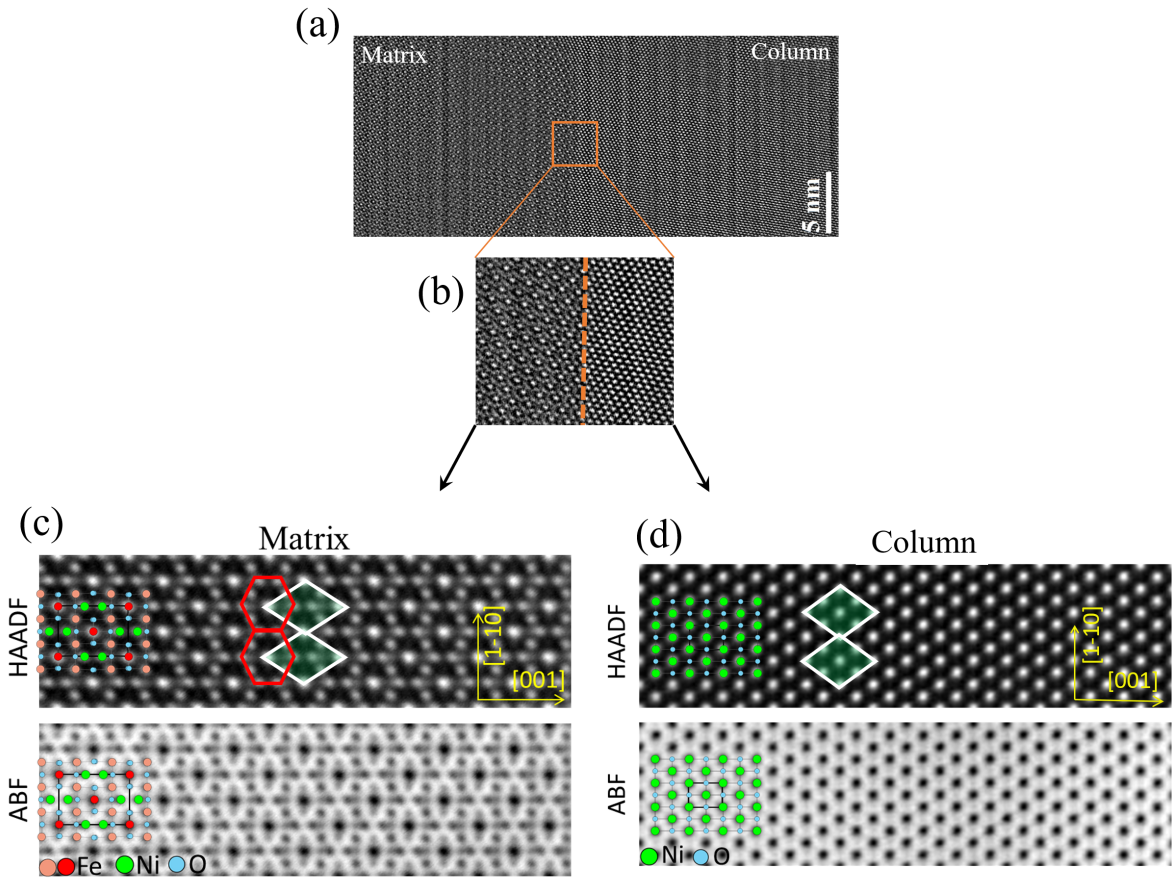

Figure 5.8. Atomically resolved STEM images. (a) Large area STEM image of the matrix and column with the interface region highlighted in (b). (c and d) High magnification HAADF- and ABF-STEM images of matrix and column, respectively, taken along [110] direction. The $NiFe_2O_4$ and NiO crystal structures are superimposed.

between the two phases. The yellow dotted line represents the interfacial region. While the oxygen distribution is homogenous in both phases as well as the interface, there are glaring differences in the iron and nickel distributions. The column phase is composed of mostly nickel with a trace amount of iron, whereas the matrix phase is composed of more iron than nickel, as expected for $NiFe_2O_4$. Figures 5.9(e–g) show the background subtracted EELS spectra of the O-K, Fe-L, and Ni-L edges, respectively, from the column phase and matrix phase. The spectra were normalized by the intensity of the O-K edge. The binding energy of the Fe-L edge is lower in the rock-salt phase, indicating a lower Fe valence state than the Fe^{3+} in the $NiFe_2O_4$ phase. In contrast, the binding energy of the Ni-L edge remains the

same in both phases. These results are consistent with the presence of Ni^{2+} and Fe^{3+} in the spinel phase and Ni^{2+} and Fe^{2+} in the column phase. The Fe : Ni ratio (R) was obtained from the integrated intensity of Ni-L and Fe-L edges. The Fe : Ni ratio profile across the interface, plotted in Figure 5.9(h), shows that the ratio R is close to 0 in the column and increases to the value of 2, corresponding to $NiFe_2O_4$ across the interface. Furthermore, the intensity ratio profile also shows that there is a gradual change in the Fe : Ni ratio across the interface, highlighting cation intermixing in ~2 nm region around the interface.

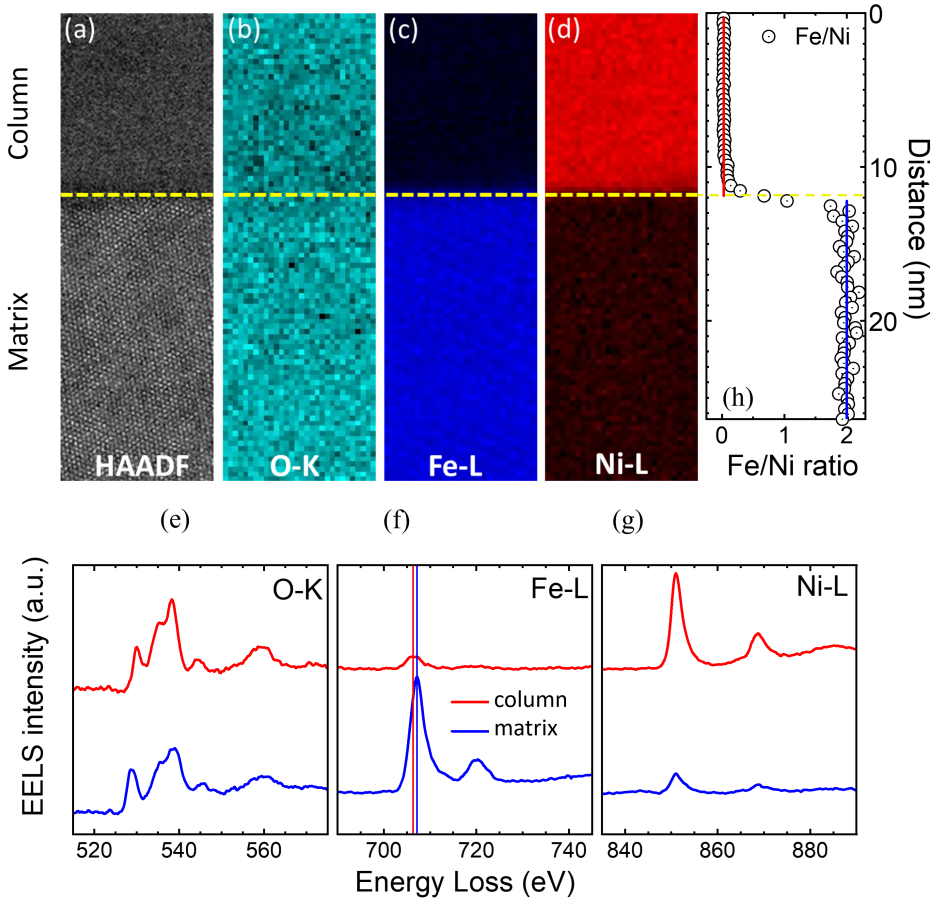

Figure 5.9. Electron Energy Loss Spectroscopy (EELS) data. (a) HAADF-STEM image and EELS elemental maps of (b) O, (c) Fe, and (d) Ni across the interface marked by the yellow line. (e-g) Background subtracted EELS spectra of O-K, Fe-L, and Ni-L edges, respectively. The EELS spectra were normalized by the intensity of O-K edge.(h) Profile of Fe/Ni ratio across the interface.

In addition to the vertical columns of NiO aligned along the $NiFe_2O_4$ crystal growth direction, we also observed horizontally aligned columns lying perpendicular to the crystal growth direction. Figures 5.10(a and b) show the SEM images of the region containing the horizontal columns. They too depict a stricking self-assembly, with an average separation of 21 ± 3 μm, and are structurally identical to the vertical columns, as demonstrated in the TEM images shown in Figures 5.10(c–e).

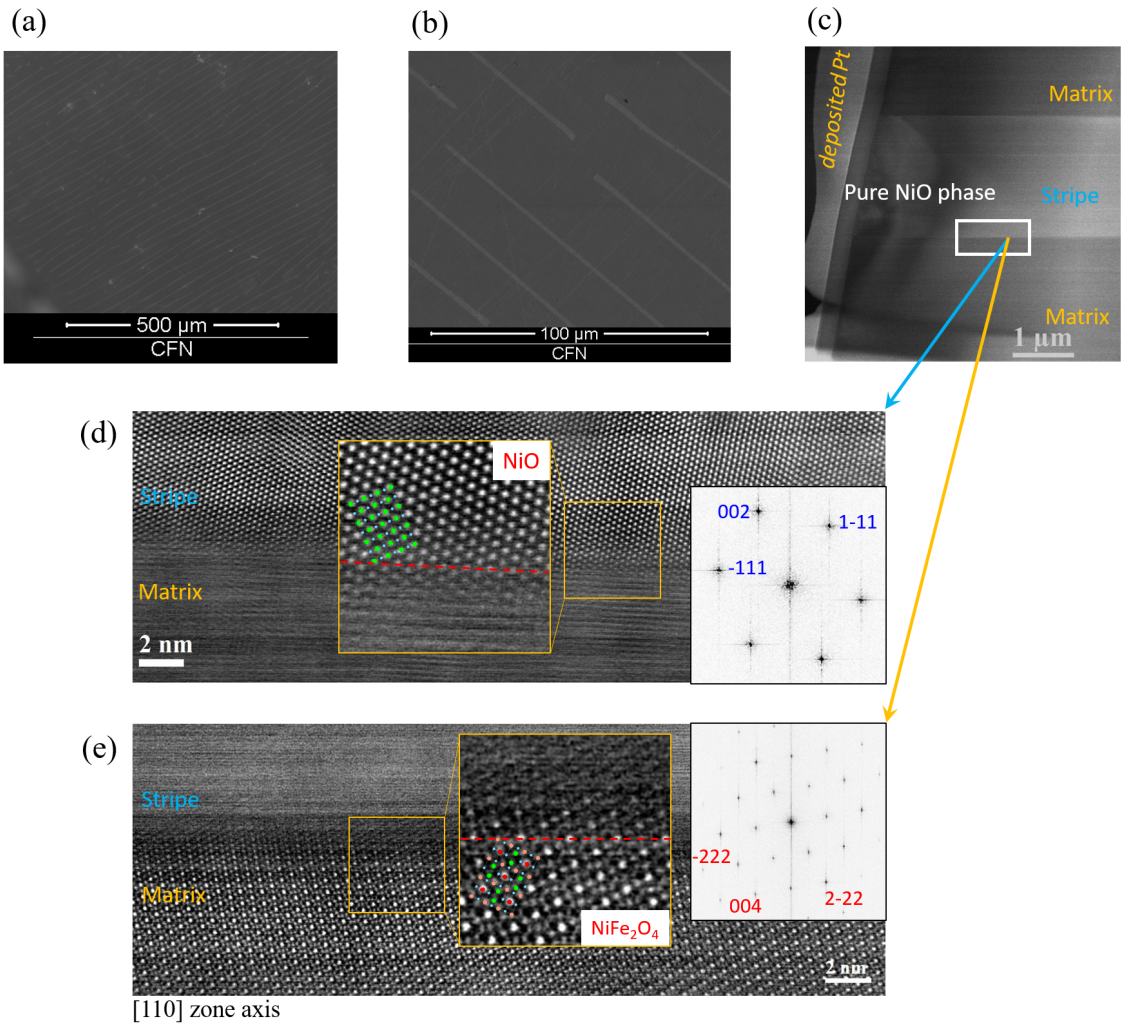

Figure 5.10. Horizontally aligned NiO columns. (a) A large scale SEM image showing horizontal NiO columns. (b) A magnified view of the column. (c) A representative TEM sample containing the spinel matrix and the horizontal column. (d and e) Atomically resolved STEM images obtained from the vertical column and matrix, respectively. The respective insets show a magnified view of the atomic arrangement and the 2D FFT images.

To determine the orientation of the NiO columns with respect to the matrix phase, we obtained STEM images and SAED patterns by aligning the samples along several crystallographic direction of the $NiFe_2O_4$ matrix phase. Our analysis revealed that the NiO columns grow along their crystallographic [211] direction. Therefore, the mutual orientation of the matrix and the columns can be written as $[211]_{NiO}/[111]_{NiFe_2O_4}$. Figure 5.11 shows the schematic of the arrangement of the self-assembled NiO columns embedded within the $NiFe_2O_4$ crystal.

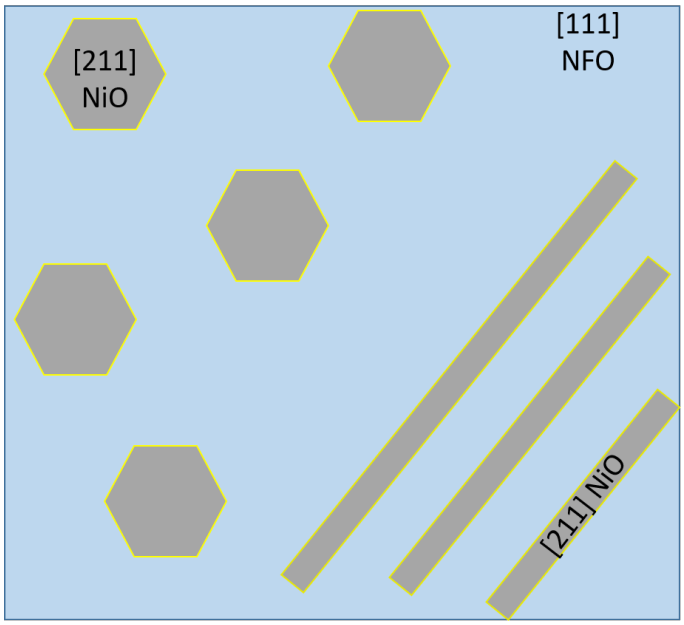

Figure 5.11. The arrangement of the naturally assembled NiO columns in the $NiFe_2O_4$ matrix.

In $NiFe_2O_4$, the tetrahedral Fe^{3+} ions are coupled antiferromagnetically with the octahedral Fe^{3+} and Ni^{2+} ions, leading to a collinear ferrimagnetic order with an easy axis along the [111] direction. On the other hand, NiO is an antiferromagnet with $T_N \sim 525$ K [137, 138, 144], as demonstrated by the temperature dependence of magnetic susceptibility in Figure 5.12. In its A-type antiferromagnetic structure, the {111} planes with ferromagnetically locked Ni^{2+} ions are strongly coupled antiferromagnetically. Due to the presence of the antiferromagnetic columns within the ferrimagnetic matrix, large local magnetic anisotropies can be expected.

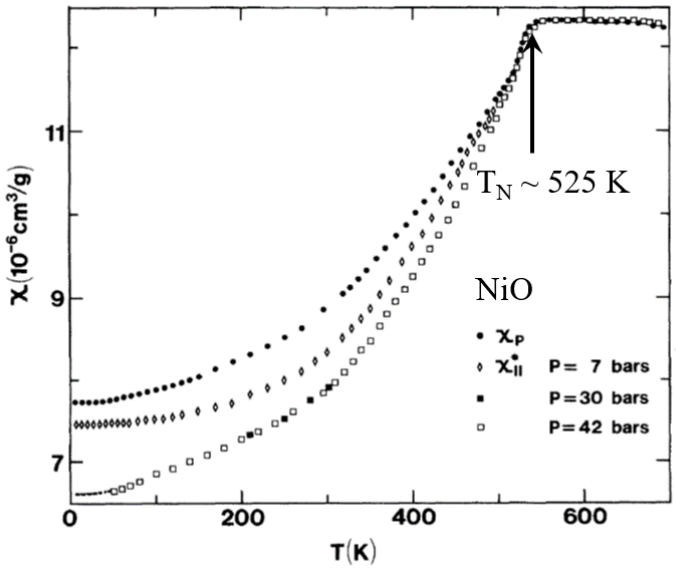

Figure 5.12. Temperature dependence of magnetic susceptibility in NiO. Figure adapted from Ref. [144].

To map the local magnetic anisotropy, we performed magnetic force microscopic (MFM) studies. The MFM phase contrast images were collected in a dual pass mode after the first pass topography scan. Figures 5.13(a and b) show the AFM image of a ∼12 μm by ∼16 μm region containing a vertical NiO column (dark blue area) and a line profile across the column, respectively. The MFM phase contrast images collected in the dual pass mode at T = 305 K from the same region are displayed in Figures 5.13(c–g). The blue and red phase contrast represent the domains aligned along the magnetic field ("up") and against the magnetic field ("down"), respectively. The MFM images show the distinct magnetic orders in the two regions, even when there is no magnetic field applied. At H = 0, $NiFe_2O_4$ consists of almost evenly distributed "up" and "down" regions, whereas NiO lacks any phase contrast. When the magnetic field is increased to 250 Oe, the contrasts in both regions are enhanced. Interestingly, the area around the NiO column starts to develop a phase opposite to that within the column. At H = 500 Oe, the NiO column is mostly saturated and the opposite contrast in the boundary region begins propagating across the $NiFe_2O_4$ matrix. At an even higher field, both NiO and $NiFe_2O_4$ regions are fully saturated,

with only the phase contrast between them remaining. Similar behavior is observed at low temperatures (T = 25 K), as shown in Figures 5.13(h–l). The MFM images verify the distinct magnetic orders in NiO and $NiFe_2O_4$ and illustrate the highly anisotropic local magnetism resulting from their coexistence.

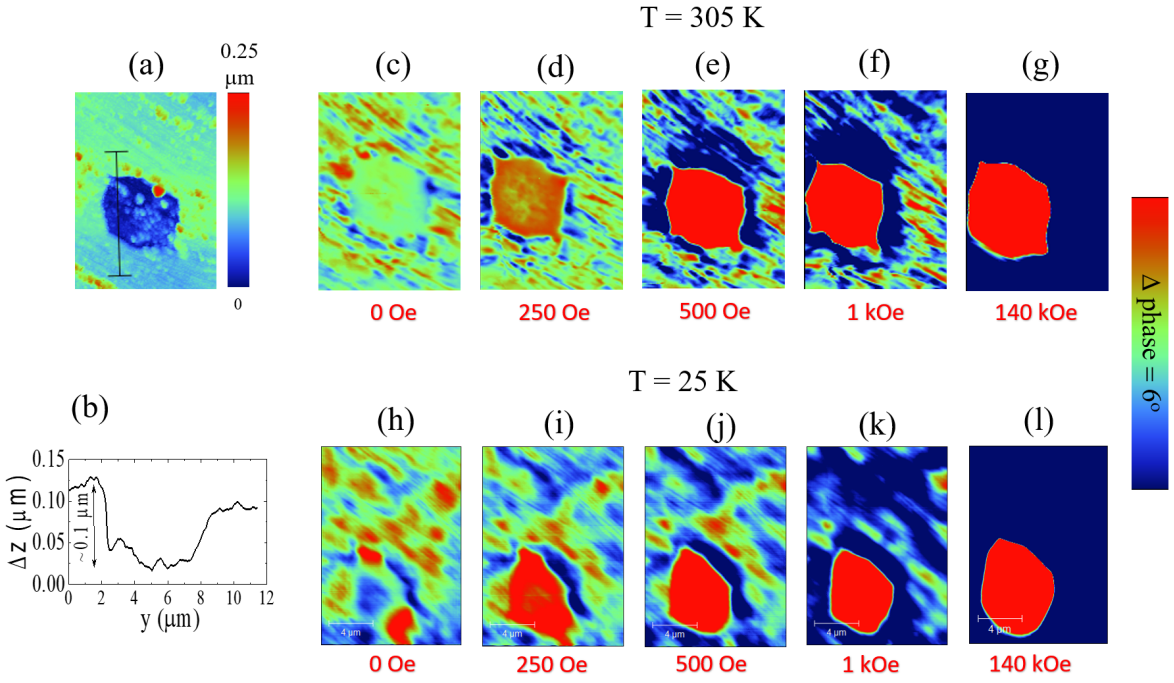

Figure 5.13. Magnetic force microscopy (MFM) of $NiFe_2O_4$ crystal C2. (a) AFM topographical image of an area of a polished single crystal containing a NiO column. (b) The line profile across the NiO column as indicated in (a). (c-g) MFM phase contrast images obtained at 305 K from the same region as (a) in a 100 nm lift height dual pass mode with magnetic fields 0 T to -14 T as indicated. (h-l) Same as (c-g) but obtained at 25 K. The scan area is ∼12 μm by ∼16 μm.

Our microscopic investigations demonstrate that the crystal C2 is composed of a self-assembled array of NiO columns within the matrix of $NiFe_2O_4$. The columns and the matrix are chemically, structurally, and magnetically distinct, as shown in Figure 5.14. Such arrangement leads to a disordered or frustrated region across the interface, where the spins experience a tug of war between the two distinct magnetic textures in the two regions. The disorder/frustration is further enhanced by the structural imperfection and cation intermixing at the interface. The spin disorder or frustration can result in a spin glass

(SG) state at the interface [134, 145, 146], manifesting in a drop in magnetic susceptibility below a freezing temperature, where the spins collectively freeze. Could the anomalous downturn in magnetic susceptibility in our samples be due to the interfacial SG state? To answer this question, we explored the usual signatures of SGs in sample C2.

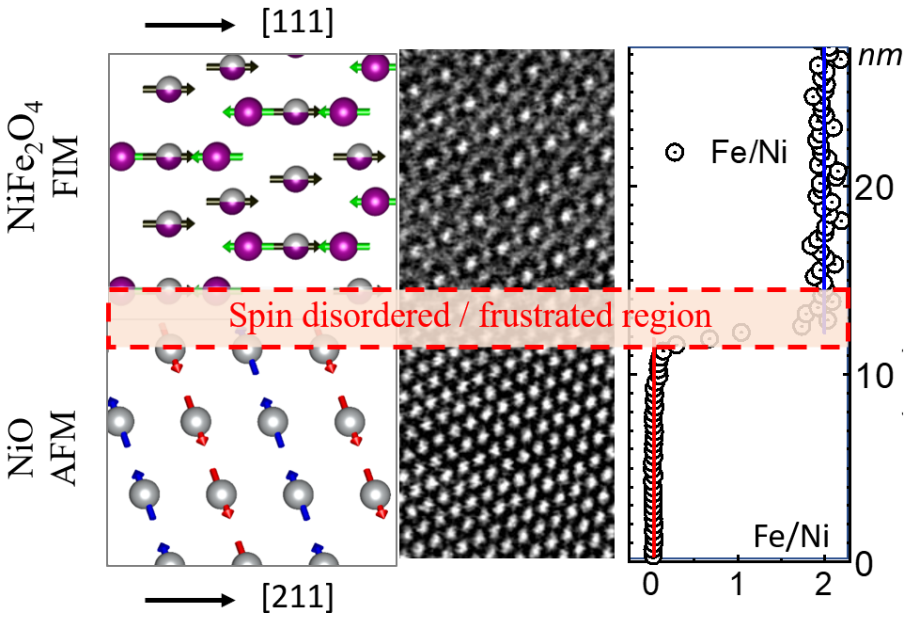

Figure 5.14. Spin arrangement, atomic arrangement, and chemical composition across the interface between $NiFe_2O_4$ and NiO with the spin disordered/frustrated interfacial region highlighted.

Figure 5.15(a) shows the temperature variations of the ZFC susceptibilities measured under selected magnetic fields below 50 K, where spin freezing can be observed at all fields. Notably, the magnetic field suppresses the freezing temperature T_f as well as the magnitude of the suppression. This behavior is in accord with that expected in a SG system, where a metastable frozen state observed below a well-defined freezing temperature T_f is suppressed by increasing field [10, 116]. The suppression of T_f by H results in a phase boundary between the glassy phase and the non-glassy phase, known as de Almeida-Thouless (AT) line [10, 147]. The AT line is described by the relationship $H = \alpha_{AT}[1 - (T_f(H)/T_{SG})]^{3/2}$, where the coefficient α_{AT} is a function of the exchange parameters and T_{SG} is the SG transition temperature as H approaches 0. Figure 5.15(b) shows the field dependence of

T_f. A linear dependence of T_f on $H^{2/3}$ demonstrates the existence of the AT line in our system. From the linear fit, we obtained $T_{SG} \sim 28$ K and $\alpha_{AT} \sim 10000$ Oe. The small value of α_{AT} suggests that this spin glass state is easily suppressed to 0 K by a moderate magnetic field.

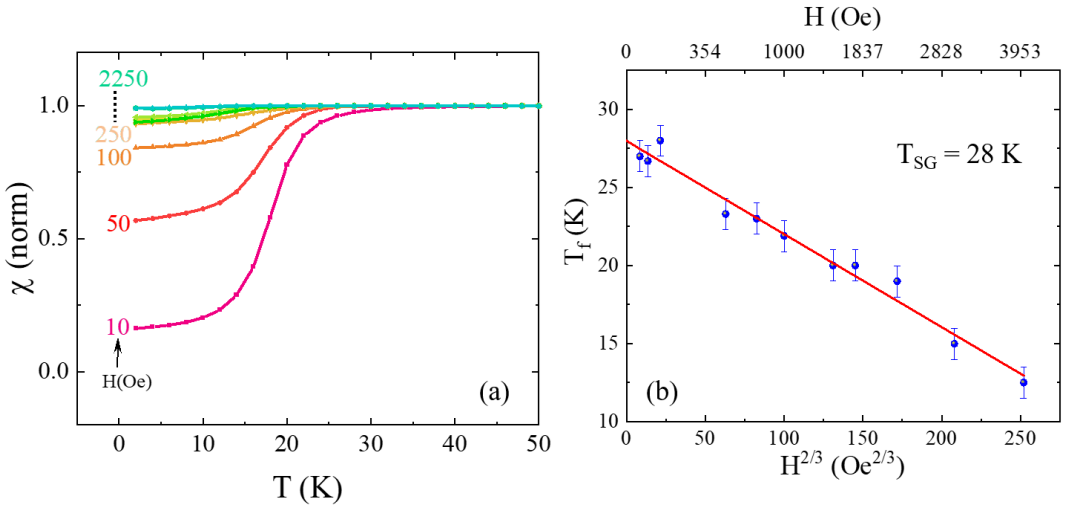

Figure 5.15. Magnetic field effect on spin freezing. (a) Temperature dependence of magnetic susceptibility in crystal C2 from 2 K to 50 K measured under indicated magnetic fields (H). (b) Freezing temperature T_f as a function of $H^{2/3}$. The solid line represents the best linear fit corresponding to de Almeida-Thouless relationship.

One of the signatures of SG is the presence of nonequilibrium phenomena due to the slow dynamics which prevents the system from reaching the equilibrium state within the time scale of an experiment [116, 148, 149]. To demonstrate the presence of the nonequilibrium dynamics, we carried out a series of dynamic magnetization measurements in both ZFC and FC conditions. Following the usual protocols [150], in the ZFC experiments, the ZFC_{stop} magnetization data were collected in the conventional procedure in the warming mode in the presence of a H = 50 Oe with intermediate stops at three temperatures for durations of one hour each. Figure 5.16(a) shows the ZFC_{stop} data overlaid with the usual ZFC and FC magnetization data for comparison, where the arrows represent the temperatures where the warming was temporarily halted. This time evolution of magnetization at each stop resulting in a step-like nature of the overall curve illustrates the nonequilibrium

dynamics in the system. Another example of nonequilibrium dynamics in SG system is the magnetic memory effect. Figure 5.16(b) shows the results of the FC magnetic memory effect experiments. In the first step, the FCC_{stop} magnetization is measured while cooling the sample to 2 K in 50 Oe magnetic field with three intermediate stops. During each stop, the magnetic field is turned off, and the magnetization is allowed to relax. After each stop, the magnetic field is turned back on, and the cooling is resumed. Once the sample is cooled to 2 K, the FCW_{mem} magnetization (memory curve) is measured while warming the sample continuously without any stops. As shown in Figure 5.16(b), clear features can be observed in the memory curve at temperatures where the cooling was paused, demonstrating the magnetic memory effect in the sample. The inset of Figure 5.16(b) further highlights this phenomenon.

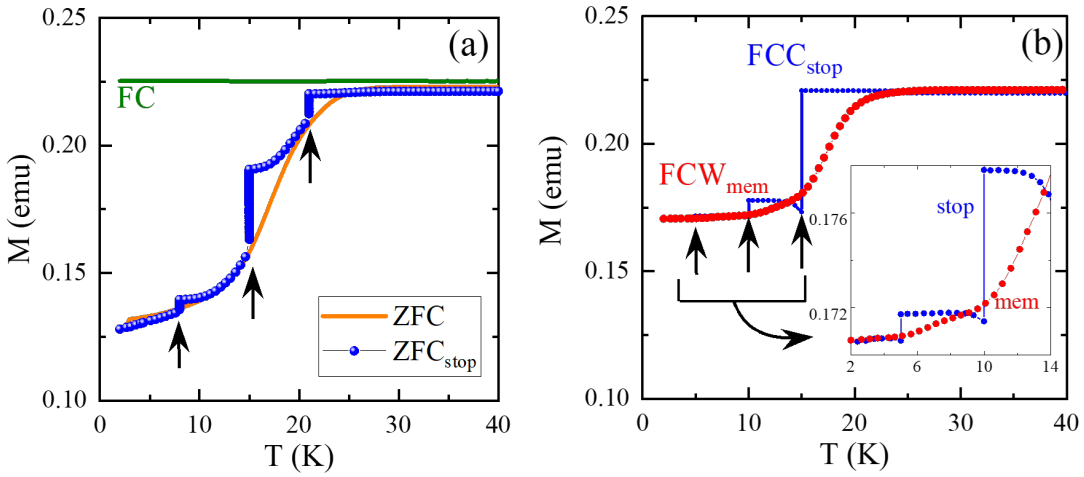

Figure 5.16. Memory effect in (a) ZFC and (b) FC dc magnetization in crystal C2. The arrows indicate the temperatures where the measurement was paused. The inset in (b) highlights the behavior below 14 K.

Further illustration of the magnetic memory effect can be observed in the ZFC and FC magnetization relaxation curves. Figure 5.17(a) shows the magnetization relaxation under the ZFC protocol, where the sample was first cooled down to T = 15 K under zero field, after which H = 50 Oe was turned on, and the time dependence of magnetization M(t) was measured for t_1 = 1 h. A clear exponential rise in M(t) can be observed during t_1. After t_1, the sample was quenched to T = 10 K and M(t) was measured for t_2 = 1

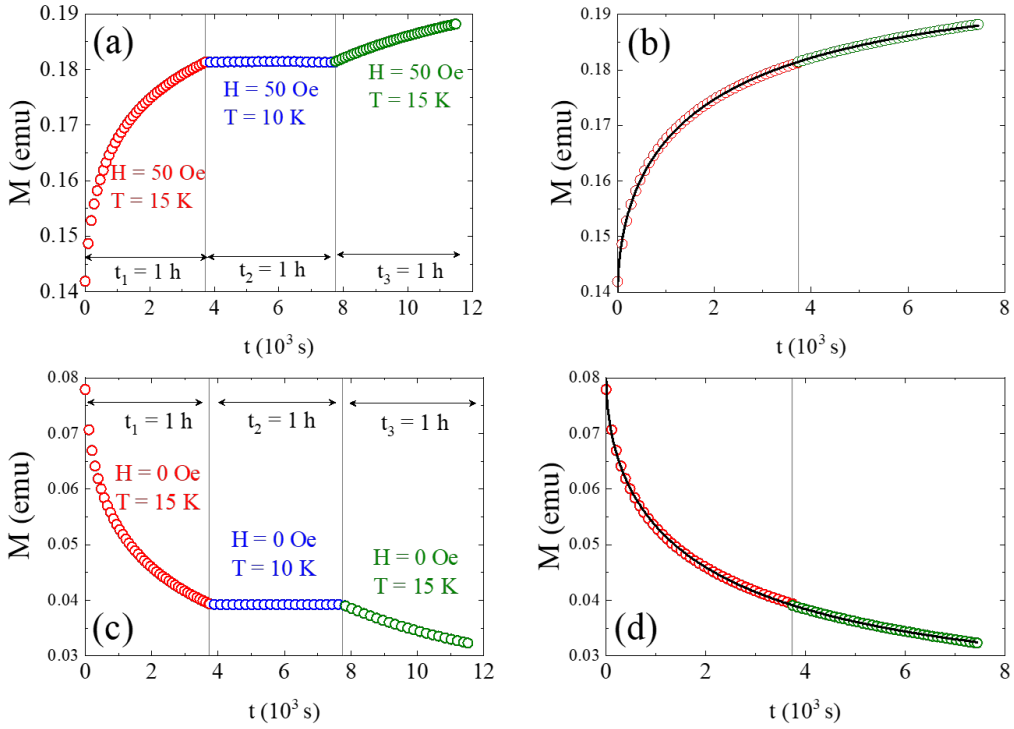

Figure 5.17. Magnetic memory effect in negative temperature cycling. (a) Relaxation of ZFC magnetization at 15 K measured in 50 Oe magnetic field with an intermediate negative temperature cycling though 10 K. (b) Data from duration t_1 and t_3 in (a) plotted after removing the points during t_2. (c) Relaxation of FC magnetization measured at 15 K in 0 Oe magnetic field with an intermediate negative temperature cycling through 10 K. (d) Data from duration t_1 and t_3 in (c) plotted together. The solid curves in (b) and (d) are the best fits to the stretched exponential model.

h. During t_2, the magnetization was found to be almost unchanged. Finally, the sample was warmed back to T = 15 K and M(t) was measured for t_3 = 1 h, where M(t) shows an exponential variation once again. In the FC protocol, shown in Figure 5.17(c), the sample was cooled to 15 K under H = 50 Oe. After reaching 15 K, the field was turned off and M(t) was measured for t_1 = 1 h, where an exponential relaxation is observed. The sample was then quenched to 10 K and kept there for t_2 = 1 h. Once again, M remains unchanged during t_2. After t_2, the sample was warmed back to 15 K, where M(t) starts to decrease exponentially. Remarkably, as shown in Figures 5.17(b and d), when the M(t)

data at 15 K measured during t_1 and t_3 are put together, they seem to follow a continuous exponential decay and growth for the FC and ZFC processes, respectively. This clearly indicates that the magnetic state of the system before temporary cooling is recovered after the temperature cycling. The solid green lines in Figures 5.17(b and d) are the best fits to the stretched exponential function $M(t) = M_0 + M_r exp[-(t/\tau)^{1-n}]$, where M_0 and M_r are the time-independent and glassy components of magnetization, respectively, and τ and n are the characteristic time constant and the critical exponent, respectively [151]. From the fitted curves, we obtain $n \sim 0.47$ and $\tau \sim 2000$ s for both FC and ZFC relaxation, comparable to those in some typical spin glass systems.

Interestingly, the magnetization relaxation curve could not be recovered in the case where the sample was subjected to an intermediate warming. Figure 5.18(a) shows the magnetization relaxation data measured at 15 K with an intermediate warming to 20 K. Like before, the sample was cooled to 15 K under a zero magnetic field, and the magnetization relaxation was measured under a 50 Oe magnetic field. After time period t_1, the sample was warmed to 20 K, where the magnetization continued to rise and failed to return to the previous state when cooled back to 15 K after t_2. This asymmetric response to negative and positive temperature cycling, i.e. temporary cooling and temporary warming, can be explained by the so-called hierarchical model [152–156]. In this description of SG, the free-energy landscape consists of fractal-like multivalley structure, as shown in Figure 5.18(b), which is a function of temperature. At a given temperature T_0, several valleys (local minima) that are metastable states are present out of which the system is "frozen" in one valley. When the system is quenched to a lower temperature $T_0 - \Delta T$, the valleys split into smaller sub-valleys that are separated by some energy barrier. At this lower temperature, the magnetization relaxation only occurs within one of the newly formed sub-valleys. When the system is brought back to the original temperature T_0, the sub-valleys merge and the system returns to the original state. On the other hand, if the sample is heated from T_0 to $T_0 + \Delta T$, the system gets out of the valley in which it was "frozen" and the

relaxation restarts in a new energy landscape. When the temperature is cooled back to T_0, the system cannot return to the valley it was originally trapped in because of several equally probable macrostates available. Thus, the memory effect can only be observed in the negative temperature cycling case.

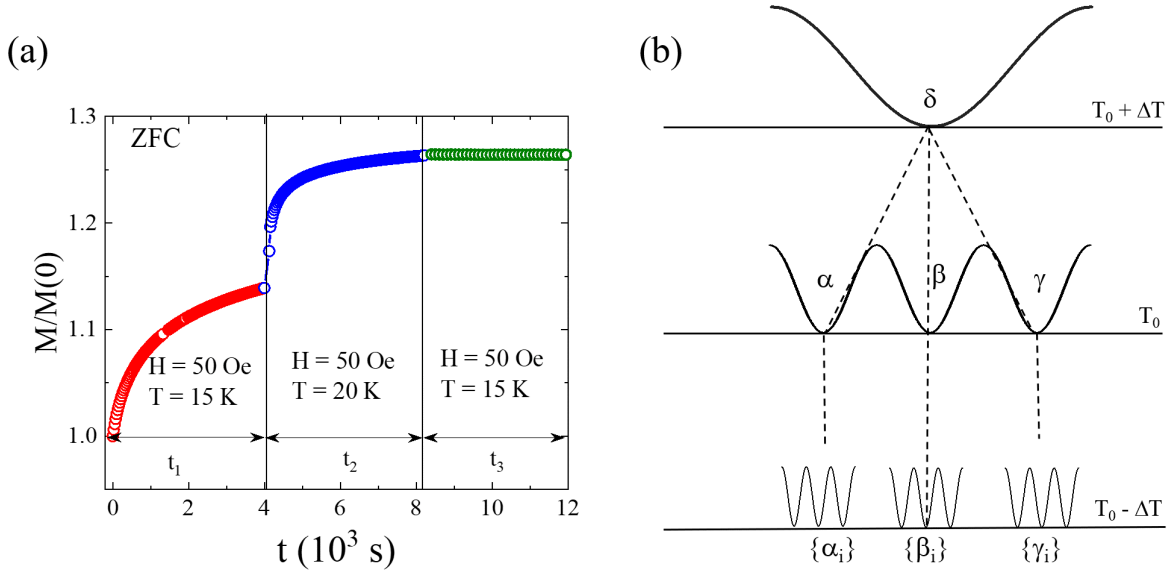

Figure 5.18. Positive temperature cycling of magnetization relaxation. (a) ZFC magnetization relaxation measured under 50 Oe at 15 K with an intermediate warming to 20 K during t_3. (b) A sketch of the fractal-like free energy landscape in the hierarchical model at different temperatures around T_0. Panel (b) reproduced from [153].

The glassy dynamics were further verified via ac susceptibility measurements. Figures 5.19(a and b) show the temperature dependences of the real χ' and imaginary χ'' parts of ac susceptibilities, respectively, measured under $H_{dc} = 0$ and $H_{ac} = 3.9$ Oe with various driving frequencies *f*. Both χ' and χ'' show prominent frequency dependences in the vicinity of spin freezing temperature. The downturn in χ' resembles to what was seen in dc magnetization measurements, whereas χ'' features a sharp peak near the freezing temperature. The freezing temperature T_f, defined here as the right inflection point in $\chi''(T)$ curve, increases with increasing *f*. Our experimental data show that T_f and *f* follow the Vogel-Fulcher law $f = f_0 e^{-E_a/(k_B(T_f - T_0))}$, where $\tau_0 = 1/f_0$ is the single spin flip time, E_a is the activation energy of the relaxation barrier, and T_0 is the Vogel-Fulcher temperature

[157–161], as shown by the linear scaling of $\ln(f)$ with $1/(T_f–T_0)$ in Figure 5.19(c). From the best fit line, we obtained $\tau_0 \sim 1{\cdot}10^{-6}$ s, $E_a \sim 33$ meV, and $T_0 \sim 4$ K. The spin flip time of $1{\cdot}10^{-6}$ is much longer than what is observed in the conventional spin glasses (10^{-10}–10^{-13} s) and lies on the upper end of the range observed in the cluster-type spin glasses with weak interactions (10^{-6}–10^{-10} s). The large activation energy $E_a \gg k_B T_0$ also suggests weak interactions between spin clusters.

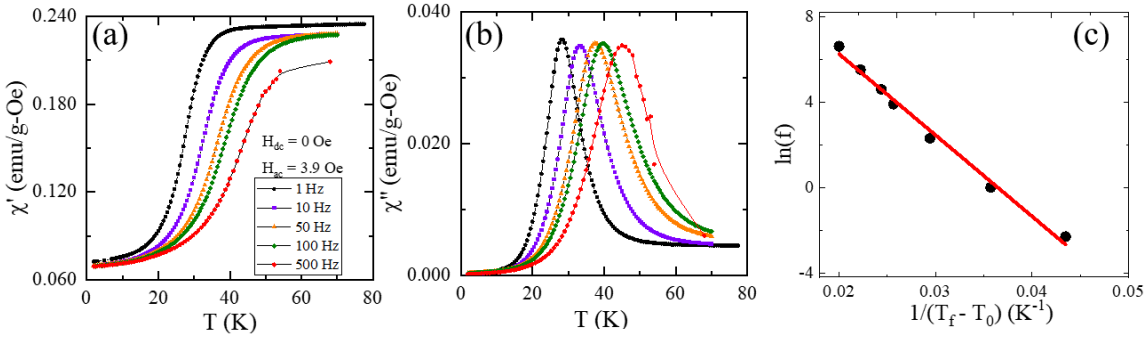

Figure 5.19. Ac magnetic susceptibility in $NiFe_2O_4$ crystal C2. (a and b) Temperature dependences of real and imaginary parts of ac susceptibility, respectively, measured under $H_{dc} = 0$ and $H_{ac} = 3.9$ Oe with indicated driving frequencies. (c) Frequency dependence of T_f. The solid line represents the fitting to the Vogel-Fulcher law.

From the ac and dc magnetic susceptibility measurements discussed above, we confirmed the presence of a SG state below $T_{SG} \sim 28$ K in sample C2. Because of the coexistence of the two highly anisotropic magnetic textures (FI and AFM), the spins at the interface are forced to satisfy both spin arrangements. The inability of the interfacial spins to satisfy both magnetic orders simultaneously results in a spin frustrated region at the interface. At high temperatures ($T \gg T_{SG}$), thermal fluctuations dominate over other requirements, allowing the frustrated spins to behave independently. The frustrated spins can freely rotate and can satisfy one or the other spin arrangements irrespective of the neighboring spins at the interface. As the temperature is lowered ($T \sim T_{SG}$), the independent spins slow down and start sensing the neighboring spins. The spins build up into locally correlated units, known as spin clusters [6]. The spins within a cluster fluctuate together. The spins that are not in clusters can take part in interactions between the clusters

[6]. Further lowering the temperature further slows the fluctuations within the cluster and at the same time, the clusters begin to grow. At T_{SG}, the system finds one of the many metastable ground states and the spins collectively "freeze" in that configuration. This freezing process is summarized in Figure 5.20.

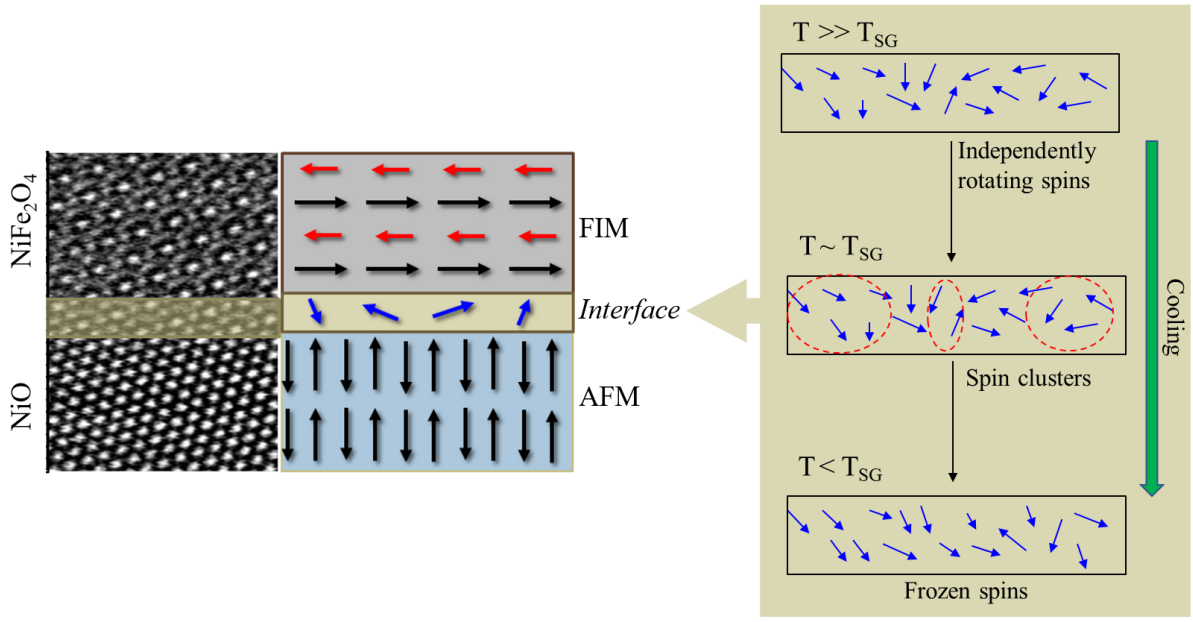

Figure 5.20. The spin frustrated interface between the ferrimagnetic $NiFe_2O_4$ and antiferromagnetic NiO. The spin freezing process is highlighted on the right panel.

The presence of the naturally assembled secondary rock-salt phase in the spinel matrix begs the question: what causes it? As mentioned earlier, the spinel structure and rock-salt structure are closely related. Several materials such as $LiMn_2O_4$ and $MgMn_2O_4$ undergo a phase transition from the spinel phase to a rock-salt phase where the tetrahedral cations diffuse in to the vacant 16c octahedral sites [142, 143, 162]. The presence of point defects, such as Frenkel-defect or vacancies, help overcome the energy barrier of diffusion which leads to the cation migration and a subsequent lattice reconstruction of the spinel structure to the rock-salt structure. While the exact reason for the formation of such naturally assembled rock-salt microstructures in our samples is not clear at this moment, our results show that the crystal growth atmosphere is an important factor. As implied by our measurements, the sample grown under 1 MPa oxygen pressure atmosphere (C1) contained a lesser amount of

rock-salt inclusions than the sample grown in a flowing oxygen atmosphere (C2). Therefore, oxygen vacancies during the crystal growth could have played a role in the nucleation of the rock-salt phase. This agrees with the previous reports that have shown that the oxygen vacancies can reduce the diffusion barrier needed for the phase reconstruction from spinel to rock-salt phases [142, 163, 164], and underscores the possibility of tuning the oxygen atmosphere to carefully produce materials with such natural microstructures. In addition to allowing us to investigate the interface phenomena, these natural microstructures could also be a new avenue to achieve complex magnetic structures, such as skyrmions and target skyrmions, due to their confined geometries [165–168]. The traditional method of artificially creating confined geometries from a large sample can be quite technical and expensive. The realization of naturally formed arrays of self-assembled microstructures provides an efficient and cheaper alternative.

5.3 Conclusion

In this chapter, we have demonstrated the emergence of new phenomena by exploiting the interfaces between the single crystal matrix $NiFe_2O_4$ containing self-assembled NiO columns that are uniformly distributed across the entire volume of the sample. From detailed SEM and high resolution STEM investigations, we determined that the NiO columns prefer to grow along the [211] crystallographic direction and are oriented either along the [111] direction of $NiFe_2O_4$ (vertical columns) or parallel to that direction (horizontal columns). The coexistence of two structurally (STEM images), chemically (EELS mapping), and magnetically (MFM images) distinct phases result in a highly spin frustrated interface. The frustrated interfacial spins undergo a collective freezing below $T_{SG} \sim 28$ K forming a spin glass state, which was verified via bulk magnetization measurements, including magnetic memory effect, dynamic magnetization, and frequency dependent ac susceptibility. Additionally, by varying the crystal growth conditions, we discovered that the nucleation of the columns is related to the crystal growth atmosphere; oxygen pressure dampenend their formation suggesting that the tuning of sample growth environment

could provide a feasible way to control such self-assembled columns. Such naturally arranged microstructures could provide a novel path to exploit interface-related phenomena and generate novel functionalities in a more cost-effective way.

Chapter 6
Summary

In this dissertation, we focused on the experimental investigation of complex magnetic phenomena in three iron-based spinel oxide systems: $FeMn_2O_4$, $MnFe_2O_4$, and $NiFe_2O_4$. We combined various in-house techniques at our disposal such as optical floating zone furnace, physical properties measurement system, magnetic properties measurement system, and magnetic force microscope with resources at two different national laboratories: Oak Rigde National Laboratory for neutron diffraction and Brookhaven National Laboratory for transmission electron microscopy. This allowed us to obtain a clear understanding of the magnetic landscape present in the three systems that we studied. The work presented in this dissertation is pictorially summarized in the Figure 6.1.

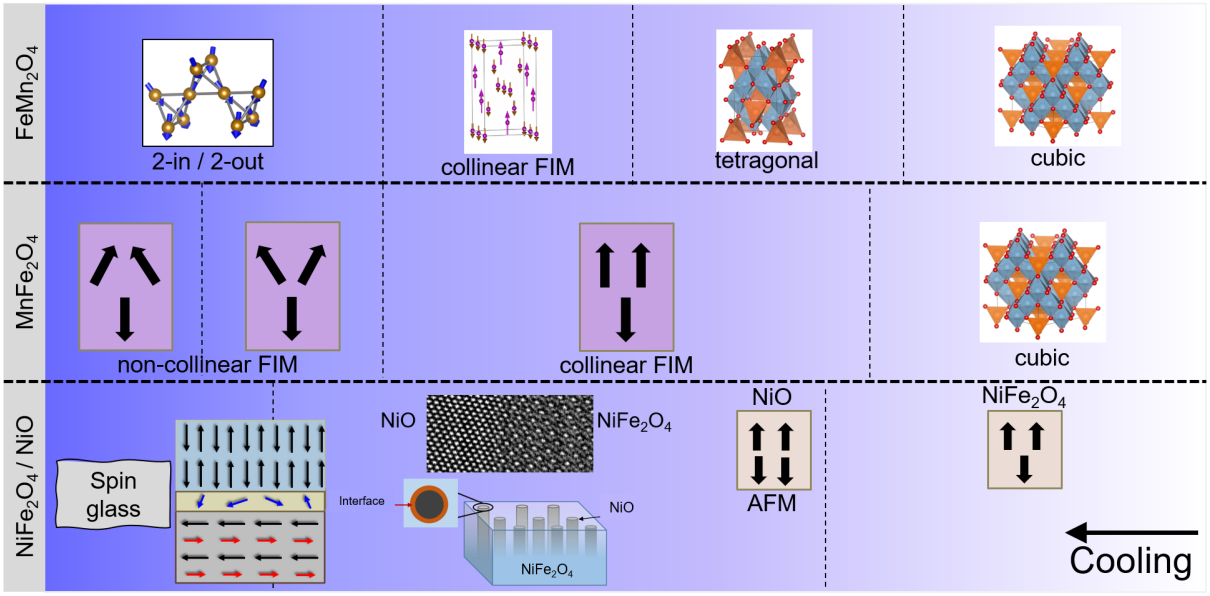

Figure 6.1. A summary of the results from this dissertation.

By investigating the structural, magnetic, thermal, and electrical properties of single-crystal $FeMn_2O_4$ in a wide range of temperature, we were able to identify three phase transitions. Through neutron powder diffraction measurement, we found that it undergoes a structural transition at $T_s \sim 595$ K from cubic at high temepratures to tetragonal at low temperatures. The other two transitions are magnetic transitions at $T_{FI\text{-}1} \sim 373$ K and $T_{FI\text{-}2}$

$\sim$ 50 K. Through magnetization and neutron diffraction measurements, we determined that $FeMn_2O_4$ orders ferrimagnetically below $T_{FI\text{-}1}$ with spins at the O-sublattice being antiparallel to those at the T-sublattice. On the other hand, below $T_{FI\text{-}2}$ the spins at the O-sublattice become noncollinear and order in a two-in-two-out fashion following the ice rules, resulting in a sharp decrease in the magnetization. Further investigation of its physical properties revealed significant contributions of magnetic excitations on low temperature specific heat and thermal conductivity and a very small phonon heat conduction.

A similar complex magnetic phase diagram was obtained in the case of $MnFe_2O_4$, with three different magnetic states emerging at $T_{FI\text{-}1} \sim 575$ K, $T_{FI\text{-}2} \sim 50$ K, and $T_x \sim 15$ K, respectively. It enters the collinear ferrimagnetic state from a high temperature paramagnetic state at $T_{FI\text{-}1}$ and undergoes two successive spin rearrangements at $T_{FI\text{-}2}$ and T_x. Our detailed analyses of the specific heat and thermal conductivity measurements revealed a significant contribution from the low-temperature magnetic excitations. We found that a large negative magneto-thermal conductivity emerges below $\sim 2T_{FI\text{-}2}$ with a maximum amplitude near $T_{FI\text{-}2}$, which becomes positive below T_x. Such opposite response to the magnetic field in the two low temperature magnetic states demonstrate their different spin configurations.

In the third part of this dissertation, we investigated the complexities that arise at the interface of two magnetically different materials. We executed bulk magnetic and microscopic measurements of single crystalline $NiFe_2O_4$ with a self-assembled array of NiO columns. Our magnetization measurements showed the presence of a low temperature spin glass state below $T_{SG} \sim 28$ K with magnetic memory effect and slow spin dynamics. MFM revealed large local magnetic anisotropy from the presence of the microstructures within the ferrimagnetic matrix. Our results showed that the spin glass state forms at the interface between the two phases due to the competing magnetic orders across the interface. Our work shows that the self-assembled array of microstructures embedded within a crystalline matrix could provide a new path to exploit interfaces for practical applications.

Appendix. Consent Policy

American Physical Society Reuse and Permissions License

03-Mar-2020

This license agreement between the American Physical Society ("APS") and Roshan Nepal ("You") consists of your license details and the terms and conditions provided by the American Physical Society and SciPris.

Licensed Content Information

License Number:	**RNP/20/MAR/023355**
License date:	03-Mar-2020
DOI:	10.1103/PhysRevB.97.024410
Title:	Structural and magnetic transitions in spinel $\mathrm{FeM}{\mathrm{n}}_{2}{\mathrm{O}}_{4}$ single crystals
Author:	Roshan Nepal et al.
Publication:	Physical Review B
Publisher:	American Physical Society
Cost:	USD $ 0.00

Request Details

Does your reuse require significant modifications: No

Specify intended distribution locations:	United States
Reuse Category:	Reuse in a thesis/dissertation
Requestor Type:	Author of requested content
Items for Reuse:	Whole Article
Format for Reuse:	Electronic

Information about New Publication:

University/Publisher:	Louisiana State University
Title of dissertation/thesis:	Investigation of complex magnetic phenomena in spinel FeMn2O4, MnFe2O4, and NiFe2O4
Author(s):	Roshan Nepal
Expected completion date:	May. 2020

License Requestor Information

Name:	Roshan Nepal
Affiliation:	Individual
Email Id:	rnepal3@lsu.edu
Country:	United States

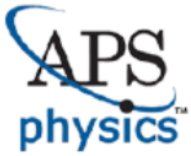

American Physical Society
Reuse and Permissions License

TERMS AND CONDITIONS

The American Physical Society (APS) is pleased to grant the Requestor of this license a non-exclusive, non-transferable permission, limited to Electronic format, provided all criteria outlined below are followed.

1. You must also obtain permission from at least one of the lead authors for each separate work, if you haven't done so already. The author's name and affiliation can be found on the first page of the published Article.

2. For electronic format permissions, Requestor agrees to provide a hyperlink from the reprinted APS material using the source material's DOI on the web page where the work appears. The hyperlink should use the standard DOI resolution URL, http://dx.doi.org/{DOI}. The hyperlink may be embedded in the copyright credit line.

3. For print format permissions, Requestor agrees to print the required copyright credit line on the first page where the material appears: "Reprinted (abstract/excerpt/figure) with permission from [(FULL REFERENCE CITATION) as follows: Author's Names, APS Journal Title, Volume Number, Page Number and Year of Publication.] Copyright (YEAR) by the American Physical Society."

4. Permission granted in this license is for a one-time use and does not include permission for any future editions, updates, databases, formats or other matters. Permission must be sought for any additional use.

5. Use of the material does not and must not imply any endorsement by APS.

6. APS does not imply, purport or intend to grant permission to reuse materials to which it does not hold copyright. It is the requestor's sole responsibility to ensure the licensed material is original to APS and does not contain the copyright of another entity, and that the copyright notice of the figure, photograph, cover or table does not indicate it was reprinted by APS with permission from another source.

7. The permission granted herein is personal to the Requestor for the use specified and is not transferable or assignable without express written permission of APS. This license may not be amended except in writing by APS.

8. You may not alter, edit or modify the material in any manner.

9. You may translate the materials only when translation rights have been granted.

10. APS is not responsible for any errors or omissions due to translation.

11. You may not use the material for promotional, sales, advertising or marketing purposes.

12. The foregoing license shall not take effect unless and until APS or its agent, Aptara, receives payment in full in accordance with Aptara Billing and Payment Terms and Conditions, which are incorporated herein by reference.

13. Should the terms of this license be violated at any time, APS or Aptara may revoke the license with no refund to you and seek relief to the fullest extent of the laws of the USA. Official written notice will be made using the contact information provided with the permission request. Failure to receive such notice will not nullify revocation of the permission.

14. APS reserves all rights not specifically granted herein.

15. This document, including the Aptara Billing and Payment Terms and Conditions, shall be the entire agreement between the parties relating to the subject matter hereof.

Observation of three magnetic states in spinel MnFe2O4 single crystals

Author: Roshan Nepal,Mohammad Saghayezhian,Jiandi Zhang,Rongying Jin

Publication: Journal of Magnetism and Magnetic Materials

Publisher: Elsevier

Date: 1 March 2020

References

[1] C. Lacroix, P. Mendels, and F. Mila, eds., *Introduction to frustrated magnetism: materials, experiments, theory* (Springer Science & Business Media, 2011).

[2] C. Lhuillier and G. Misguich, in *Introduction to frustrated magnetism: materials, experiments, theory*, edited by C. Lacroix, P. Mendels, and F. Mila (Springer Science & Business Media, 2011) Chap. 2, pp. 23–39.

[3] C. Castelnovo, R. Moessner, and S. L. Sondhi, Nature **451**, 42–45 (2008).

[4] T. Kurumaji, T. Nakajima, M. Hirschberger, A. Kikkawa, Y. Yamasaki, H. Sagayama, H. Nakao, Y. Taguchi, T.-h. Arima, and Y. Tokura, Science **365**, 914–918 (2019).

[5] N. Grimes, Physics in Technology **6**, 22 (1975).

[6] S. Blundell, *Magnetism in condensed matter* (Oxford University Press, 2001).

[7] A. H. Morrish, *The physical principles of magnetism* (Wiley-IEEE Press, New York, 2001).

[8] H. A. Jahn and E. Teller, Proceedings of the Royal Society of London. Series A-Mathematical and Physical Sciences **161**, 220–235 (1937).

[9] M. L. Néel, in *Annales de Physique*, Vol. 3 (1948) p. 137.

[10] K. Binder and A. P. Young, Reviews of Modern physics **58**, 801 (1986).

[11] M. L. Néel, in *Annales de Physique*, Vol. 18 (1932) p. 5.

[12] M. L. Néel, in *Annales de Physique*, Vol. 5 (1936) p. 232.

[13] M. L. Néel, Proceedings of the Physical Society. Section A **65**, 869 (1952).

[14] D. C. Mattis, *The theory of magnetism made simple: an introduction to physical concepts and to some useful mathematical methods* (World Scientific Publishing Company, 2006).

[15] W. F. Giauque and M. F. Ashley, Physical Review **43**, 81 (1933).

[16] W. Giauque and J. Stout, Journal of the American Chemical Society **58**, 1144–1150 (1936).

[17] L. Pauling, Journal of the American Chemical Society **57**, 2680–2684 (1935).

[18] M. J. P. Gingras, in *Introduction to frustrated magnetism: materials, experiments, theory*, edited by C. Lacroix, P. Mendels, and F. Mila (Springer Science & Business Media, 2011) Chap. 12, pp. 293–329.

[19] R. J. Cava, K. L. Holman, T. McQueen, E. J. Welsh, D. V. West, and A. J. Williams, in *Introduction to frustrated magnetism: materials, experiments, theory*, edited by C. Lacroix, P. Mendels, and F. Mila (Springer Science & Business Media, 2011) Chap. 6, pp. 131–154.

[20] H. Takagi and S. Niitaka, in *Introduction to frustrated magnetism: materials, experiments, theory*, edited by C. Lacroix, P. Mendels, and F. Mila (Springer Science & Business Media, 2011) Chap. 7, pp. 155–175.

[21] R. Plumier and A. Tardieu, C.R. Acad. Sci. **257**, 3858 (1963).

[22] H. Mamiya and M. Onoda, Solid State Communications **95**, 217–221 (1995).

[23] H. Mamiya, M. Onoda, T. Furubayashi, J. Tang, and I. Nakatani, Journal of applied physics **81**, 5289–5291 (1997).

[24] S. Nizioł, Physica Status Solidi (a) **18**, K11–K13 (1973).

[25] Y. Ueda, N. Fujiwara, and H. Yasuoka, Journal of the Physical Society of Japan **66**, 778–783 (1997).

[26] S. Kondo, J. Phys. Soc. Jpn. **69**, 139 (2000).

[27] S.-H. Lee, D. Louca, H. Ueda, S. Park, T. Sato, M. Isobe, Y. Ueda, S. Rosenkranz, P. Zschack, J. Íñiguez, Y. Qiu, and R. Osborn, Physical Review Letters **93**, 156407 (2004).

[28] S.-H. Lee, C. Broholm, T. Kim, I. W Ratcliff, and S.-W. Cheong, Physical Review Letters **84**, 3718 (2000).

[29] K. Kamazawa, Y. Tsunoda, H. Kadowaki, and K. Kohn, Physical Review B **68**, 024412 (2003).

[30] K. Tomiyasu, J. Fukunaga, and H. Suzuki, Physical Review B **70**, 214434 (2004).

[31] Y. Yamasaki, S. Miyasaka, Y. Kaneko, J.-P. He, T. Arima, and Y. Tokura, Physical Review Letters **96**, 207204 (2006).

[32] N. Tristan, J. Hemberger, A. Krimmel, H.-A. Krug von Nidda, V. Tsurkan, and A. Loidl, Physical Review B **72**, 174404 (2005).

[33] T. Suzuki, H. Nagai, M. Nohara, and H. Takagi, Journal of Physics: Condensed Matter **19**, 145265 (2007).

[34] J. t. Dunitz and L. Orgel, Journal of Physics and Chemistry of Solids **3**, 318–323 (1957).

[35] D. S. McClure, Journal of Physics and Chemistry of Solids **3**, 311–317 (1957).

[36] R. G. Burns and R. G. Burns, *Mineralogical applications of crystal field theory*, Vol. 5 (Cambridge university press, 1993).

[37] S. E. Dutton, Q. Huang, O. Tchernyshyov, C. Broholm, and R. Cava, Physical Review B **83**, 064407 (2011).

[38] S. Bordács, D. Varjas, I. Kézsmárki, G. Mihály, L. Baldassarre, A. Abouelsayed, C. A. Kuntscher, K. Ohgushi, and Y. Tokura, Physical Review Letters **103**, 077205 (2009).

[39] M. C. Kemei, P. T. Barton, S. L. Moffitt, M. W. Gaultois, J. A. Kurzman, R. Seshadri, M. R. Suchomel, and Y.-I. Kim, Journal of Physics: Condensed Matter **25**, 326001 (2013).

[40] M. L. Néel, in *Annales de Physique*, Vol. 12 (1948) pp. 137–198.

[41] D. S. Mathew and R.-S. Juang, Chemical Engineering Journal **129**, 51–65 (2007).

[42] A. Elfalaky and S. Soliman, Journal of Alloys and Compounds **580**, 401–406 (2013).

[43] V. O. Garlea, R. Jin, D. Mandrus, B. Roessli, Q. Huang, M. Miller, A. J. Schultz, and S. E. Nagler, Physical Review Letters **100**, 066404 (2008).

[44] E. Winkler, S. B. Canosa, F. Rivadulla, M. López-Quintela, J. Rivas, A. Caneiro, M. Causa, and M. Tovar, Physical Review B **80**, 104418 (2009).

[45] Y. Murakami, Y. Nii, T. Arima, D. Shindo, K. Yanagisawa, and A. Tonomura, Physical Review B **84**, 054421 (2011).

[46] Q. Zhang, K. Singh, F. Guillou, C. Simon, Y. Breard, V. Caignaert, and V. Hardy, Physical Review B **85**, 054405 (2012).

[47] G. Srinivasan and M. S. Seehra, Physical Review B **28**, 1 (1983).

[48] M. Kim, X. Chen, Y. I. Joe, E. Fradkin, P. Abbamonte, and S. L. Cooper, Physical Review Letters **104**, 136402 (2010).

[49] T. Tatarchuk, M. Bououdina, J. J. Vijaya, and L. J. Kennedy, in *International Conference on Nanotechnology and Nanomaterials* (Springer, 2016) pp. 305–325.

[50] N. M. Caffrey, D. Fritsch, T. Archer, S. Sanvito, and C. Ederer, Physical Review B **87**, 024419 (2013).

[51] C. S. Hurlbut, E. S. Dana, and W. E. Sharp, *Dana's Minerals and How to Study Them (After Edward Salisbury Dana)* (John Wiley & Sons, 1998).

[52] P. Wasilewski and G. Kletetschka, Geophysical Research Letters **26**, 2275–2278 (1999).

[53] F. Walz, Journal of Physics: Condensed Matter **14**, R285 (2002).

[54] L. Martín-García, A. Mascaraque, B. M. Pabón, R. Bliem, G. S. Parkinson, G. Chen, A. K. Schmid, J. de la Figuera, *et al.*, Physical Review B **93**, 134419 (2016).

[55] H. A. Dabkowska and A. B. Dabkowski, in *Springer Handbook of Crystal Growth*, edited by G. Dhanaraj, K. Byrappa, V. Prasad, and M. Dudley.

[56] *Magnetic Property Measurement System: MPMS MultiVu Application User's Manual* (Quantum Design).

[57] *Vibrating Sample Magnetometer (VSM) Option User's Manual* (Quantum Design).

[58] D. Martien, "Introduction to ac susceptibility. quantum design," (2000).

[59] *Physical Property Measurement System: Heat Capacity Option User's Manual* (Quantum Design).

[60] *Physical Property Measurement System: Hardware Manual* (Quantum Design).

[61] *Physical Property Measurement System: Thermal Transport Option User's Manual* (Quantum Design).

[62] *Physical Property Measurement System: Resistivity Option User's Manual* (Quantum Design).

[63] Keithley, "Model 2001 multimeter: Operator's manual," (2010).

[64] D. B. Williams and C. B. Carter, in *Transmission electron microscopy* (Springer, 1996) pp. 3–17.

[65] C. Davisson and L. H. Germer, Physical Review **30**, 705 (1927).

[66] G. P. Thomson and A. Reid, Nature **119**, 890–890 (1927).

[67] U. Hartmann, Annual Review of Materials Science **29**, 53–87 (1999).

[68] attocube, "User manual: Atomic force microscope attoafm/mfm ixs," (2014).

[69] R. Buhl, Journal of Physics and Chemistry of Solids **30**, 805–812 (1969).

[70] V. Brabers, Physica Status Solidi (b) **33**, 563–572 (1969).

[71] P. J. Wojtowicz, Physical Review **116**, 32 (1959).

[72] G. I. Finch, A. Sinha, and K. Sinha, Proceedings of the Royal Society of London. Series A. Mathematical and Physical Sciences **242**, 28–35 (1957).

[73] B. Boucher, R. Buhl, and M. Perrin, Journal of Applied Physics **40**, 1126–1127 (1969).

[74] V. Brabers, Journal of Crystal Growth **8**, 26–28 (1971).

[75] V. Brabers, Journal of Physics and Chemistry of Solids **32**, 2181–2191 (1971).

[76] K. Naito, H. Inaba, and H. Yagi, Journal of Solid State Chemistry **36**, 28–35 (1981).

[77] R. Nepal, Q. Zhang, S. Dai, W. Tian, S. E. Nagler, and R. Jin, Physical Review B **97**, 024410 (2018).

[78] H. Lee, G. Kim, D. Kim, J. Kang, C. Zhang, S.-W. Cheong, J. H. Shim, S. Lee, H. Lee, J. Kim, *et al.*, Journal of Physics: Condensed Matter **20**, 295203 (2008).

[79] S. C. Tarantino, M. Giannini, M. A. Carpenter, and M. Zema, IUCrJ **3**, 354–366 (2016).

[80] S. Nayak, S. Thota, D. Joshi, M. Krautz, A. Waske, A. Behler, J. Eckert, T. Sarkar, M. S. Andersson, R. Mathieu, *et al.*, Physical Review B **92**, 214434 (2015).

[81] R. Bhowmik, R. Ranganathan, and R. Nagarajan, Physical Review B **73**, 144413 (2006).

[82] S. Thota and M. Seehra, Journal of Applied Physics **113**, 203905 (2013).

[83] M. Tanaka, T. Mizoguchi, and Y. Aiyama, Journal of the Physical Society of Japan **18**, 1091–1091 (1963).

[84] E. Gopal, *Specific heats at low temperatures* (Plenum Press, New York, 1966).

[85] R. Fisher, F. Bouquet, N. Phillips, J. Franck, G. Zhang, J. Gordon, and C. Marcenat, Physical Review B **64**, 134425 (2001).

[86] D. Villuendas, T. Tsutaoka, and J. H. Ferràs, Journal of Magnetism and Magnetic Materials **405**, 282–286 (2016).

[87] G. Balaji, N. Gajbhiye, G. Wilde, and J. Weissmüller, Journal of Magnetism and Magnetic Materials **242**, 617–620 (2002).

[88] K. Sinha and U. Upadhyaya, Physical Review **127**, 432 (1962).

[89] G. Dixon, Physical Review B **21**, 2851 (1980).

[90] V. Brabers, Y. Proykova, N. Salerno, and T. Whall, Journal of Applied Physics **61**, 4390–4392 (1987).

[91] D. Santos-Carballal, A. Roldan, R. Grau-Crespo, and N. H. De Leeuw, Physical Review B **91**, 195106 (2015).

[92] S. Harrison, C. Kriessman, and S. Pollack, Physical Review **110**, 844 (1958).

[93] J. M. Hastings and L. M. Corliss, Physical Review **104**, 328 (1956).

[94] G. Sawatzky, F. Van Der Woude, and A. Morrish, Physical Review **187**, 747 (1969).

[95] Z. Simsa and V. Brabers, IEEE Transactions on Magnetics **11**, 1303–1305 (1975).

[96] A. Heeger, T. Blocker III, and S. Ghosh, Journal of Applied Physics **35**, 840–841 (1964).

[97] B. Low, Journal of Applied Physics **34**, 1250–1251 (1963).

[98] A. B. Van Groenou, Journal of Physics and Chemistry of Solids **28**, 325–331 (1967).

[99] R. Nepal, M. Saghayezhian, J. Zhang, and R. Jin, Journal of Magnetism and Magnetic Materials **497**, 165955 (2020).

[100] B. Aslibeiki, P. Kameli, and M. Ehsani, Ceramics International **42**, 12789–12795 (2016).

[101] J. B. Goodenough and A. L. Loeb, Physical Review **98**, 391 (1955).

[102] Q. Zhao, Z. Yan, C. Chen, and J. Chen, Chemical Reviews **117**, 10121–10211 (2017).

[103] C. Shull, E. Wollan, and W. Koehler, Physical Review **84**, 912 (1951).

[104] Z. Šimša, Cechoslovackij Fiziceskij Zurnal B **15**, 435–437 (1965).

[105] Y. Huang, Z. Yang, and Y. Zhang, Journal of Physics: Condensed Matter **24**, 056003 (2012).

[106] D. Jiles, *Introduction to magnetism and magnetic materials* (CRC press, 2015).

[107] S. R. Butler and W. R. Buessem, Journal of Applied Physics **34**, 1754–1757 (1963).

[108] K. Mandal, S. Mitra, and P. A. Kumar, Europhysics Letters **75**, 618 (2006).

[109] R. Kodama, Journal of magnetism and magnetic materials **200**, 359–372 (1999).

[110] B. Mehdaoui, R. Moubah, B. Orayech, M. Bahout, O. Peña, M. Jáuregui, D. Saurel, and A. El Bouari, Journal of Alloys and Compounds **748**, 528–536 (2018).

[111] A. Franco Jr, H. Pessoni, and F. Machado, Journal of Applied Physics **118**, 173904 (2015).

[112] X. Zuo and C. Vittoria, Physical Review B **66**, 184420 (2002).

[113] Y. Yafet and C. Kittel, Physical Review **87**, 290 (1952).

[114] R. Jin, Y. Onose, Y. Tokura, D. Mandrus, P. Dai, and B. Sales, Physical Review Letters **91**, 146601 (2003).

[115] D. Sanders and D. Walton, Physical Review B **15**, 1489 (1977).

[116] J. A. Mydosh, *Spin glasses: an experimental introduction* (Taylor and Francis, London, 1993).

[117] J. Owen, M. Browne, W. Knight, and C. Kittel, Physical Review **102**, 1501 (1956).

[118] J. De Nobel and F. Du Chatenier, Physica **25**, 969–979 (1959).

[119] J. E. Zimmerman and F. Hoare, Journal of Physics and Chemistry of Solids **17**, 52–56 (1960).

[120] P. W. Anderson, Materials Research Bulletin **5**, 549–554 (1970).

[121] G. Parisi, Proceedings of the National Academy of Sciences **103**, 7948–7955 (2006).

[122] G. Venkataraman and G. Athithan, Pramana **36**, 1–77 (1991).

[123] A. Ansari, J. Berendzen, S. F. Bowne, H. Frauenfelder, I. Iben, T. B. Sauke, E. Shyamsunder, and R. D. Young, Proceedings of the National Academy of Sciences **82**, 5000–5004 (1985).

[124] J.-i. Inoue, Physical Review E **63**, 046114 (2001).

[125] L. Zhu, K. Ikeda, P. Pang, R. Zhang, and A. Sarrafzadeh, in *International Conference on Neural Information Processing* (Springer, 2016) pp. 579–586.

[126] J.-i. Maskawa, in *Empirical Science of Financial Fluctuations* (Springer, 2002) pp. 153–158.

[127] M. Ohzeki, in *Lectures on Quantum Computing, Thermodynamics and Statistical Physics* (World Scientific, 2013) pp. 63–124.

[128] P. W. Anderson, Physics Today **41**, 9–11 (1988).

[129] F. Hellman, A. Hoffmann, Y. Tserkovnyak, G. S. Beach, E. E. Fullerton, C. Leighton, A. H. MacDonald, D. C. Ralph, D. A. Arena, H. A. Dürr, *et al.*, Reviews of Modern Physics **89**, 025006 (2017).

[130] J. Chakhalian, J. W. Freeland, A. J. Millis, C. Panagopoulos, and J. M. Rondinelli, Reviews of Modern Physics **86**, 1189 (2014).

[131] H. Y. Hwang, Y. Iwasa, M. Kawasaki, B. Keimer, N. Nagaosa, and Y. Tokura, Nature Materials **11**, 103–113 (2012).

[132] J. Ding, O. Lebedev, S. Turner, Y. Tian, W. Hu, J. Seo, C. Panagopoulos, W. Prellier, G. Van Tendeloo, and T. Wu, Physical Review B **87**, 054428 (2013).

[133] H. Guo, Z. Wang, S. Dong, S. Ghosh, M. Saghayezhian, L. Chen, Y. Weng, A. Herklotz, T. Z. Ward, R. Jin, *et al.*, Proceedings of the National Academy of Sciences **114**, E5062–E5069 (2017).

[134] B. Pang, L. Zhang, Y. Chen, J. Zhou, S. Yao, S. Zhang, and Y. Chen, ACS Applied Materials & Interfaces **9**, 3201–3207 (2017).

[135] D. A. Gilbert, B. B. Maranville, A. L. Balk, B. J. Kirby, P. Fischer, D. T. Pierce, J. Unguris, J. A. Borchers, and K. Liu, Nature Communications **6**, 1–7 (2015).

[136] K. Ugendar, S. Samanta, S. Rayaprol, V. Siruguri, G. Markandeyulu, and B. Nanda, Physical Review B **96**, 035138 (2017).

[137] W. L. Roth and G. A. Slack, Journal of Applied Physics **31**, S352–S353 (1960).

[138] R. Shanker and R. Singh, Physical Review B **7**, 5000 (1973).

[139] A. C. Pebley, P. E. Fuks, T. M. Pollock, and M. J. Gordon, Journal of Magnetism and Magnetic Materials **419**, 29–36 (2016).

[140] B. Negulescu, L. Thomas, Y. Dumont, M. Tessier, N. Keller, and M. Guyot, Journal of Magnetism and Magnetic Materials **242**, 529–531 (2002).

[141] S. J. Schneider, *Compilation of the melting points of the metal oxides*, Vol. 63 (US Department of Commerce, National Bureau of Standards, 1963).

[142] P. Gao, R. Ishikawa, E. Tochigi, A. Kumamoto, N. Shibata, and Y. Ikuhara, Chemistry of Materials **29**, 1006–1013 (2017).

[143] Q. D. Truong, M. Kempaiah Devaraju, P. D. Tran, Y. Gambe, K. Nayuki, Y. Sasaki, and I. Honma, Chemistry of Materials **29**, 6245–6251 (2017).

[144] G. Srinivasan and M. S. Seehra, Physical Review B **29**, 6295 (1984).

[145] F. Spizzo, M. Tamisari, F. Chinni, E. Bonfiglioli, and L. Del Bianco, Journal of Magnetism and Magnetic Materials **421**, 234–240 (2017).

[146] F. Radu, *Fundamental aspects of exchange bias effect in AF/F bilayers and multilayers*, PhD dissertation, Ruhr-Universitat Bochum (2005).

[147] J. De Almeida and D. J. Thouless, Journal of Physics A: Mathematical and General **11**, 983 (1978).

[148] J. Mydosh, Reports on Progress in Physics **78**, 052501 (2015).

[149] F. Wang, J. Kim, Y.-J. Kim, and G. Gu, Physical Review B **80**, 024419 (2009).

[150] Y. Sun, M. Salamon, K. Garnier, and R. Averback, Physical Review Letters **91**, 167206 (2003).

[151] R. Chamberlin, G. Mozurkewich, and R. Orbach, Physical Review Letters **52**, 867 (1984).

[152] V. S. Dotsenko, Journal of Physics C: Solid State Physics **18**, 6023 (1985).

[153] F. Lefloch, J. Hammann, M. Ocio, and E. Vincent, Europhysics Letters **18**, 647 (1992).

[154] E. Vincent, J. Bouchaud, J. Hammann, and F. Lefloch, Philosophical Magazine B **71**, 489–500 (1995).

[155] P. Sibani and K. H. Hoffmann, Physical Review Letters **63**, 2853 (1989).

[156] N. Khan, P. Mandal, and D. Prabhakaran, Physical Review B **90**, 024421 (2014).

[157] H. Vogel, Phys. Z **22**, 645–646 (1921).

[158] G. S. Fulcher, Journal of the American Ceramic Society **8**, 339–355 (1925).

[159] J.-L. Tholence, Physica B+ C **126**, 157–164 (1984).

[160] E. Courtens, Physical Review Letters **52**, 69 (1984).

[161] C. Cardoso, F. Araujo-Moreira, V. Awana, E. Takayama-Muromachi, O. De Lima, H. Yamauchi, and M. Karppinen, Physical Review B **67**, 020407 (2003).

[162] K. He, S. Zhang, J. Li, X. Yu, Q. Meng, Y. Zhu, E. Hu, K. Sun, H. Yun, X.-Q. Yang, *et al.*, Nature Communications **7**, 11441 (2016).

[163] M. Lin, L. Ben, Y. Sun, H. Wang, Z. Yang, L. Gu, X. Yu, X.-Q. Yang, H. Zhao, R. Yu, *et al.*, Chemistry of Materials **27**, 292–303 (2015).

[164] D. Qian, B. Xu, M. Chi, and Y. S. Meng, Physical Chemistry Chemical Physics **16**, 14665–14668 (2014).

[165] H. Du, R. Che, L. Kong, X. Zhao, C. Jin, C. Wang, J. Yang, W. Ning, R. Li, C. Jin, *et al.*, Nature Communications **6**, 8504 (2015).

[166] H. Du, D. Liang, C. Jin, L. Kong, M. J. Stolt, W. Ning, J. Yang, Y. Xing, J. Wang, R. Che, *et al.*, Nature Communications **6**, 7637 (2015).

[167] F. Zheng, H. Li, S. Wang, D. Song, C. Jin, W. Wei, A. Kovács, J. Zang, M. Tian, Y. Zhang, *et al.*, Physical Review Letters **119**, 197205 (2017).

[168] Y. Liu, R. K. Lake, and J. Zang, Physical Review B **98**, 174437 (2018).

Vita

Roshan Kumar Nepal was born in Biratnagar, Nepal. After graduating from high school, he came to the United States in 2009 for higher education. He obtained his Bachelor of Science degree with dual majors in physics and mathematics from Southeastern Louisiana University in 2013. He joined the graduate program at Louisiana State University's Department of Physics and Astronomy in Fall 2015 and started his graduate research under the supervision of Professor Rongying Jin in Summer 2016. He received his Master of Science degree in physics in 2019 and is anticipating graduating with a Doctor of Philosophy degree in May 2020.